

WiserBAN



Project Acronym: WiserBAN

Project Title: Smart miniature low-power wireless microsystem for Body Area Networks

Call: FP7-ICT-2009-5, Collaborative project

Grant Agreement no.: 257454

Project Duration: 36 months

Coordinator: CSEM

Beneficiaries:

CSEM Centre Suisse D'Electronique et de Microtechnique SA – Recherche et Development	CSEM	CH
Commissariat a L'Energie Atomique et aux Energies Alternatives	CEA	FR
Fraunhofer-Gesellschaft zur Foerderung der Angewandten Forschung E.V.	FRAUNHOFER	DE
Valtion Teknillinen Tutkimuskeskus	VTT	FI
Technische Universitat Berlin	TUB	DE
Alma Mater Studiorum-Universita di Bologna	UNIBO	IT
Sorin CRM SAS	SORIN	FR
EPCOS SAS	EPCOS	FR
MED-EL Elektromedizinische Geraete GmbH	MED-EL	AT
Siemens Audiologische Technik GmbH	DE-SAT	DE
Debiotech S.A.	DEBIOTECH	CH
SignalGenerix Ltd	SG	CY
RTD TALOS Ltd	TALOS	CY

WiserBAN

Smart miniature low-power wireless microsystem for Body Area Networks

Deliverable identifier: D3.2

Deliverable title: First active and passive prototype antennas for WBAN microsystem and smart antenna-to-radio interface

Due date of deliverable: M16, 31.10.2011

Actual submission date: M20, 09.10.2012

Start day of project: 01/09/2010

Duration: 36 months

WP Number: WP3: Smart BAN antennas

Organization name of lead partner for this deliverable (partner name): VTT

Author(s): Jouko Aurinsalo (VTT), Antti Lamminen (VTT), Arto Rantala (VTT), Alexander Vasylychenko (CSEM), Cedric Hennemann (CSEM), Raffaele D'Errico (CEA), Laure Huitema (CEA), Sarah Sufyar (CEA), Christophe Delaveaud (CEA), Patricia Jameux (Epcos)

Document Status:

Project funded by the European Commission within the Seventh Framework Programme		
Dissemination Level		
PU	Public	
PP	Restricted to other programme participants (including the Commission Services)	
RE	Restricted to a group specified by the consortium (including the Commission Services)	
CO	Confidential, only for members of the consortium (including the Commission Services)	X

Revision History

Version	Date	Changed page(s)	Cause of change	Partner
V0.1	29.08.2011		First version	VTT
V0.2	08.11.2011		Second version	VTT
V0.3	23.11.2011		CEA contribution added	CEA
V0.4	28.11.2011		CSEM contribution added	CSEM
V0.5	29.11.2011		Edited	VTT
V0.6	13.03.2012		VTT contribution added	VTT
V0.7	13.03.2012		CSEM contribution added	CSEM
V0.8	16.03.2012		CEA contribution added	CEA
V0.9	26.03.2012		Comments taken into account	VTT
V1.0	28.03.2012		CSEM remarks taken into account	VTT
V1.1	03.04.2012		modified according to Board decision	VTT
V1.2	03.04.2012		Refined introduction and conclusion, and did final review	CSEM

Disclaimer: The information in this document is subject to change without notice. Company or product names mentioned in this document may be trademarks or registered trademarks of their respective companies.

All rights reserved.

The document is proprietary of the WiserBAN consortium members. No copying or distributing, in any form or by any means is allowed without the prior written agreement of the owner of the property rights.

This document reflects the authors' view. The European Community is not liable for any use that may be made of the information contained herein.

Contents

Executive Summary	6
1 Introduction	7
2 Overview of the WiserBAN antenna-to-radio interface.....	8
3 Transceiver and RF front-end.....	10
4 RF SAW filter.....	13
5 VTT active antennas with impedance matching on SoC.....	15
5.1 Antenna and matching circuit designs	16
5.1.1 L-antenna	16
5.1.2 Antenna impedance tuning	19
5.1.3 Antenna impedance sensing.....	21
5.2 First antenna prototypes	23
5.2.1 Test structures and prototype realization	23
5.2.2 Antenna measurements and results.....	27
5.3 Preliminary head proximity simulations	31
5.4 Summary and next steps.....	34
6 CEA miniature agile antenna.....	35
6.1 Antenna structure	35
6.2 Impedance agility simulated results	35
6.3 Methodology for antenna measurement.....	37
6.4 Antenna prototype.....	40
6.5 Impedance measurement.....	41
6.6 Radiation performances.....	43
6.6.1 Isolated antenna simulations	43
6.6.2 Measurement results	44
6.7 Antenna characteristics in the ear.....	46

6.7.1	Antenna orientation inside the auditory canal	46
6.7.2	Antenna depth inside the auditory canal	49
6.7.3	Ear to ear channel.....	51
6.8	Antenna/SiP interface.....	52
7	CSEM passive loop antenna for cochlear implant.....	53
7.1	Introduction	53
7.2	Matching circuit principle	55
7.3	Implementation of the matching circuit	56
7.4	Test bench and measurement setup.....	58
7.4.1	Test bench	58
7.4.2	Measurement results	61
7.5	Conclusion.....	66
8	CEA Passive antenna for Micro SD card	67
8.1	Antenna structure	67
8.2	Simulation results.....	68
8.3	Methodology for antenna measurement.....	71
8.4	Antenna prototype	72
8.5	Impedance results.....	72
8.6	Radiation results.....	75
8.7	Antenna characteristics in a Smartphone	76
8.7.1	Investigated scenarios	76
8.7.2	Simulation results of smartphone influence.....	77
8.7.3	Optimization of the antenna in the Smartphone	79
9	Conclusions	83

Executive Summary

The WiserBAN project will create an ultra-miniature and ultra-low power RF micro-system for wireless Body Area Networks (BAN) targeting primarily wearable and implanted devices for healthcare, biomedical and lifestyle applications.

The proposed research concerns the extreme miniaturization of the BAN with primarily the areas of ultra-low power radio SoC (System on Chip), RF and Low-frequency MEMS, miniature reconfigurable antennas, miniaturized SiP (System in Package), sensor signal processing and flexible communication protocols.

*At first this document describes **the antenna-to-radio interface** for various active and passive antennas developed in the WiserBAN project. The antenna-to-radio interface varies somewhat in different antenna cases. The aim of the document is to give the reader an overview of the various antenna interfaces.*

*Secondly the document describes **first manufactured active and passive antenna prototypes** and their first measurement results. Measured test results are compared to simulated performance results. The document sets the baseline for further antenna development in the project. Final antenna prototypes with test results will be described in deliverable D3.3.*

1 Introduction

i) About the contents of this document

This WiserBAN document describes both the overall configuration of the antenna-to-radio interface and basic design considerations for active and passive antennas. For each active and passive antenna also the test results of the first prototype antennas are presented.

The key components of the interface are the RF front-end, RF SAW filter and various WiserBAN antennas. The RF front-end and RF SAW filter are same in all use cases. Instead various antennas will be employed in different use cases. Consequently the antenna-to-radio interface varies somewhat in different use cases. This document highlights these differences.

The antenna-to-radio interface is described for two end user cases, wearable and implanted. For a wearable active antenna there are two different cases: tunable L-antenna for BTE (behind the ear) hearing aid and miniature agile dipole antenna for ITE (in the ear) hearing aid. A passive loop antenna is targeted for a cochlear implant. A passive planar antenna is developed for a micro-SD card which will be used as a remote control device in all use cases.

Furthermore the document describes the basic design considerations for each developed antenna (two active and two passive antennas). Now a first prototype antenna exists for each antenna type. Likewise all antenna prototypes have been characterized. The first performance test results are promising and they set a good basis for final antenna prototypes. These test results are also reported in the document.

The document describes also the basic design and operation principles of the AIST (antenna impedance sensing & tuning) system. The control system will be used with VTT active antenna. The key analog blocks of the control system were realized on the MPW 1 run (first WiserBAN CMOS processing).

ii) About material not yet included in this deliverable

Measurements on the AIST system are not yet included, as VTT experienced some issues requiring more time for characterization, and related to board parasitic effects and software implementation.

In order not to impede the presentation of the other material cited above under i) and which concerns 95% of the deliverable, and deliver D3.2 with even more delay, the WiserBAN board decided to:

- Submit D3.2 as is, at M20
- A memo will be issued in M22 with the outcome of the AIST characterization.
- The complete characterization results will be formally delivered in D3.3.

2 Overview of the WiserBAN antenna-to-radio interface

WiserBAN project is about the assembly of a communication protocol, 2.45 GHz RF transceiver, antenna tuning circuitry, control and digital interface functionalities into a small 65nm CMOS silicon chip which will be assembled together with RF and LF-MEMS devices (SAW, BAW, Si resonators) as well as external components into a small System in Package (WiserBAN SiP).

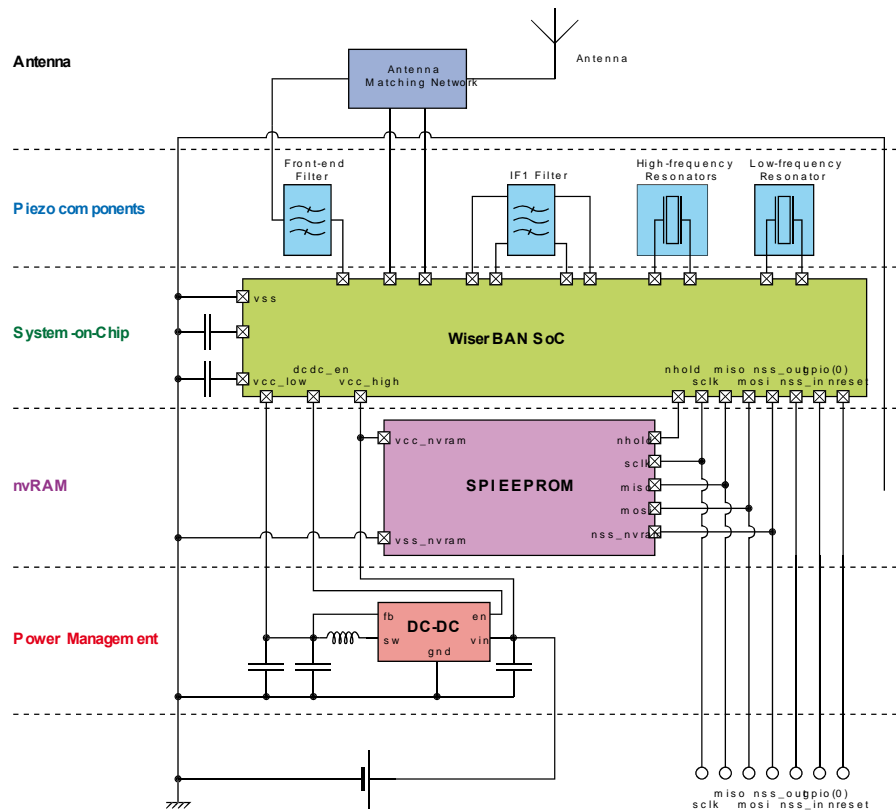


Figure 2.1 WiserBAN platform architecture (a detailed up-to-date block diagram is presented in document D1.2 WiserBAN platform specification and architecture)

The antenna-to-radio interface consists of the CMOS transceiver, RF SAW filter, possibly antenna matching circuit and antenna radiator (Figure 2.2). In case of an active antenna the antenna resonant frequency is tunable. In case of a passive antenna the antenna resonant frequency is fixed. In all cases antennas are matched to 50 ohms impedance and antenna output ports are single-end type.

Normally the antenna port is directly connected to the output port of the RF SAW filter. In the case of a tunable miniature dipole antenna the antenna matching is done in the antenna radiator structure and no separate matching circuit is needed. In the

case of a tunable L-antenna a part of the matching circuit is realized on the SoC. Therefore in this case the antenna output port comes exceptionally out from the SoC.

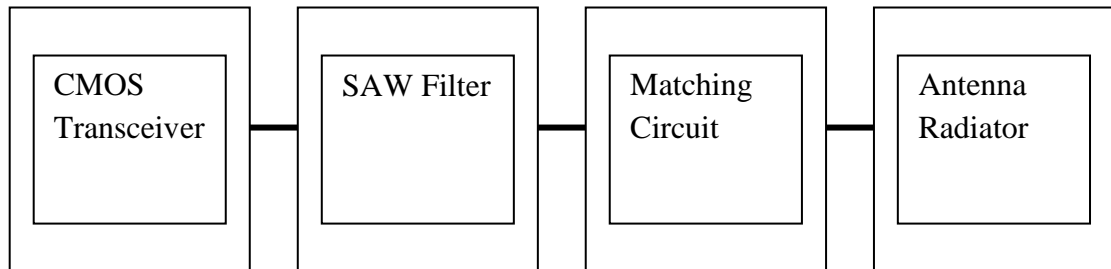


Figure 2.2 Main parts of the WiserBAN antenna-to-radio interface

3 Transceiver and RF front-end

The architecture of the WiserBAN transceiver is shown in Figure 3.1. In the receive mode the RF front-end converts the ISM band signal into a modulated fixed frequency signal at 2002 MHz. At this frequency the signal is bandpass filtered by an RF MEMS device (either SAW or BAW filter) before being sub-sampled, filtered, decimated and converted into a digital signal. In the transmit mode the data stream from the digital baseband (not drawn) modulates directly the transmit frequency. Before transmission the signal is amplified by the Pre-PA and PA. The key specifications of the transceiver are given in Table 3.1.

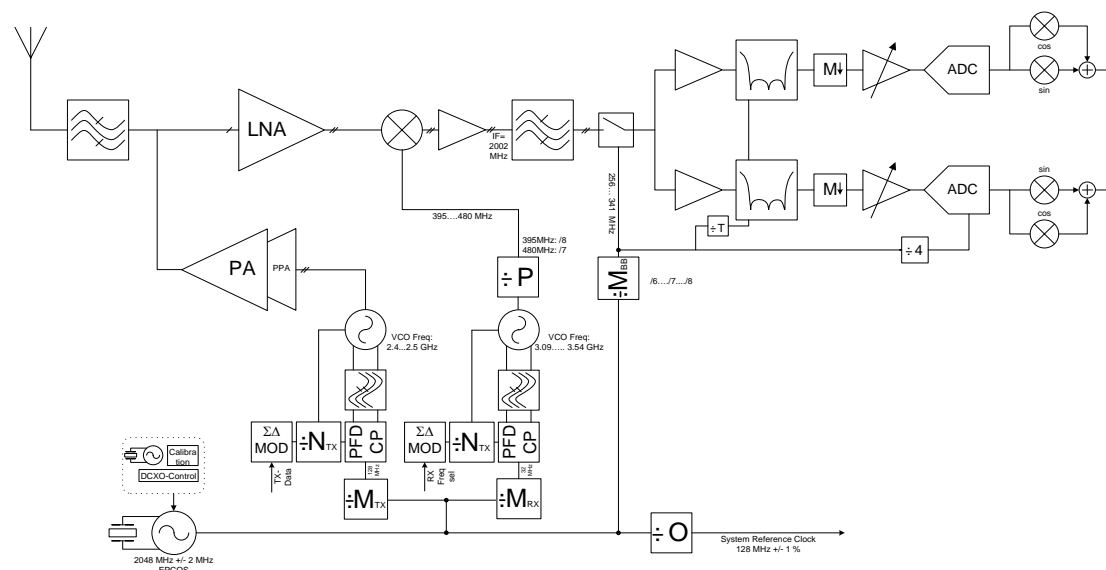


Figure 3.1 Block diagram of the WisserBAN transceiver

Table 3.1 Main specifications of the WiserBAN transceiver

Parameters	Symbols	Comments	Min	Typ	Max	Units
Supply voltage	V _{DDx}	1.2 V ± 10 %	1.08	1.2	1.32	V
Operating temperature	T _A		-40	27	85	°C
Total active current consumption	I _{Tot,RX}	Antenna to 2MBit/s Datastream		7.4		mA
	I _{Tot,TX}	2MBit/s Datastream to Antenna		6.9		
Total standby current consumption	I _{PLL_STB}			10		µA
Frequency range	f _{RTX,ISM}	ISM Band	2400		2485	MHz
	f _{RTX,ext}	Extended Frequency Band	2485		2500	MHz
Current consumption	I _{RX_FE}	RX Front-End (LNA & Mix)		1.6		mA
	I _{FREQ_SYNTH}	Frequency Synthesis RX/TX		3.0		mA
	I _{ABB}	Analog Baseband (Buffer, Sampler, FIR/IIR, VGA, ADC)		2.4		mA
	I _{DBB}	Digital Baseband		0.4		mA
	I _{PA}	Power Amplifier (@ 0 dBm)		3.5		mA
Receiver sensitivity	P _{SENS}	@ 2 MBit/s datarate		-90		dBm
Transmitted power	P _{TX}	@ 2 Mbit/s datarate		0		dBm

Maximum input signal strength	P_{RXmax}	with enabled AGC		-10		dBm
Peak data rate	DR	Maximum transmissible data rate			2	MBit/s
Silicon Area	$A_{TOT, RF}$	Preliminary estimation of the RF /Analog chip area, incl. pads		1.5		mm ²

A more detailed schematic presentation of the RF front-end is given in Figure 3.2. The specifications of the RF front-end are given respectively in Table 3.2.

Because the WiserBAN micro-system is under development different documents are not necessarily all the time up-to-date with each other. For detailed up-to-date information on the WiserBAN transceiver see document D1.3 WiserBAN radio system architecture and specification.

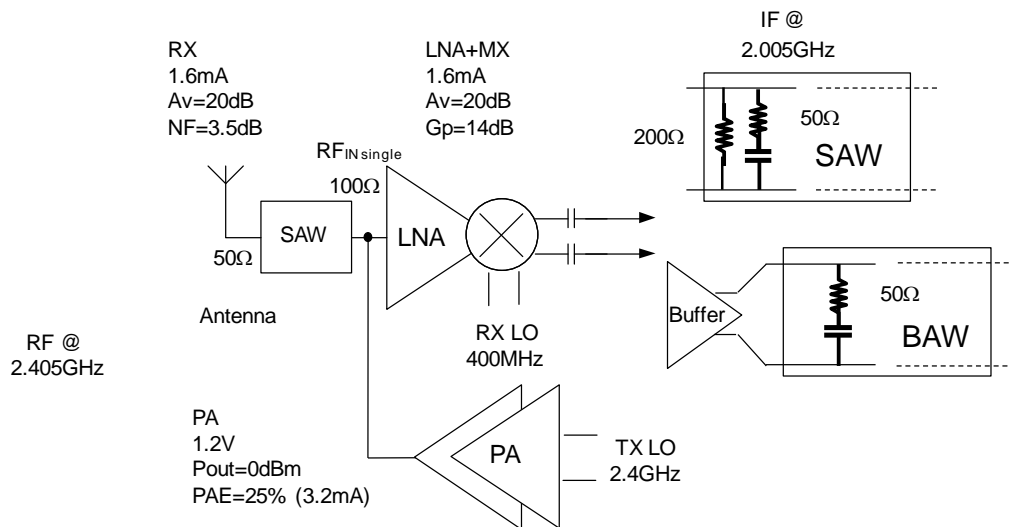


Figure 3.2 Schematic presentation of the RF front-end

Table 3.2 Specifications of the RF front-end

Typical specifications are at 25°C, voltage supply=1.2V, unless otherwise noted.

Parameter	Test conditions, comments	Min.	Typ.	Max	Unit
Temperature range		-25		+75	°C
Voltage supply		1.080	1.200	1.320	V
IF frequency	IF filter bandpass center		2.00 2		GHz
LO frequency		400		480	MHz
LO amplitude	single peak sinusoidal, 50% duty cycle		400		mV
Receiver					
Startup time			1		µs
TX – RX turnaround	RX bias on		0.4		µs
RX frontend current	LNA & MX, max. gain		1500		µA
	LNA & MX, AGC 6dB		800		
NF	100Ω source impedance		3.5		dB
Gv (voltage gain)	2 x (>15kΩ // 80fF) load single		34		dB
	200Ω diff load (IF filter)		18		
Attenuation (AGC)	3 steps	0		18	dB
IIP3	Max. gain, 200Ω diff load		-30		dBm
	Max. gain, high impedance		-34		
	Min. gain, 30dB attenuation		-2		
Transmitter					
Startup time			1		µs
RX – TX turnaround	TX bias on		0.4		µs
PA current	100Ω load impedance		3500		µA
Output power	100Ω load impedance		0		dBm
Spurious <1GHz	100kHz RBW			-54	dBm
Spurious >1GHz	1MHz RBW			-36	dBm
Leakages			20		nA

1. This receiver front-end gain can be digitally reduced in order to increase the dynamic with a digitally implemented AGC using the RSSI.
2. This specification is simplified from the ETS 300 220: it can be precise if problem encountered. To be complete, those limits are also needed in reception but this should not be a problem by construction.
3. The leakage is the current when functionality is fully off. This specification can only be measured as a sum with the leakage of the other parts of the SoC.

4 RF SAW filter

The RF filter is a SAW filter using bare die packaging technology (DSSP) which enables to get an height smaller than 250 μm (see outline drawing here below). The design is based on an existing design which has been resized for DSSP and modified to avoid the use of an external matching inductor. It is optimized for 50 Ω single ended source and load impedances.

Because the WiserBAN micro-system is under development different documents are not necessarily all the time up-to-date with each other. For detailed up-to-date information on the RF SAW filter see documents D1.3 WiserBAN radio system architecture and specification and D2.2 RF, IF & LF MEMS first samples.

Table 4.1 Main performance parameters of the RF SAW filter

Parameter	Design Goal E369			
	Min.	Typ.	Max.	Unit
Operating temperature range	0	-	60	°C
Center Frequency	-	2441.75	-	MHz
Passband Width	83.5	-	-	MHz
Max Insertion Loss over 83.5 MHz band @ Fc	-	2.0	2.8	dB
Relative attenuation				
880 - 960 MHz	40	-	-	dB
960 - 1980 MHz	34	-	-	dB
2110 - 2170 MHz	33	-	-	dB
2700 - 2800 MHz	35	-	-	dB
3600 - 5000 MHz	28	-	-	dB
Amplitude Ripple over 83.5 MHz band @ Fc	-	-	1.0	dB
Input V.S.W.R. over Passband	-	1.7	2.2	
Output V.S.W.R. over Passband	-	1.7	2.2	
Source Impedance (single - no external matching)	-	50	-	Ω
Load Impedance (single - no external matching)	-	50	-	Ω
Package size	DSSP 0.95 x 0.6 mm (CBT06A)			

5 VTT active antennas with impedance matching on SoC

The antenna is connected to the RF front-end at 50 ohms impedance level. The antenna input port is specified to be a single-end type configuration. In the case of a passive micro-SD card antenna the antenna radiator is directly matched to 50 ohms. In the case of a passive loop antenna an external matching circuit is used. In both cases the antenna port is connected directly to the output port of the RF SAW filter. The antenna bandwidths in these cases are sufficiently wide to cover a large fraction of 2.4 GHz ISM band. Thus no frequency tuning is needed.

CEA miniature tunable dipole antenna and VTT tunable L-antenna include a tunable component (varactor and digital capacitor bank). Both these antennas have a quite narrow instantaneous bandwidth (around 10 MHz) due to the antenna's small electrical size. The tunable component is used to tune the antenna to the correct RF frequency within 2.4 GHz ISM band. In the CEA antenna the varactor locates on top of the antenna radiator. The antenna matching to 50 ohms is done in the antenna structure. Therefore also this antenna is connected directly to the output port of the RF SAW filter similarly like passive antennas. The miniature tunable dipole antenna will be described in detail in Section 6.

In VTT antenna the impedance matching circuit is partly realized on the antenna platform and partly on the SoC. For example the digitally controlled capacitance bank locates on the SoC. The benefit of this solution is that no active components are needed in the antenna radiator structure. In this case the antenna signal comes out from the SoC to the output port of the RF SAW filter. This integrated antenna & radio front-end requires a particularly careful interface co-design.

5.1 Antenna and matching circuit designs

5.1.1 L-antenna

The first tunable antenna design shown in Figure 5.1.1 is a so-called L-antenna which consists of 4 mm × 4 mm sized ground plane, spiral inductor and L-shaped radiating element. The antenna is designed for an IPD (Integrated Passive Device) process in which the conductors are patterned on top and bottom sides of 0.055 mm thick polyimide layer. The polyimide is placed on top of 0.625 mm thick quartz substrate. The overall antenna volume is about 4 x 8 x 0.7 mm³. The electrical parameters of the polyimide are $\epsilon_r=3.36$ and $\tan\delta=0.001$. The quartz substrate has $\epsilon_r = 3.8$ and $\tan\delta = 0.0001$.

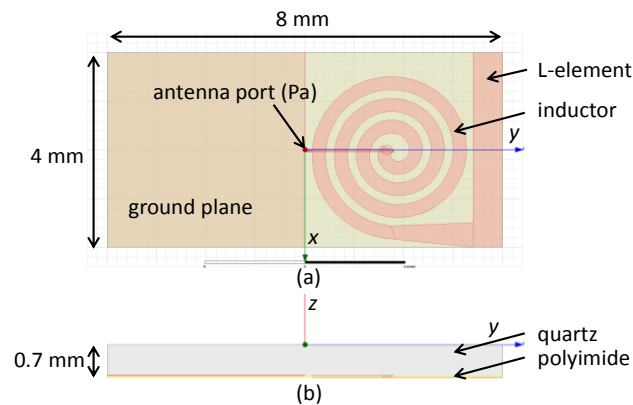


Figure 5.1.1 Layout of L-antenna on IPD: (a) top view, (b) side view

The simulated antenna impedance of the first version of L-antenna is plotted on Smith chart in Figure 5.1.2. At 2.4 GHz the impedance is $(3.5+j11.6) \Omega$. The radiation resistance is small which indicates small radiation efficiency as expected for an electronically small antenna ($a \approx \lambda/15$). The real part remains almost constant between 2.3 and 2.5 GHz but the imaginary part varies between $-j42 \Omega$ and $+j76 \Omega$.

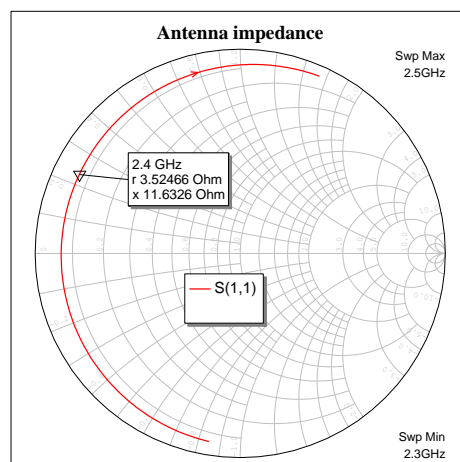


Figure 5.1.2 Input impedance of L-antenna

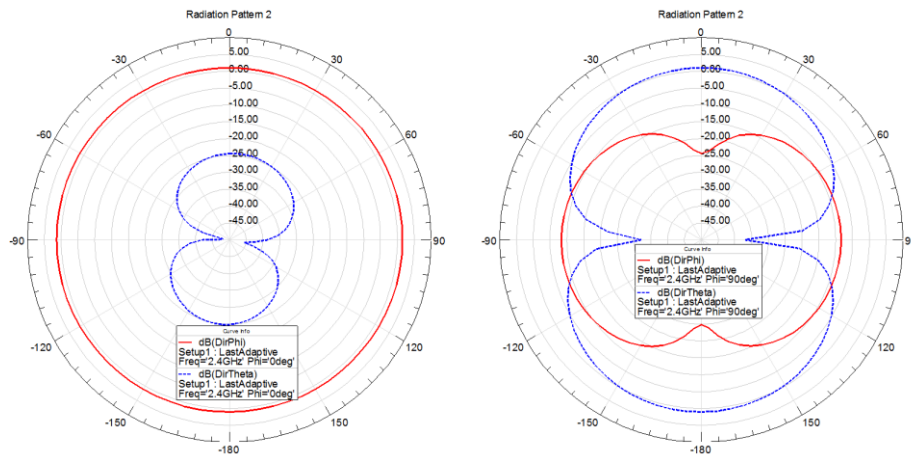


Figure 5.1.3 Radiation patterns of L-antenna

The simulated radiation patterns are shown in Figure 5.1.3. The 3D radiation pattern is a dipole-like “donut” with minimums at the directions of the $\pm y$ -axis.

The antenna impedance is poorly matched to $50\ \Omega$ and the reflection coefficient is only $-1.2\ \text{dB}$ at the lowest when normalized to $50\ \Omega$. The matching circuits shown in Figure 5.1.4 can be used to match the antenna impedance to $50\ \Omega$. The matching circuit consists of a series capacitor C1 and a shunt inductor L (A) or series capacitor C1 and shunt capacitor C2 (B). The center frequency of the antenna can be tuned by tuning C1. Tunable capacitors are implemented using CMOS capacitor banks on the SoC. Matching circuit topology B is preferred in this project because both matching components can be tunable and integrated compactly on the SoC. The center frequency of the antenna is tuned by switching between different capacitors in the C1 bank.

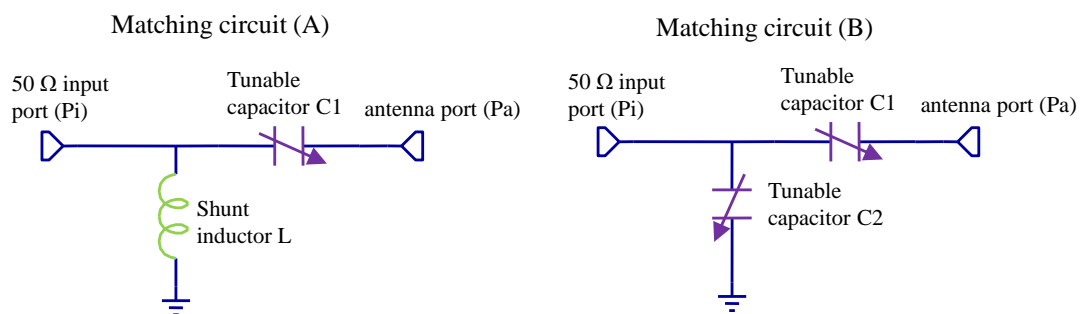


Figure 5.1.4 Matching circuits for L-antenna

An example of L-antenna tuning between frequencies 2365 and 2445 MHz is presented in Figure 5.1.5. Nine tuning steps, i.e., nine different capacitance values are needed for a tuning range of 80 MHz: 1.2, 1.37, 1.59, 1.88, 2.29, 2.90, 3.85, 5.7 and 10.4 pF. The exact capacitance values are determined in co-operation with the capacitor bank designer. The right vertical axis in Figure 5.1.5 represents efficiency. The black curves indicate the matching circuit efficiency (mc eff.) when the Q values of C and L are assumed to be 30 and 50, respectively. The mc eff. is above 70%

across the frequency band. The radiation efficiency of the antenna is about 14% which results to an overall antenna efficiency of 11%. This value includes the matching circuit losses. Since the directivity of L-antenna is about 1.5 dBi at the maximum, the maximum gain is about -8 dBi. However, it should be noted that these values do not take into account the human body effect or the surroundings of the antenna in a real application environment.

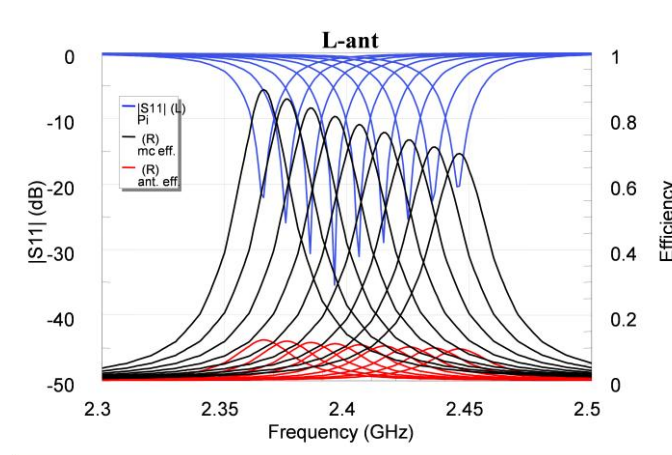


Figure 5.1.5 Tuning of L-antenna

Table 5.1.1 Tunable L-antenna specifications

Parameters	Comments	Values	Units
Dimensions	Height less than 1 mm	4*8*0.7	mm
Frequency range		2400 - 2485	MHz
Instantaneous BW	Tunable over the frequency range	10	MHz
Input impedance		50	ohms
VSWR	Corresponds to return loss of 6 dB	3	
Efficiency	Total efficiency	10	%
Radiation pattern	Like small dipole		

5.1.2 Antenna impedance tuning

The antenna impedance tuning is implemented as a part of the ASIC circuit. The tuner contains a binary weighted n-bit capacitor array with a small unit capacitor. The binary weighted capacitor array provides in theory linear control steps over capacitor range as response of control but also at the same time a minimum size of total capacitance i.e. occupied silicon area. On the other hand the obtained frequency tuning is not a linear function of control which means that a higher number of control bits are required to cover the whole tuning range. The selection of capacitors inside the array is performed by RF switches. Furthermore a digital interface is available for the switch control.

In addition to the capacitor bank a shunt inductor is required in the matching circuit. The original idea was that the shunt inductor is a part of the IPD platform. However, a moderately small inductance value ($L \sim 1\text{nH}$) indicates that there is a possibility to implement this component as a planar inductor inside the ASIC. The benefit of the integrated inductor is a reduced number of RF interconnections between the ASIC and IPD. The drawback is a lower Q value of the integrated inductor and an increase in silicon area. In the first version of the WiserBAN SoC the integrated inductor is not used but this alternative has to be considered more carefully in the design of the final WiserBAN SoC.

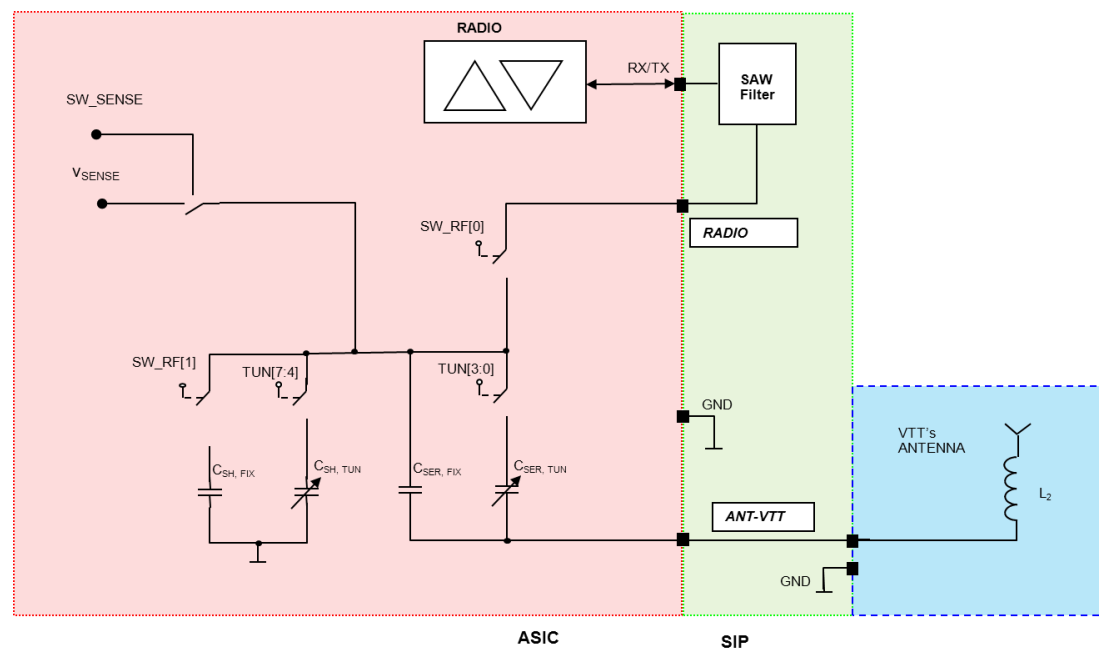


Figure 5.1.6 Simplified schematic diagram of the tuner circuit

An RF switch isolating the tuner from the radio has been added. This arrangement augments the performance of the sensing block since the impedance vs. frequency response of the RF SAW filter can be omitted. Moreover, the switch isolates the sensing signal generator (oscillator) from the radio (LNA & PA).

A simplified diagram of the antenna tuning circuit is shown in Figure 5.1.6. The transmit RF signal from the radio front-end goes through the RF SAW filter to the capacitor bank on SoC. From the capacitor bank the transmit signal continues to the antenna radiator on IPD. The matching circuit is partly integrated on the same IPD platform on which the antenna radiator locates. During the normal operation the tuner control circuit has set to a fixed switch configuration to enable a proper antenna matching. The impedance sensing circuit is disabled and disconnected from the tuner using an RF switch (SW_{SENSE}). When the impedance sensing routine is invoked at the system level (DSP, IcyFlex) the isolation switch (SW_{RF}) between the tuner and the RF SAW filter is switched off and the sensing circuit is activated. The main design parameters of the tuning circuit are listed in Table 5.1.2.

Table 5.1.2 Design parameters of the tuning circuit

Parameters	Comments	Values (1)	Units
Shunt capacitor, C_{SH}			
C_u	Unit capacitor, tuning step	0.10	pF
C_f	Fixed capacitance, minimum capacitance	$41 * C_u$	pF
C_{max}	Maximum capacitance	$56 * C_u$	pF
n	Number of control bits, 2^n steps	4	
Serial capacitor, C_{SER}			
C_u	Unit capacitor, tuning step	0.21	pF
C_f	Fixed capacitance, minimum capacitance	$5 * C_u$	pF
C_{max}	Maximum capacitance	$20 * C_u$	pF
n	Number of control bits, 2^n steps	4	
Q_c	Capacitor Q-value	270	
$R_{on, SW}$	RF switch on resistance	< 1 (2)	Ω
L_{SW}	RF switch isolation at 2.4 GHz	tbd (2)	dB

(1) Typical process parameters

(2) Trade-off between values, to be redefined later

5.1.3 Antenna impedance sensing

An optimal antenna tuning is performed by using a novel impedance sensing method. The method requires a direct signal access to the antenna input port and it can not be used at the same time when the radio (Tx/Rx) operates. Therefore the main control for the sensing and tuning is done at system level by DSP/IcyFlex which invokes the sensing/tuning algorithm when necessary. When the device environment does not change or changes only slowly over the time (small proximity effect) the antenna sensing/tuning system is activated infrequently after the boot-up of the system.

A simplified schematic diagram of the antenna impedance sensing circuit is shown in Figure 5.1.7. The system level control for the circuit block is performed by a digital interface (registers) which is controlled at the system level. In the default condition the sensing block is in idle state i.e. disabling all activity except setting control for the capacitance bank switches. When the sensing or tuning operation is requested at the system level the sensing circuit is activated and the frequency shift of the antenna tuning is analyzed and the proper configuration for the tuner is determined. After the sensing sequence has been finished a status of the tuning is delivered to the system level: tuning succeeded / failed. In the first version of the ASIC the digital interface will be also utilized to characterize the circuit operation and to test different algorithm versions for an optimal tuning.

The antenna impedance sensing will be performed by using a controllable oscillator circuit which is highly sensible to loading effect. The operational point of the oscillator is controlled digitally. The output response is obtained from a frequency counter and it is analyzed by a specific algorithm. The acquired response vs. control is analyzed and recorded at first in the nominal condition, when no unwanted proximity effects are present. In case the sensing is activated the impedance sensing/analysis routine is repeated and a deviation from the nominal condition is calculated. The calculated difference is used to re-adjust the tuning circuit for a proper impedance match.

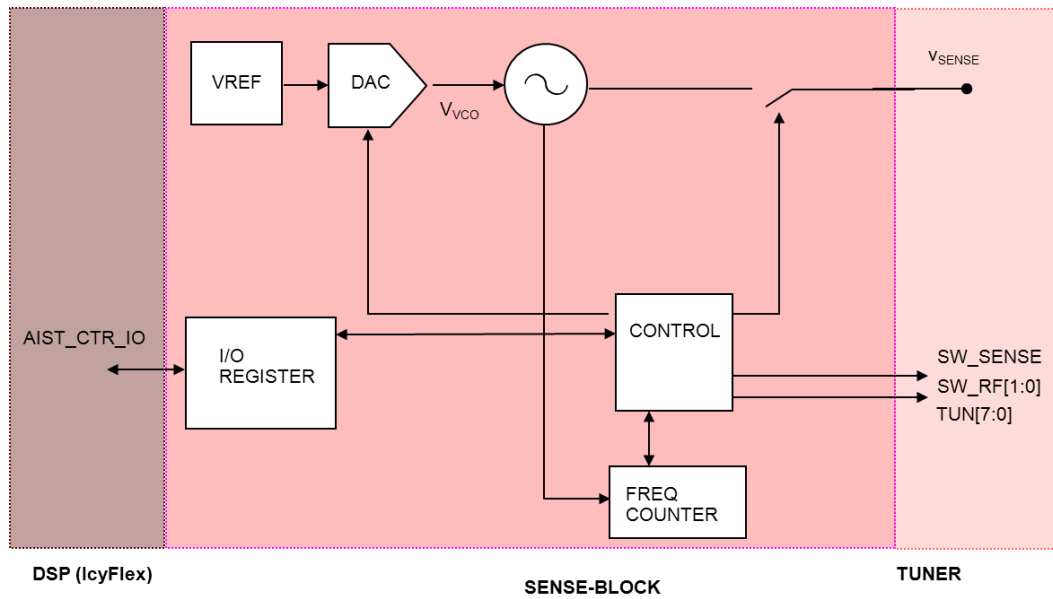


Figure 5.1.7 Simplified schematic diagram of the impedance sensing block

Table 5.1.3 Design parameters of the sensing circuit

Parameters	Symbols	Comments	Min	Typ	Max	Units
Supply voltage	V_{DDx}	1.2 V \pm 10 %	1.08	1.2	1.32	V
Operating temperature	T_A		-40	27	85	$^{\circ}\text{C}$
Total active current consumption	I_{AIST_DD}			1		mA
Total standby current consumption	I_{AIST_STB}			< 1		nA
Frequency	f_{AIST}	Sensing test signal		2450		MHz
Silicon Area				0.0034		mm^2

5.2 First antenna prototypes

5.2.1 Test structures and prototype realization

The basic concepts of L-antenna and the matching circuit (MC) designs are presented in the Section 5.1. The antenna can be matched into 50Ω also by using a shunt capacitor instead of a shunt inductor in the MC shown in Figure 5.1.4. Due to this fact, both MC components can be tunable when implemented using digital capacitor banks on the SoC.

The first L-antenna prototypes were designed on Taconic RF-35 RF PCB material having a substrate and copper thicknesses of 0.5 mm and 35 μm . The relative permittivity is $\epsilon_r=3.5$ and the loss tangent is $\tan\delta = 0.0018$. Two versions shown in Figure 5.2.1 were optimized using Ansoft HFSS EM simulator: with MC version A (L-antenna v1) and MC version B (L-antenna v2). In the first prototypes, discrete L-Series 0201 ceramic capacitors by Johanson Technology were used in the MCs. The non-ideal capacitors were modeled in the HFSS by using an equivalent series L_c -C- R_c circuits. The values of L_c and R_c were determined using AWR Microwave Office circuit simulator by comparing the L_c -C- R_c equivalent circuit with the real S-parameter models of the Johanson capacitors. The L_c and R_c values obtained through simulations are 0.4 nH and 1.1 Ω . The series and shunt capacitors of 3.9 pF and 2.7 pF were used. The integrated shunt inductor in v1 has an inductance value of 1.5 nH.

The simulation results of L-antenna v1 and v2 are presented in Figure 5.2.2 and 5.2.3. The center frequencies are at 2.40 GHz and 2.43 GHz. The maximum realized gains are -6.5 dBi and -7.8 dBi. The lower gain in v2 is due to lower return loss which is 8.8 dB. In v1 the return loss is 18.9 dB.

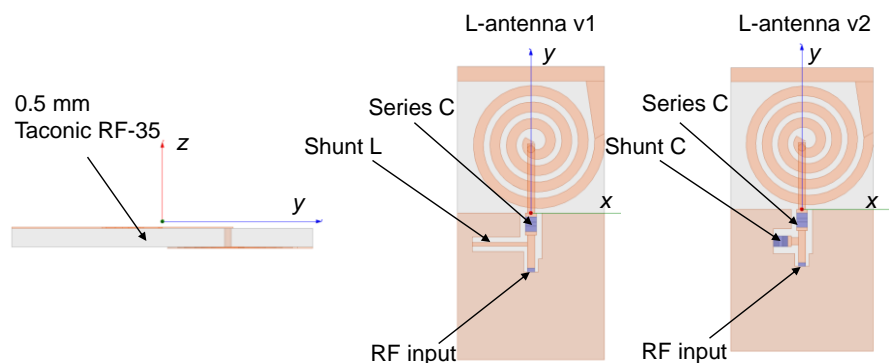


Figure 5.2.1 Simulation models of the L-antenna prototypes

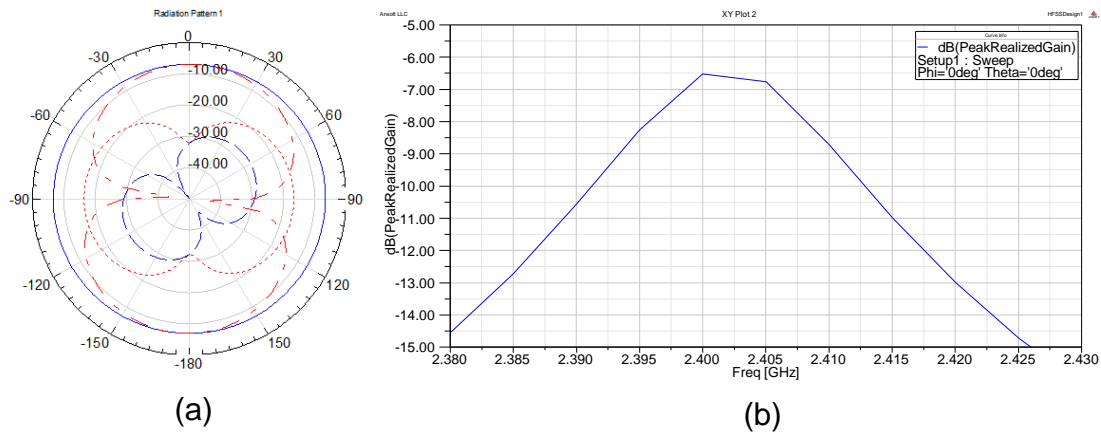


Figure 5.2.2 Simulation results of the L-antenna v1. (a) realized gain patterns at 2.4 GHz: phi-comp. $\phi=0$ deg. (solid line), phi-comp. $\phi=90$ deg. (dot line), theta-comp. $\phi=0$ deg. (dash line), theta-comp. $\phi=90$ deg. (dash-dot line). (b) peak realized gain vs. frequency.

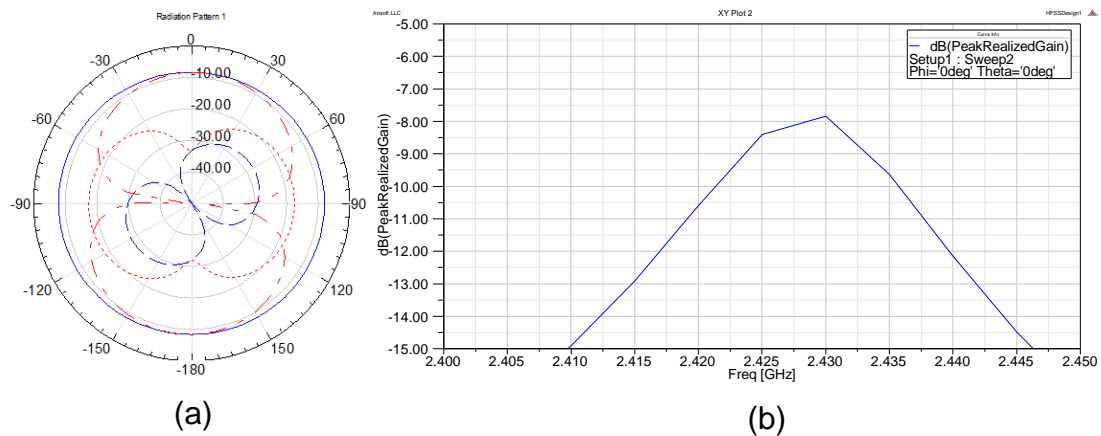


Figure 5.2.3 Simulation results of the L-antenna v2. (a) realized gain patterns at 2.43 GHz: phi-comp. $\phi=0$ deg. (solid line), phi-comp. $\phi=90$ deg. (dot line), theta-comp. $\phi=0$ deg. (dash line), theta-comp. $\phi=90$ deg. (dash-dot line). (b) peak realized gain vs. frequency.

To reduce the xy-size of the antenna, a so-called spiral antenna was also designed. The antenna consists of a planar spiral inductor on top of a ground plane separated by a substrate. The spiral size is 4 mm×4 mm in the xy-plane. The antenna height, i.e., the substrate thickness, has an effect on the radiation efficiency as shown in Figure 5.2.4. The thicker is the substrate, the higher is the efficiency. Based on simulations and investigations on available commercial PCB materials, a thickness of 3 mm was chosen for the spiral antenna.

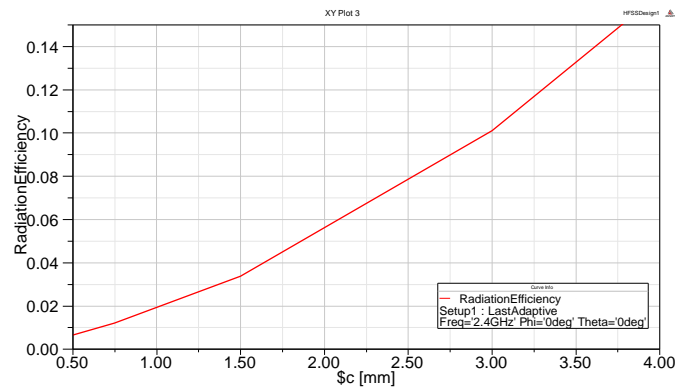


Figure 5.2.4 Radiation efficiency of spiral antenna as a function of substrate thickness

Similarly, two versions of the spiral antennas with MC types A and B were designed and optimized using HFSS. The substrate material used is a 3 mm thick Taconic RF-35 with 35 μm thick copper. The ground plane of the antenna is extended by 4 mm in order to have enough space for the U.FL coaxial connector for RF testing.

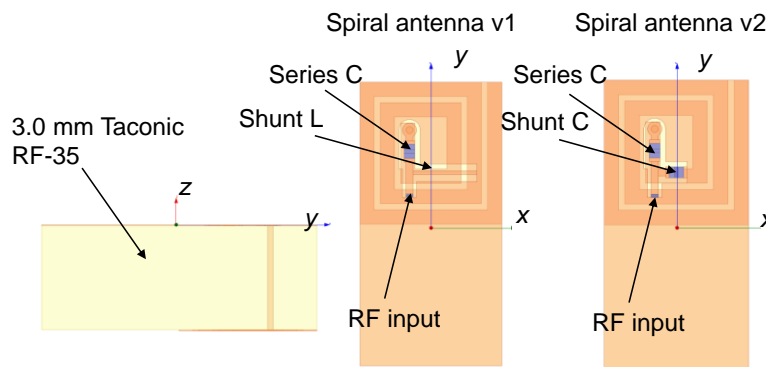


Figure 5.2.5 Simulation models of the spiral antenna prototypes

The large ground plane (4 mm \times 8 mm) lowers the resonance frequency of about 200 MHz while the radiation efficiency remains almost the same when compared to an antenna with a small ground plane (4 mm \times 4 mm). The simulation models of the spiral antennas are shown in Figure 5.2.5.

The simulation results of spiral antenna v1 and v2 are presented in Figure 5.2.6 and 5.2.7. The center frequencies are at 2.205 GHz and 2.255 GHz. The maximum realized gains are -9.2 dBi and -10.1 dBi. The return losses of both antennas are about 21 dB at the center frequencies. The radiation patterns are different from L-antennas. There is no clear main polarization and the polarization is a mix of theta- and phi-components. The nulls occur in the direction of z -axis and not in the direction of y -axis as is the case in the L-antenna.

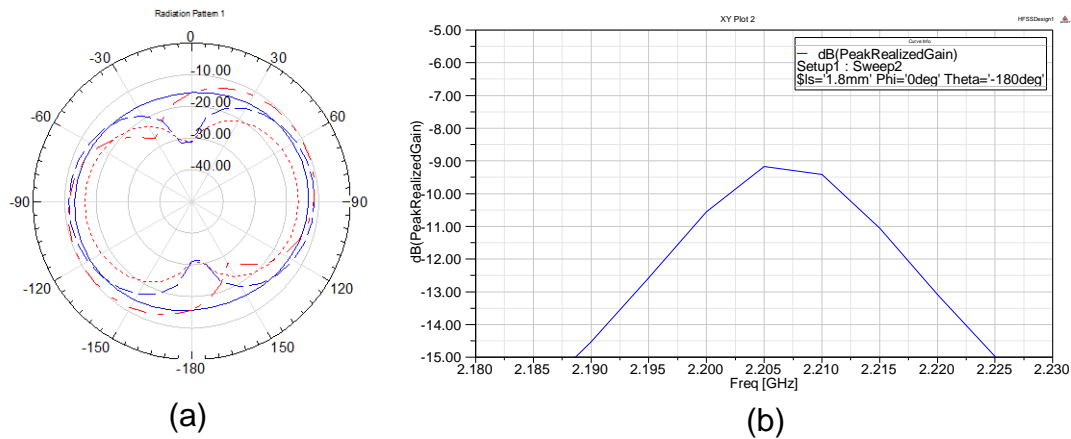


Figure 5.2.6 Simulation results of the spiral antenna v1. (a) realized gain patterns at 2.205 GHz: phi-comp. $\phi = 0^\circ$ deg. (solid line), phi-comp. $\phi = 90^\circ$ deg. (dot line), theta-comp. $\phi = 0^\circ$ deg. (dash line), theta-comp. $\phi = 90^\circ$ deg. (dash-dot line). (b) peak realized gain vs. frequency.

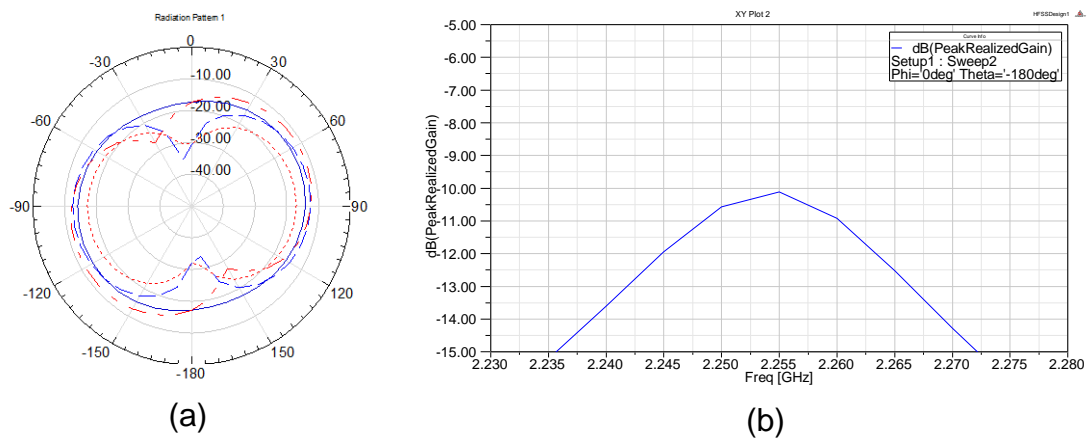


Figure 5.2.7 Simulation results of the spiral antenna v2. (a) realized gain patterns at 2.255 GHz: phi-comp. $\phi = 0^\circ$ deg. (solid line), phi-comp. $\phi = 90^\circ$ deg. (dot line), theta-comp. $\phi = 0^\circ$ deg. (dash line), theta-comp. $\phi = 90^\circ$ deg. (dash-dot line). (b) peak realized gain vs. frequency.

The first antenna prototypes were manufactured at Dowell Oy in Lahti, Finland. The layouts of Figures 5.2.1 and 5.2.5 were slightly modified and contact pads were added for a Hirose UFL coaxial connector for RF testing of the antennas. The photographs of the manufactured antennas are shown in Figures 5.2.8 and 5.2.9.

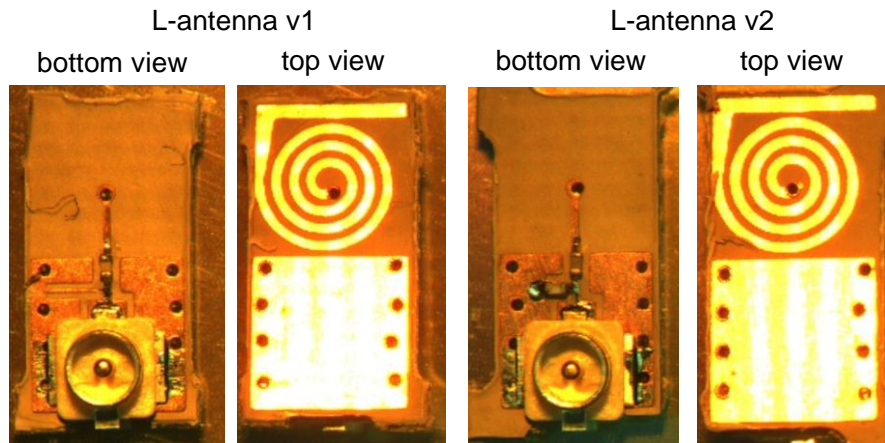


Figure 5.2.8 Photographs of the first L-antenna prototypes

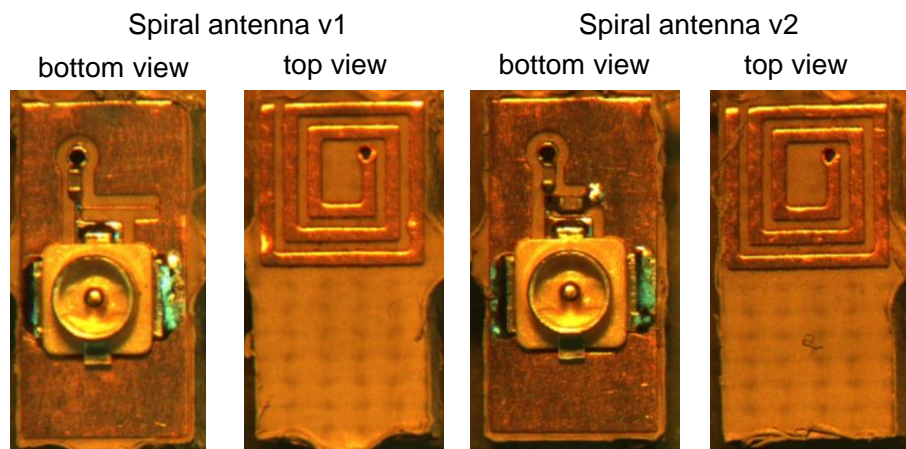


Figure 5.2.9 Photographs of the first spiral antenna prototypes

5.2.2 Antenna measurements and results

Reflection coefficients of the antennas were measured using a vector network analyzer. SMA-UFL RF cable adapters were used to feed the antennas as shown in Figure 5.2.10. The calibration reference located at the SMA connector. A short-circuited cable was measured to determine the measurement cable losses. Comparative measurements were done with a balun added on top of the measurement cable. The balun is a $\lambda/4$ long metal sleeve which is shorted at its one end. The balun provides a balanced feed for the antenna and prevents ground currents from flowing on the outer connector of the coaxial cable.

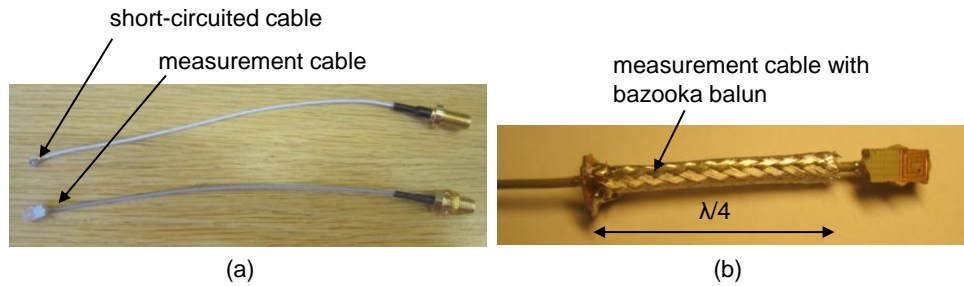


Figure 5.2.10 Photographs of the UFL-SMA RF cables. The cable losses were measured from a short-circuited cable shown in (a). A bazooka balun shown in (b) was used with the coaxial cable to provide balanced feed for the antennas.

Simulated and measured reflection coefficients of the four antenna prototypes are presented in Figures 5.2.11–5.2.14. In the L-antenna v1, the measured and simulated center frequencies are at 2.474 GHz and 2.402 GHz. With cable and balun the simulated center frequency is at 2.262 GHz. The measured $|S_{11}|$ of the “shorted UFL” shows that the cable loss is about 1.1 dB.

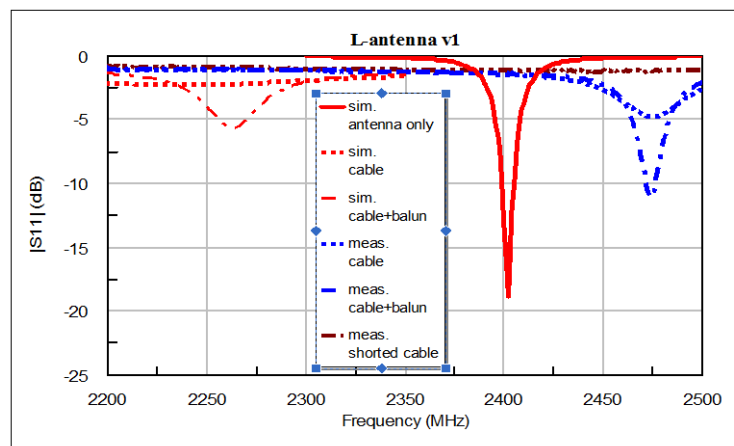


Figure 5.2.11 Reflection coefficients of L-antenna v1.

In the L-antenna v2, the measured center frequency without balun is at 2.194 GHz while the simulated center frequency is at 2.430 GHz. There are no clear resonances seen in the measurement results with balun but a small dip occurs at 2.702 GHz.

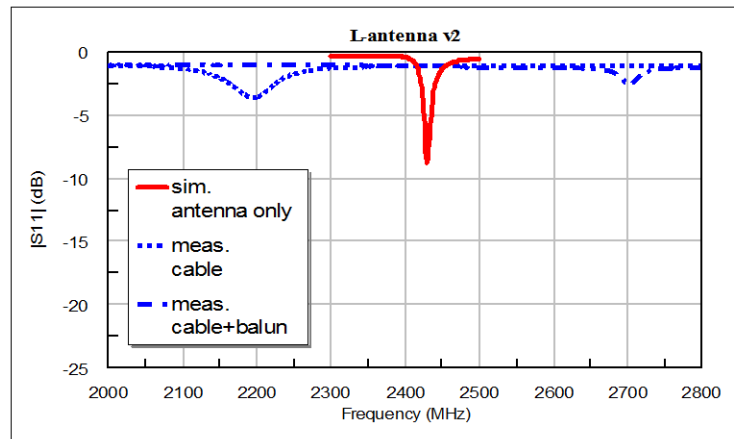


Figure 5.2.12 Reflection coefficients of L-antenna v2.

Without balun the measured $|S_{11}|$ of the spiral antennas are only between -4 dB and -5 dB. Fortunately, the balun improves the performance of the spiral antennas significantly. In the spiral antenna v1, the measured and simulated center frequencies are at 2.144 GHz and 2.207 GHz. In the spiral antenna v2, the measured and simulated center frequencies are at 2.196 GHz and 2.256 GHz. Simulations with cable and balun agree well with the measurements.

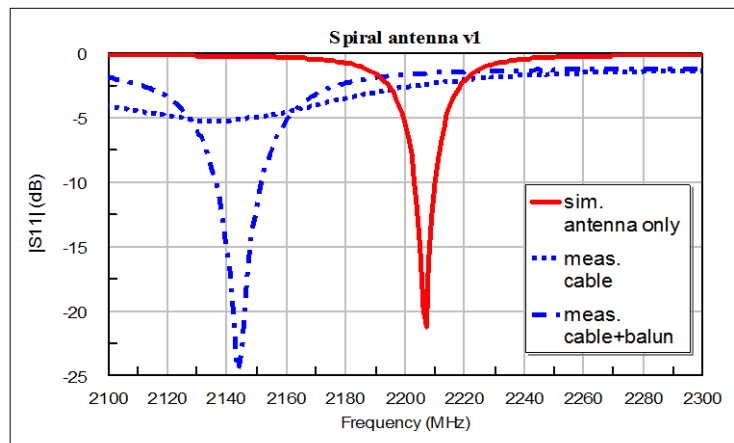


Figure 5.2.13 Reflection coefficients of spiral antenna v1.

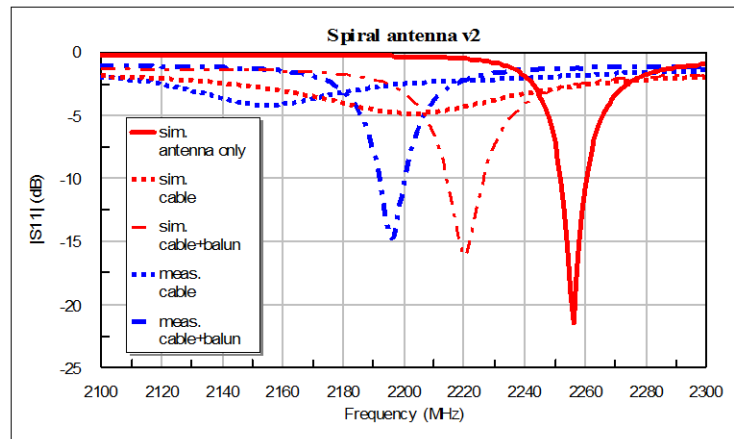


Figure 5.2.14 Reflection coefficients of spiral-antenna v2.

It is seen from the $|S_{11}|$ results that the measurement cable has a strong influence on the antenna performance due to very small size of the antennas. Despite of using a balun, there are some deviations between the simulations and the measurements which are partly caused by manufacturing inaccuracies and partly by small differences between the simulated and measured test setups. It also seems that the L-antenna is more sensitive to the cable than the spiral antenna. This is probably due to differences in the antenna polarizations and radiation patterns. The near field coupling to the cable is stronger in the L-antenna than in the spiral antenna.

Simulated and measured radiation patterns of the antennas are shown in Figure 5.2.15 and 5.2.16. It is seen that the cable distorts the patterns quite much. The antenna efficiencies including the cable and balun are higher than for antenna alone. However, the simulated and measured efficiencies are of the same order, especially with the spiral antenna.

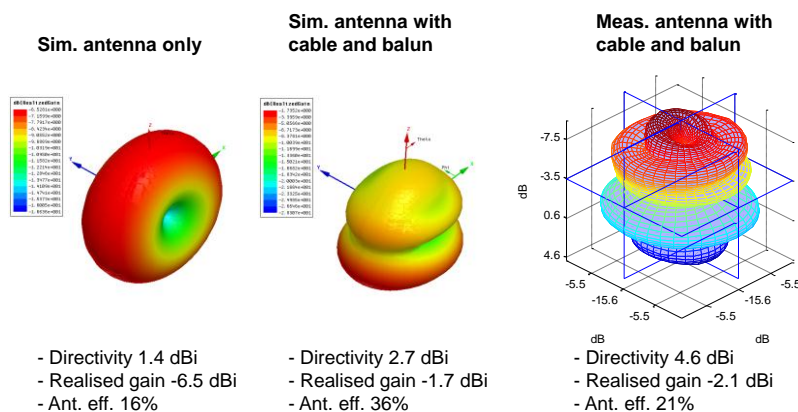


Figure 5.2.15 Radiation patterns of L-antenna v1

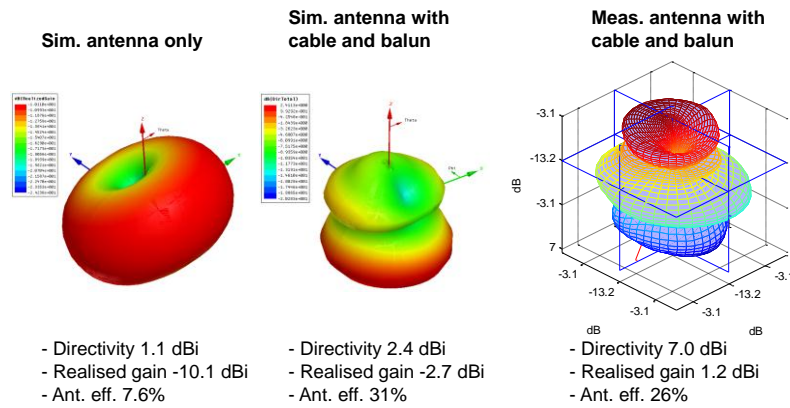


Figure 5.2.16 Radiation patterns of spiral antenna v2

The simulation and measurement results are summarized in Table 5.2.1.

Table 5.2.1 Summary of the L-antenna and spiral antenna results

Antenna type	Center freq. (meas., sim.) [GHz]	-10 dB bw (meas.,sim.) [MHz]	Real. gain (sim.) [dBi]	Ant. eff. (sim.) [%]
L-antenna v1	2.474, 2.402	4.8, 5.8	-6.5	16
L-antenna v2	2.194, 2.430	-,-	-7.8	16
Spiral antenna v1	2.144, 2.207	15.4, 6.9	-9.2	8
Spiral antenna v2	2.196, 2.256	8.4, 8.5	-10.1	8

5.3 Preliminary head proximity simulations

Preliminary investigations of a head proximity to the antenna performance were done by simulating antennas together with a simplified head model. The model consists of rectangular “ear” and “head” including different tissue layers. The “ear” is formed by “skin”-“cartilage”-“skin” layer combination each having a thickness of 2 mm. The “head” also includes three layers: “skin”, “bone” and “brain”. The electrical parameters of the layers are shown in Table 5.3.1.

Table 5.3.1 Electrical parameters of the simple head model at 2.45 GHz

	Relative permittivity ϵ'_r	Conductivity σ (S/m)
skin	38	1.49
cartilage	38.7	1.79
bone	11.4	0.4
brain	48.8	1.84

The distance d between the antenna and the “ear” and the “head” was varied between 1 mm and 10 mm. The L-antenna and spiral antenna were aligned horizontally and vertically in respect to the head model. The simulation setups with L-antennas are shown in Figures 5.3.1–5.3.2.

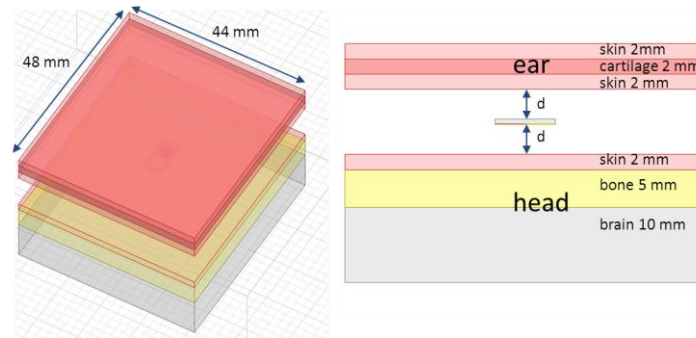


Figure 5.3.1 L-antenna horizontally aligned near a simple head model

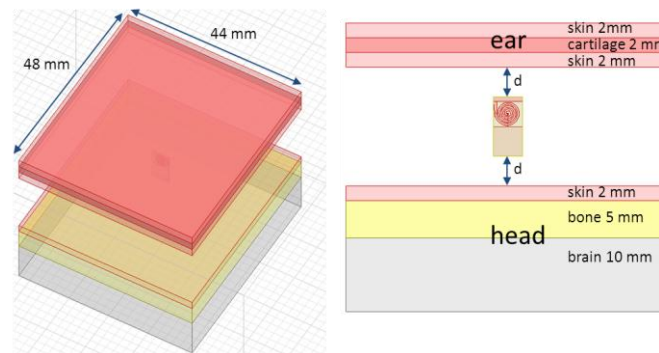


Figure 5.3.2 L-antenna vertically aligned near a simple head model

First, the antenna impedance was matched into 50Ω in free space environment. Thereafter, the reflection coefficients of antennas locating at different distances from the head model were plotted. The results of the L-antenna are shown in Figure 5.3.3. It is seen that the center frequency shift is larger in the horizontally aligned L-antenna (polarization tangential to the head) than in the vertically aligned L-antenna (polarization normal to the head). For example, at distance $d=2\text{mm}$, the frequency shift is 58 MHz for the horizontally aligned L-antenna whereas the shift is 33 MHz for the vertically aligned L-antenna.

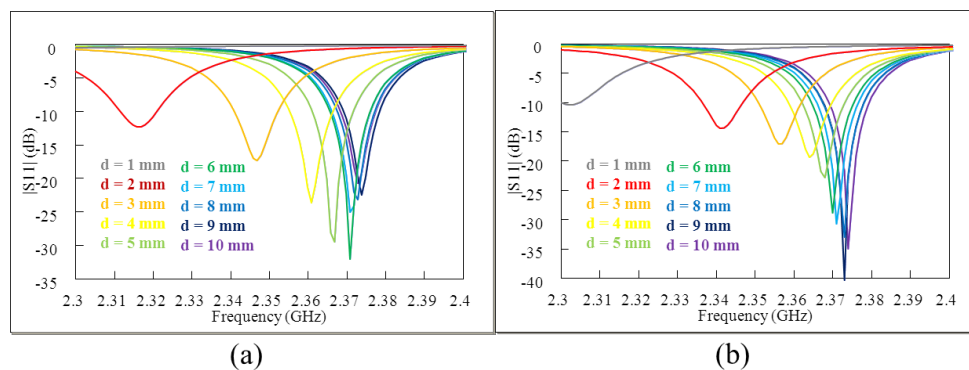


Figure 5.3.3 Frequency detuning of (a) horizontally and (b) vertically aligned L-antenna near a simple head model

The simulation models of the spiral antennas are shown in Figures 5.3.4–5.3.5 and the reflection coefficients in Figure 5.3.6. It is seen from the results that also the spiral

antenna is less sensitive to the head when aligned vertically. At distance $d=2\text{mm}$, the frequency shifts are 36 MHz in Figure 5.3.6a and 13 MHz in Figure 5.3.6b.

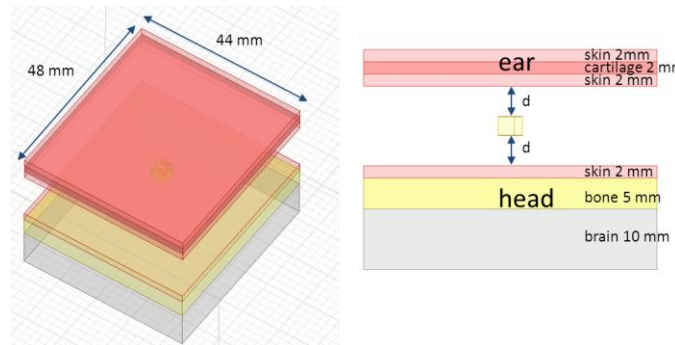


Figure 5.3.4 Spiral antenna horizontally aligned near a simple head model

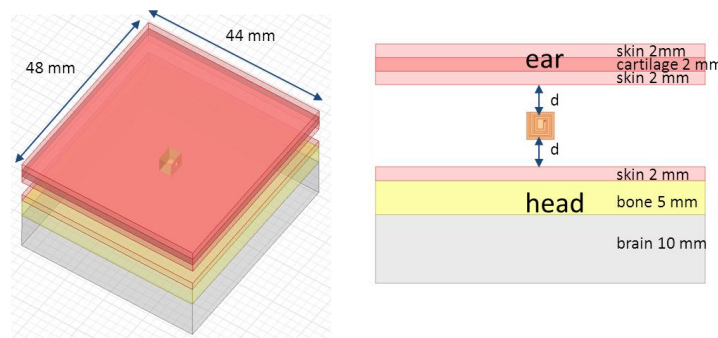


Figure 5.3.5 Spiral antenna vertically aligned near a simple head model

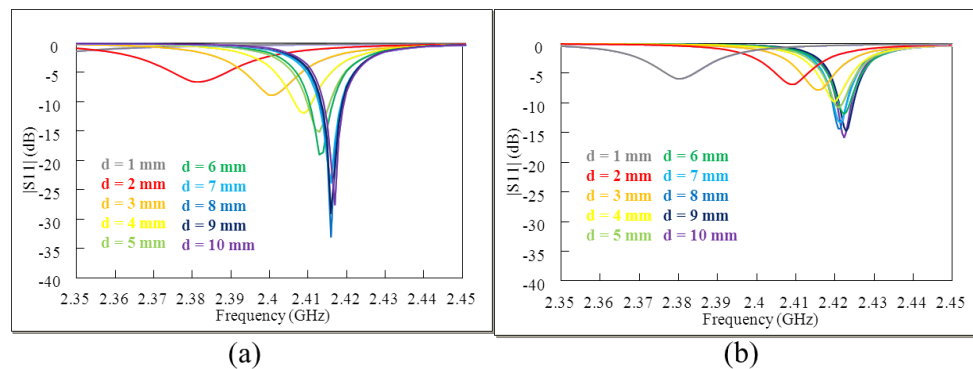


Figure 5.3.6 Frequency detuning of (a) horizontally and (b) vertically aligned spiral-antenna near a simple head model

Figure 5.3.7 shows the simulated radiation efficiencies of the antennas at different distances from the simple head model. It is observed that the best case is the vertically aligned L-antenna (polarization normal to the head) and the radiation efficiency is about 20%. However, when the L-antenna is aligned horizontally (polarization tangential to the head), the efficiency drops dramatically down to 2%. The differences are not as big for the spiral antenna, probably due to mixed polarization of the antenna. The radiation efficiency of the spiral antenna is above 5% with the d values higher than 1 mm.

It should be noted that the presented results are only preliminary and more precise investigations will be done in the near future using a more realistic head model and a BTE hearing aid device. However, these results may give some ideas how the antennas should be positioned inside a hearing aid device and behind an ear.

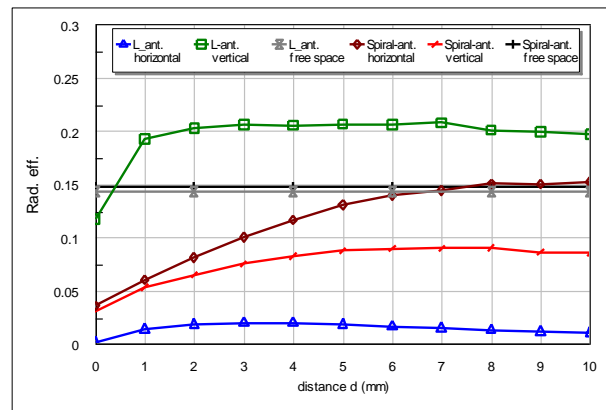


Figure 5.3.7 Radiation efficiencies of L-antenna and spiral antenna at 2.4 GHz when placed at different distances from the simple head model

5.4 Summary and next steps

First active antenna prototypes have been designed, manufactured and tested. The simulations have been compared with the measurements. The RF cable has an effect on the S_{11} and the radiation patterns of the antennas which is common when measuring small antennas. Some improvements in the results were achieved by using a balun around the measurement cable, especially with the spiral antenna.

Based on preliminary simulations with a simple head model, it seems that the spiral antenna is less sensitive to the head proximity than the L-antenna. The spiral antenna occupies a smaller area (4 mm x 4mm) than the L-antenna (4 mm x 8 mm) but it requires a thick substrate (~3mm) for adequate radiation efficiency. The thickness of the L-antenna is only about 0.5 mm.

As for the next steps, the antennas will be simulated with the SiP package, BTE hearing aid model and a more realistic human head model to investigate the effects of the surroundings on the antenna performance. Next antenna prototype versions will be optimized for the 3D SiP. The footprints of the antennas are harmonized with the miniature agile dipole antenna and interface of the SiP package.

6 CEA miniature agile antenna

6.1 Antenna structure

The antenna structure is based on a monopolar wire-patch antenna [1] which provides dipolar-like radiation characteristics. It is composed by two metallizations etched on each face of a dielectric substrate. The dielectric substrate characteristics (RO 4003) are $\epsilon_r=3.55$ and $\tan\delta=0.0027$. The lower metallic plate acts as ground and the upper metallic plate constitutes the antenna top hat. The antenna feeding is obtained by means of a probe connected to the top hat, through the ground plane and the dielectric substrate. A ground wire connects the top hat to the ground plane in order to achieve a low parallel resonance. By using a particular configuration of a slot into the antenna top hat, a significant reduction of the resonant frequency is obtained [2].

The slot shape modification into the antenna hat corresponds to a variation of the equivalent antenna capacitance. Hence a slot loading technique is used to control the operating frequency by placing a discrete varactor diode across the slot. A RF signal and a DC voltage source are used through a Bias Tee to feed the antenna and control varactor voltage. This agility method using slot and varactor diode loading allows a greater antenna miniaturization of the compact antenna structure.

The final compact agile antenna structure is depicted in Figure 6.1.1. The overall dimensions of the antenna are $5 \times 5 \text{ mm}^2$ by 2 mm high.

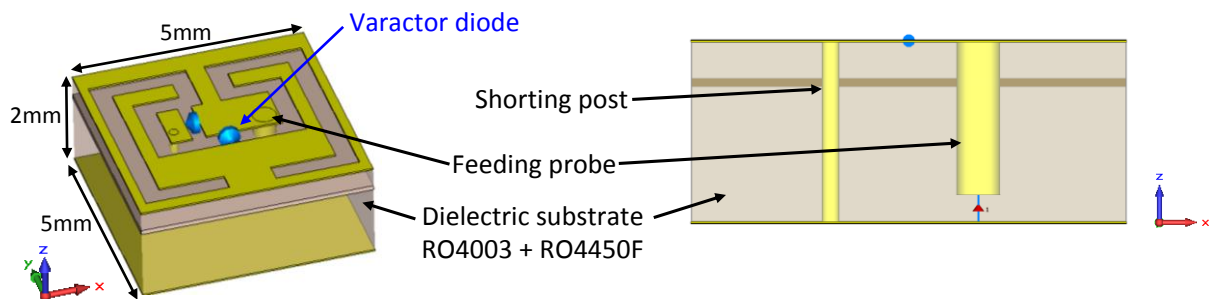


Figure 6.1.1 Perspective, top and side views of the antenna structure

6.2 Impedance agility simulated results

Antenna impedance is directly matched to 50 Ohms by means of various geometrical tuning parameters, which are not detailed here for sake of brevity. The varactor diode characteristics and the required DC voltage controls have been taken into account to optimize the antenna impedance matching. Simulated antenna input impedances and return losses for different capacitor values are respectively plotted in Figure 6.2.1 and Figure 6.2.2.

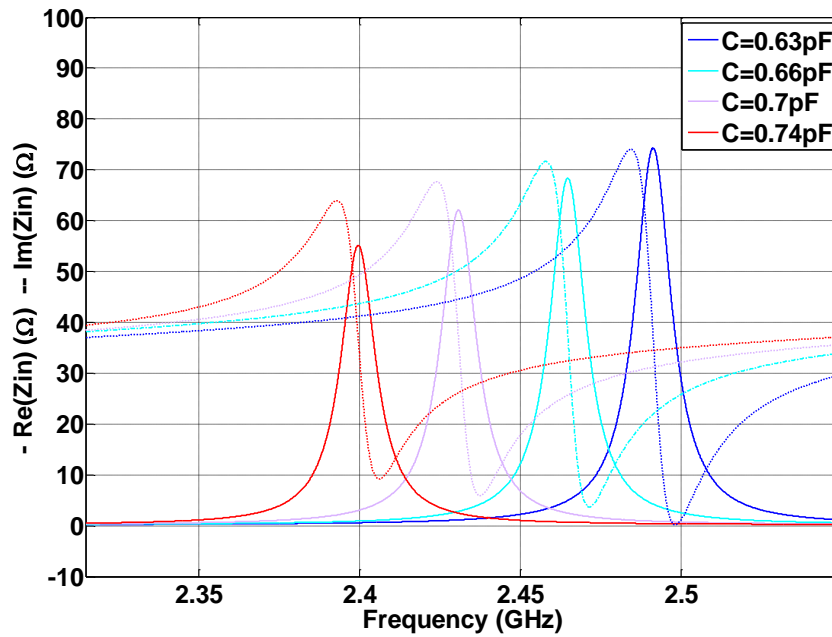


Figure 6.2.1 Input impedances for different capacitor values

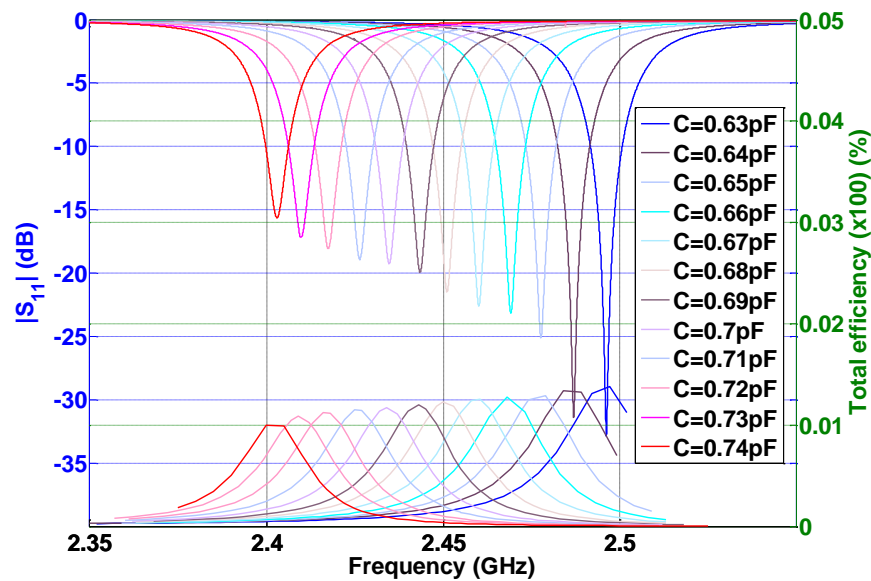


Figure 6.2.2 $|S_{11}|$ parameters and total efficiencies for different capacitor values

Simulation results show that the operating frequency can be continuously tuned over the band of interest for the WiserBAN project. Figure 6.2.2 also presents the total efficiencies on the right label for the different capacitor values i.e. for each covered channel. The total efficiency remains higher than 1% over the ISM band and includes both varactor diode and impedance mismatch losses. It should be noted that these capacitor values are obtained for varactor reverse bias voltages varying between 1V and 2V with a 0.02V step.

6.3 Methodology for antenna measurement

Measurement of such an antenna is a challenging issue given its small dimensions. A specific approach has to be established in order to compare measurements and simulation. In this subsection we present the measurement methodology and the obtained results.

The very low size of the antenna ground plane implies that antenna performances are disturbed by parasitic RF cable effects, which is needed for antenna measurements. Indeed, it can be seen on the Figure 6.3.1, that surface current on the cable is an integral part of the antenna. The radiated element is no longer the single antenna and has to be replaced by single antenna and the cable.

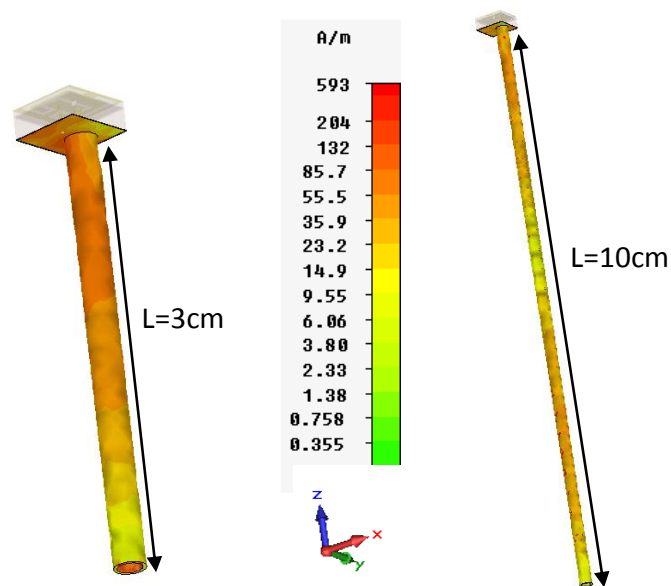
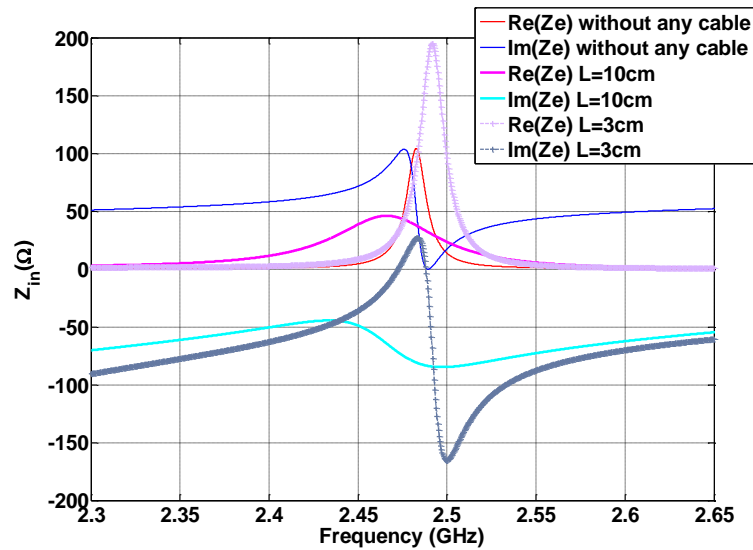
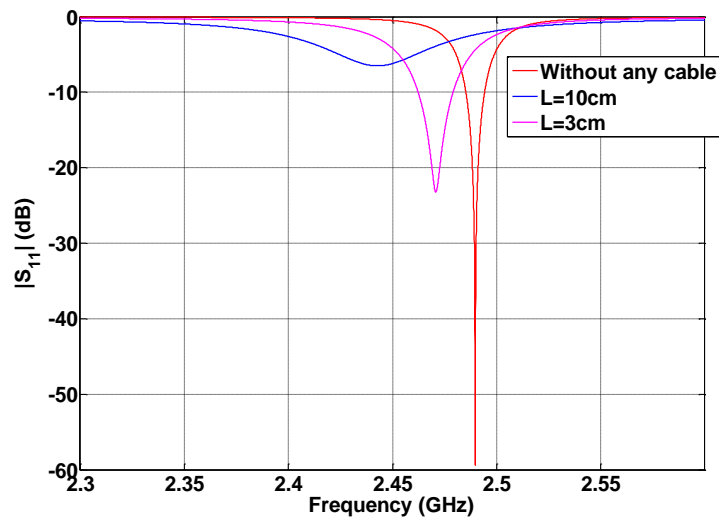


Figure 6.3.1 Surface current according to the cable

Depending on the cable length, both input impedance and $|S_{11}|$ parameter are modified (see Figure 6.3.2). Thus it is firstly necessary to control the antenna surrounding in order to properly compare measurement and simulation. For that purpose, a quarter wave length stub (bazooka cable) was integrated on the cable.



(a)



(b)

Figure 6.3.2 Input impedance (a) and $|S_{11}|$ parameter (b) according to the cable length L

The free end of the stub is an open-circuit, its length has been optimized to present a short-circuit on the shield of the coaxial feed cable (see Figure 6.3.3). To avoid the stub being in the antenna reactive area, the L distance (Figure 6.3.4) between the antenna and the stub has also been optimized. Thanks to this optimization the stub does not allow currents' cable going under it as shown the Figure 6.3.4.

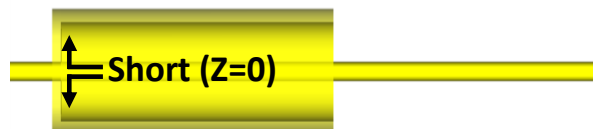


Figure 6.3.3 Integration of a quarter wave length stub on the RF feed cable

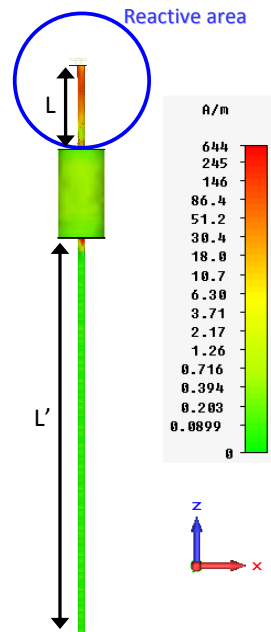
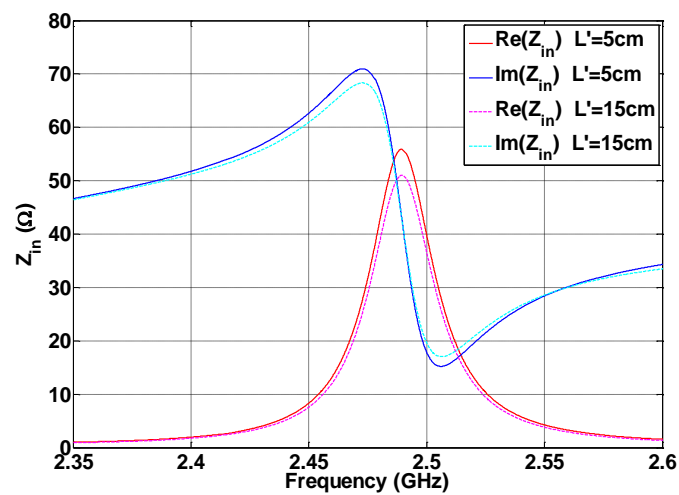
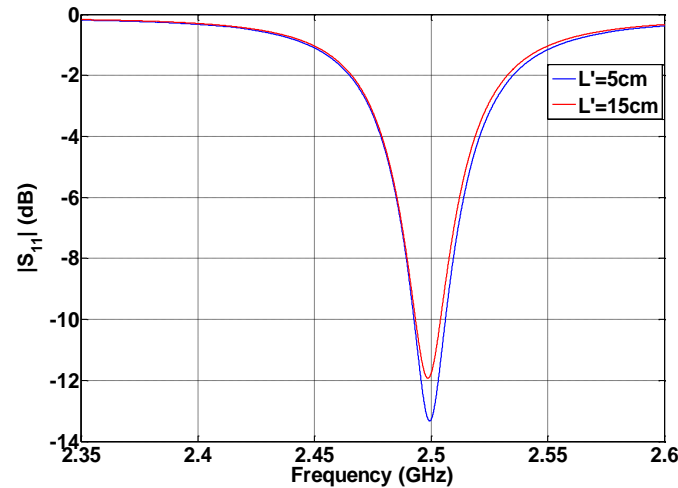


Figure 6.3.4 Surface current on the cable with the stub

In Figure 6.3.5 we present both input impedance and $|S_{11}|$ parameter when the stub is integrated. It can be noticed that the cable length and bias tee under the stub do not have any impact on impedance performances.



(a)



(b)

Figure 6.3.5 Input impedance (a) and $|S_{11}|$ parameter (b) according to the cable length L' under the stub

It should be reminded that the input impedance and $|S_{11}|$ parameter presented Figure 6.3.5 are the ones for the {antenna + stub} structure, they are thus different from those for the single antenna case. The new radiated structure, presented in Figure 6.3.6, will be hereinafter noted {antenna + stub} structure.

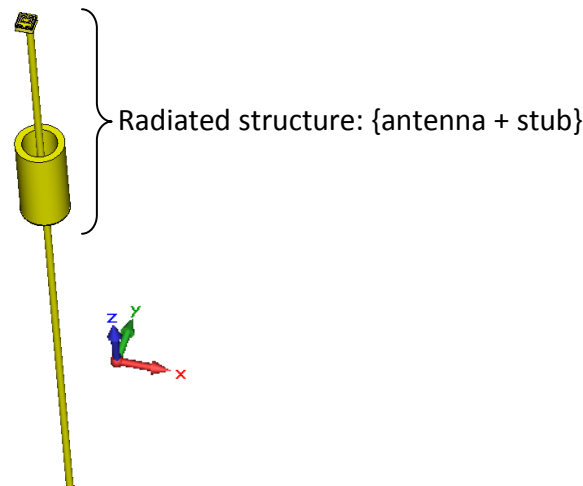


Figure 6.3.6 Radiated {antenna + stub} structure

6.4 Antenna prototype

A prototype {antenna + stub} was manufactured, by employing with a 0.64pF capacitance value on antenna hat (see Figure 6.4.1). Its global dimensions are 5mm x 5 mm x 2 mm, and the coaxial cable core core is directly feeding the antenna top hat. Taking into account the previous study, a quarter wave length stub is integrated on the RF feed cable (see Figure 6.4.1).

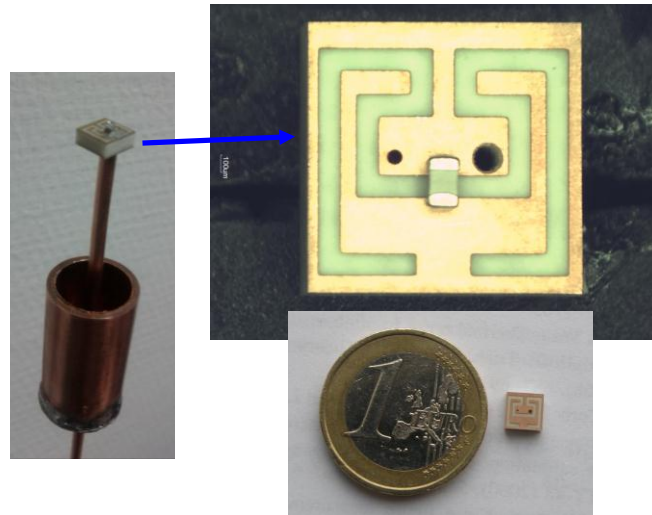
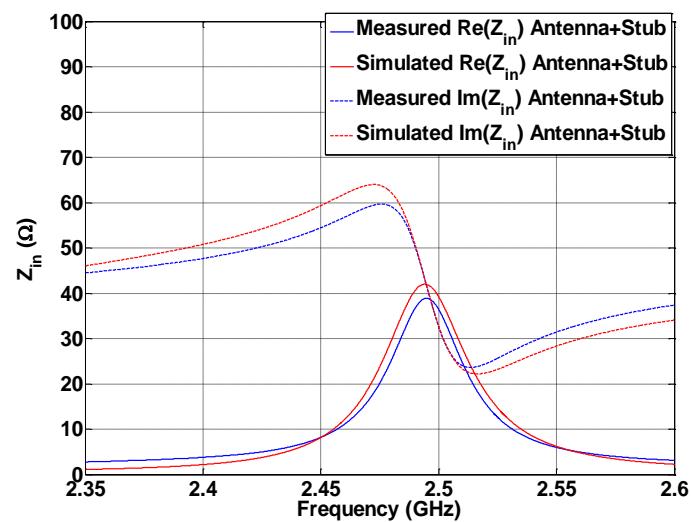


Figure 6.4.1 Prototype of the {antenna + stub} structure

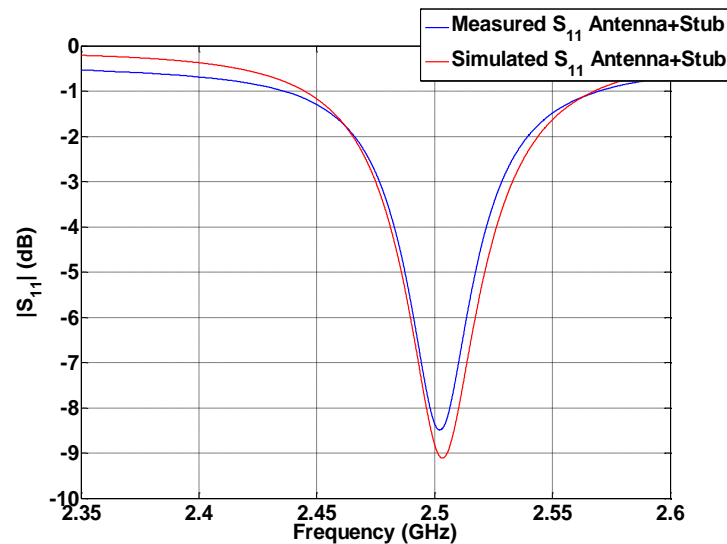
6.5 Impedance measurement

This sub section describes the measurement methodology to obtain consistent comparison between measurement and simulation.

Firstly, measured {antenna + stub} structure results were compared with the simulated ones of the same structure. Impedance performances (input impedance and $|S_{11}|$ parameter) present a very good agreement between simulation and measurement as shown in Figure 6.5.1.



(a)



(b)

Figure 6.5.1 Comparison between simulated and measured input impedance (a) and $|S_{11}|$ parameter (b) for the {antenna + stub} structure

The next step is to determine a transfer function between {antenna + stub} structure and single antenna structure. This is targeted to extrapolate the {cable + stub} effect on the performances to only have single antenna performances.

This transfer function is determined by means of the simulated {antenna + stub} and single antenna results. The Figure 6.5.2 illustrates the principles of the transfer function determination.

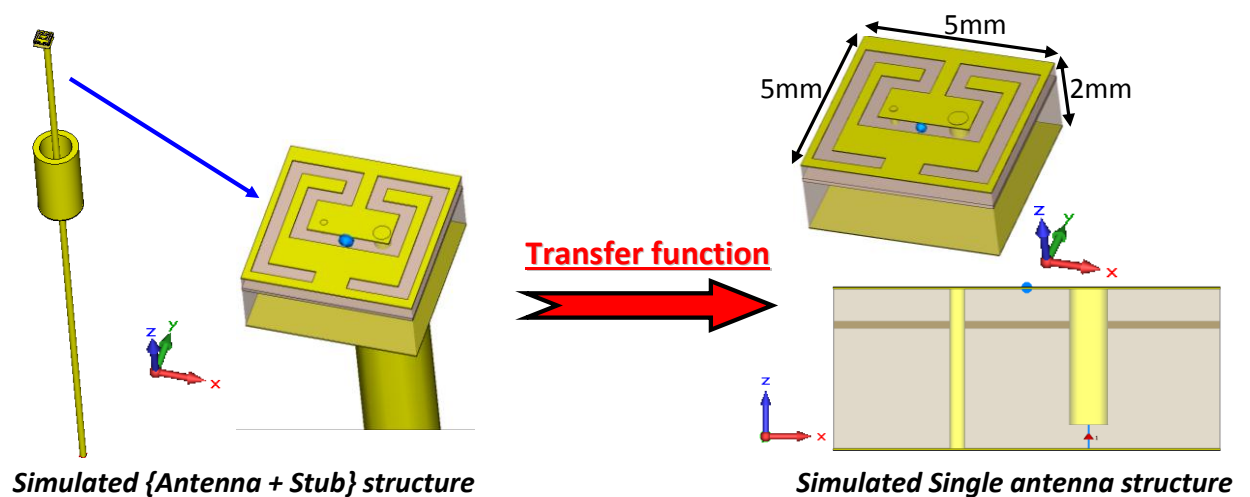


Figure 6.5.2 Determination of the transfer function

The definition of the transfer function from {antenna + stub} to isolated antenna results allows the extrapolation of the “measured single antenna” results from those obtained with the stub.

The comparison between simulated and measured single antenna results obtained by the method presented above is presented in Figure 6.5.3.

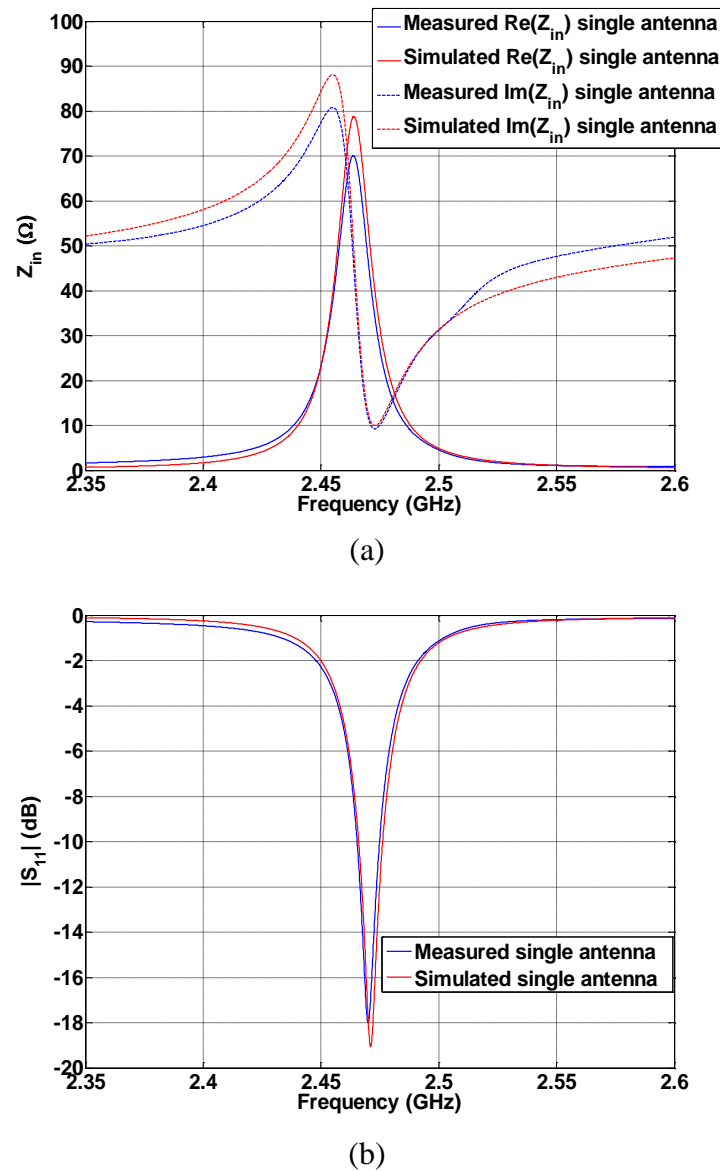


Figure 6.5.3 Comparison between simulated and measured input impedance (a) and $|S_{11}|$ parameter (b) for the single antenna structure

It could be notice that the measured single antenna is covering much more one channel of the ISM band. The excellent agreement between measured and simulated impedance results, which validates the antenna design as well as the proposed methodology.

6.6 Radiation performances

6.6.1 Isolated antenna simulations

Radiation and directivity patterns present omnidirectional properties. The 3D directivity pattern at 2.47 GHz, corresponding to the resonant frequency of the

antenna loaded by the 0.64 pF capacitor, is presented Figure 6.6.1. The antenna mainly radiates linear polarization as shown by radiation patterns in xOy and yOz planes presented in Figure 6.6.1.

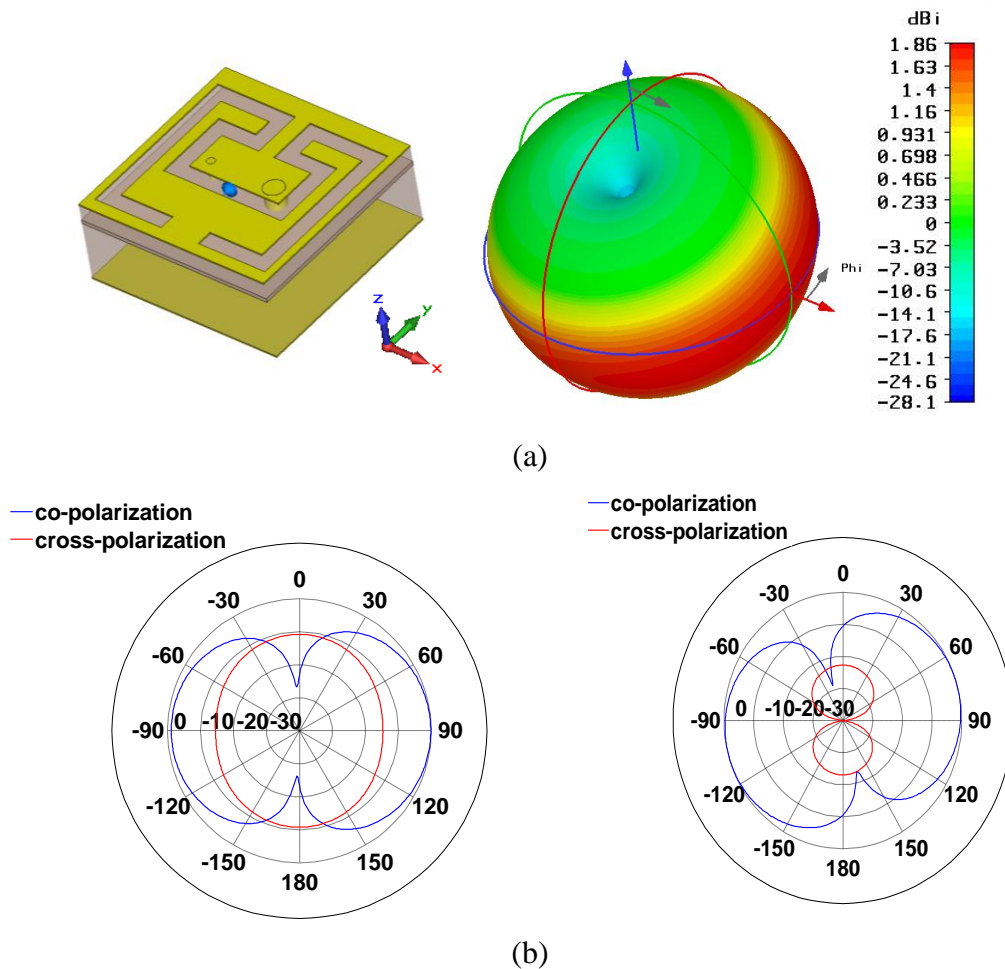


Figure 6.6.1 3D directivity pattern at 2.47 GHz (a) and Antenna radiation patterns: xOz (left) plane and yOz (right) (b)

Radiation null of the dipolar pattern is tilted with respect to z-direction in the yOz plane because of the off-centered feeding. The maximum realized gain for the single antenna in the air is -18.5 dBi.

6.6.2 Measurement results

Radiation properties in three plane, i.e. xOy, yOz and xOz planes, have been measured in an anechoic chamber as presented Figure 6.6.2.

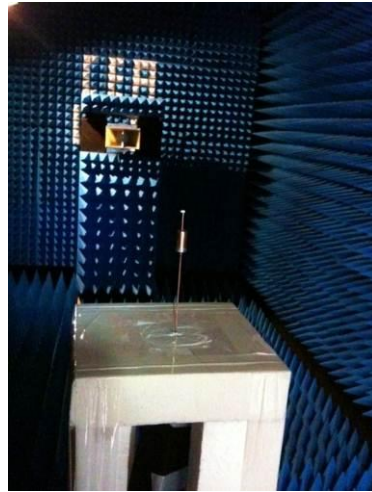


Figure 6.6.2 Antenna measurement in the anechoic chamber

Figure 6.6.3 is presenting the comparison between measured and simulated total normalized realized gains.

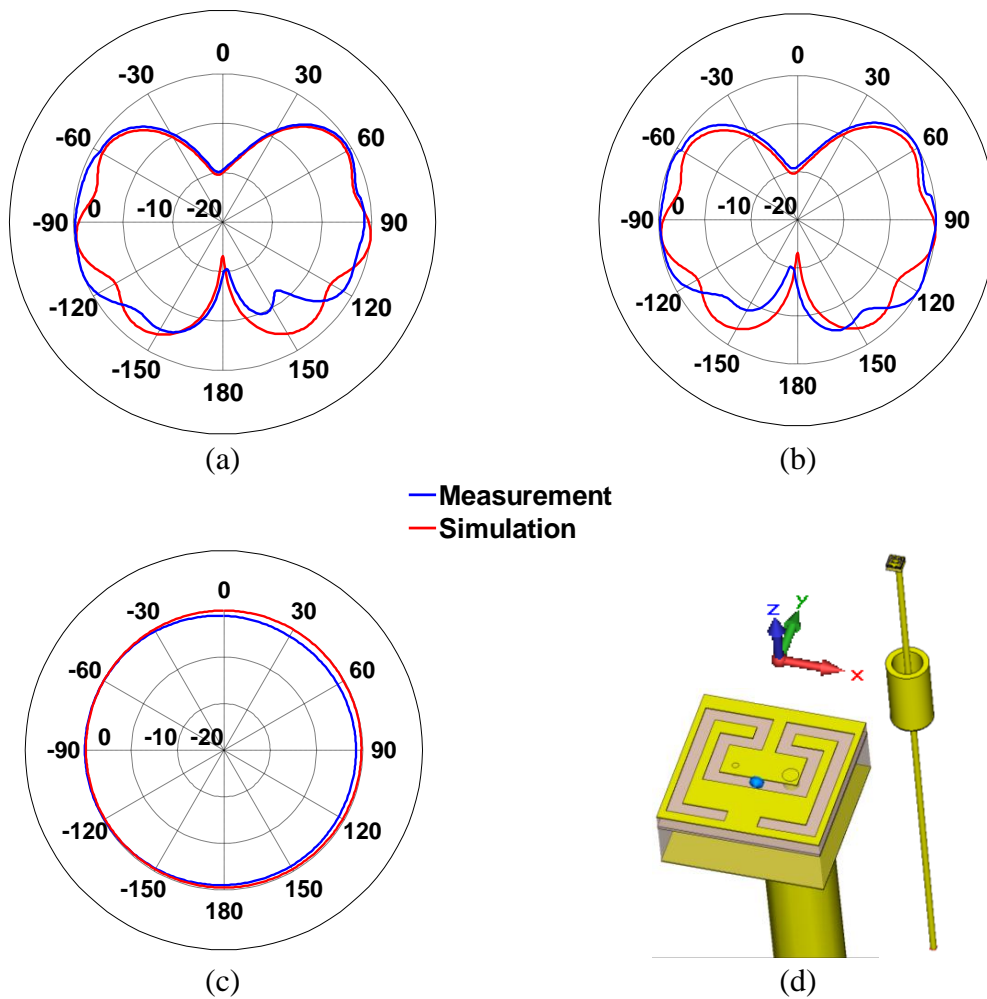


Figure 6.6.3 Radiation pattern in the xOz (a), yOz (b) and xOy (c) planes and respective coordinates of the structure (d)

Since the antenna mainly radiates on a linear polarization along z-axis, here we present the total radiation pattern (normalized to the maximum). In each plane, the measured maximum realized gain is equal to -12.7 dBi when the simulated one is -12.2 dBi. The {antenna + stub} structure presents omnidirectional properties in both measurement and simulation.

6.7 Antenna characteristics in the ear

The integration of two antennas, i.e. within each auditory canal was investigated by simulating the human head as a homogeneous Specific Anthropomorphic Mannequin (SAM) phantom. The auditory canal is modeled as a cylindrical hole of 10 mm diameter and 20 mm length. Two antennas' orientations inside the canal have been studied: normal and tangential orientations as shown Figure 6.7.1. The location inside the ear, i.e. the distance d (see Figure 6.7.1) between the two antennas has also been investigated. Both studies are discussed in this section.

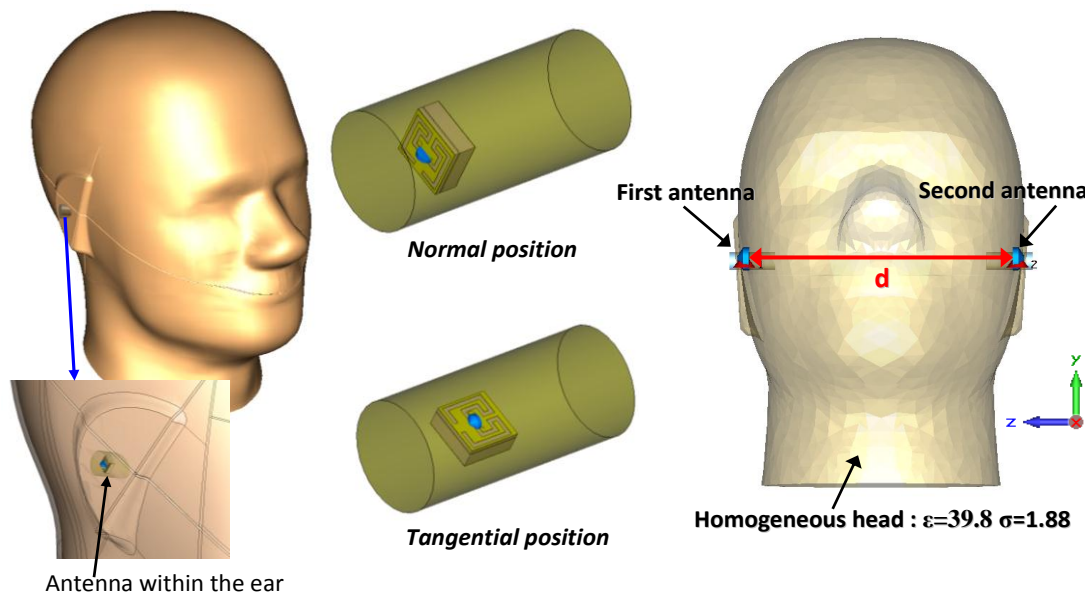


Figure 6.7.1 Investigation on the head influence

6.7.1 Antenna orientation inside the auditory canal

The study of tangential and normal positions with respect to the head surface is presented in this subsection. This is performed for a same d distance between antennas equals to 150mm. Effects of both orientations inside the head on the input impedance real part and on the $|S_{11}|$ parameter are respectively presented Figure 6.7.2 and are compared with the free space case.

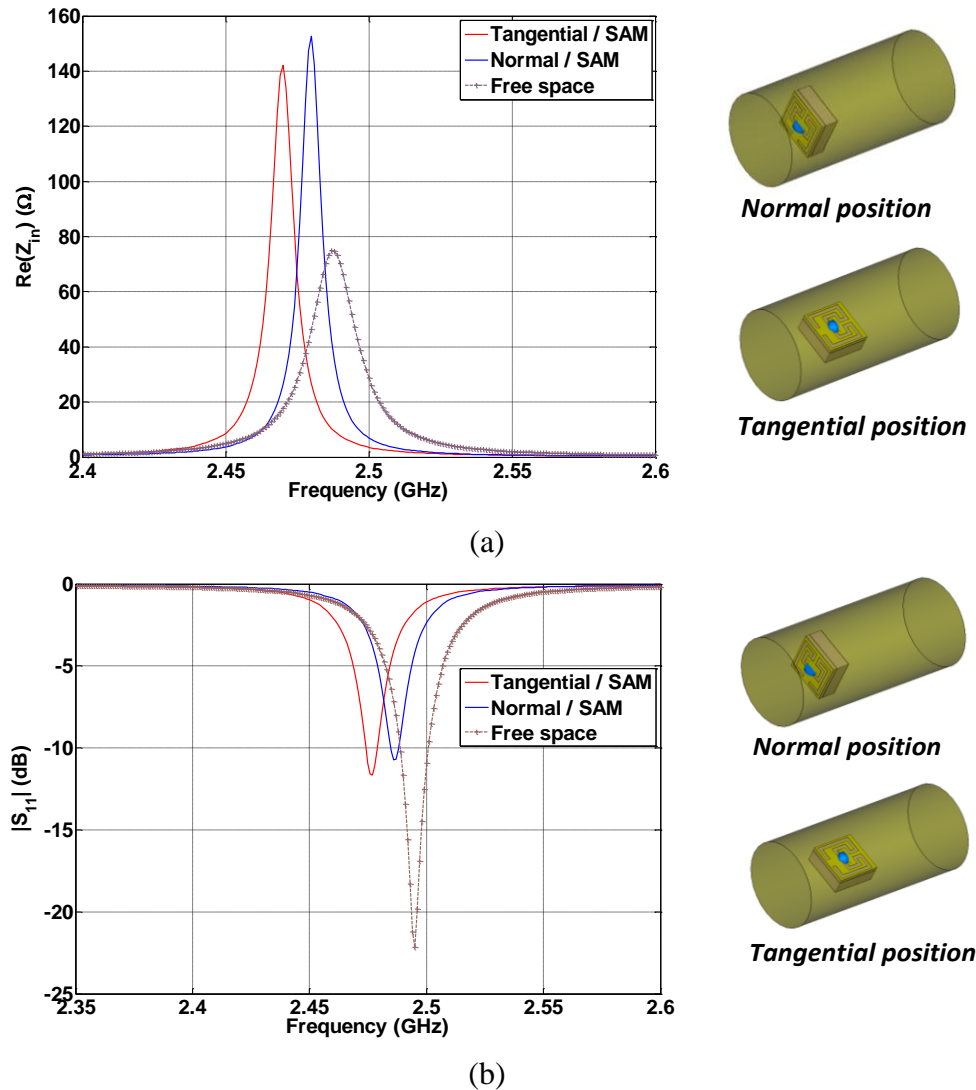


Figure 6.7.2 Input impedance (a) and $|S_{11}|$ parameter (b) for head and free space cases

The comparison between head scenarios and free space case shows an increase of the input impedance real part for head cases which is involving the decrease of the impedance bandwidth as shown by the $|S_{11}|$ parameter. Moreover, there is a decrease of the resonant frequency induced by presence of the human tissue, which differs according to the antenna orientation. Indeed, in the tangential orientation case, the auditory canal is more visible. However, for both orientations, the frequency detuning can be compensated by changing the capacitance value of the varactor diode.

The coupling between the two antennas can also be evaluated by presenting the $|S_{21}|$ parameter Figure 6.7.3. Because of the detuning effect showed previously, the frequency axis is normalized with respect to the matching resonant frequency f_0 , which is lower when placed in the ear.

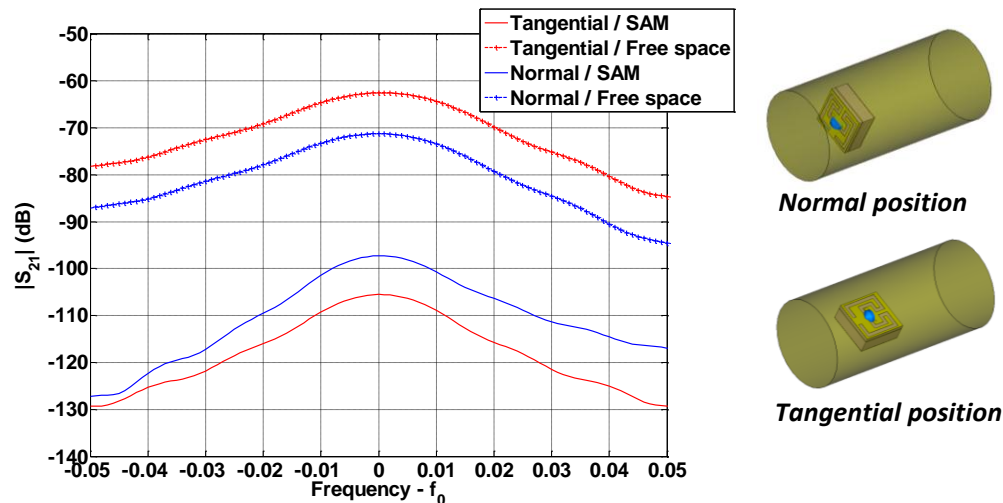


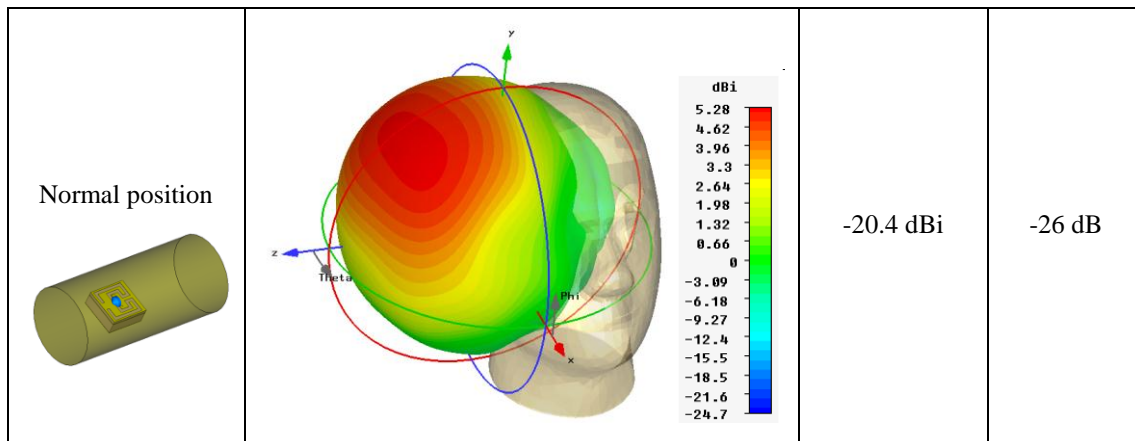
Figure 6.7.3 $|S_{21}|$ parameter for head and free space cases

It is interesting to notice that the losses are higher in the tangential position than in the normal once the antenna is in the ear. This can be explained by the fact that propagation occurs by creeping waves around the head, which are generated by normal electric field.

The Table 6.7.1 summarizes the 3D directivity patterns and antenna performances for both orientation scenarios.

Table 6.7.1 3D directivity patterns and antenna performances for both orientation scenarios

	3D directivity pattern	Maximum realized gain	Total efficiency
Tangential position		-24.9 dBi	-30 dB

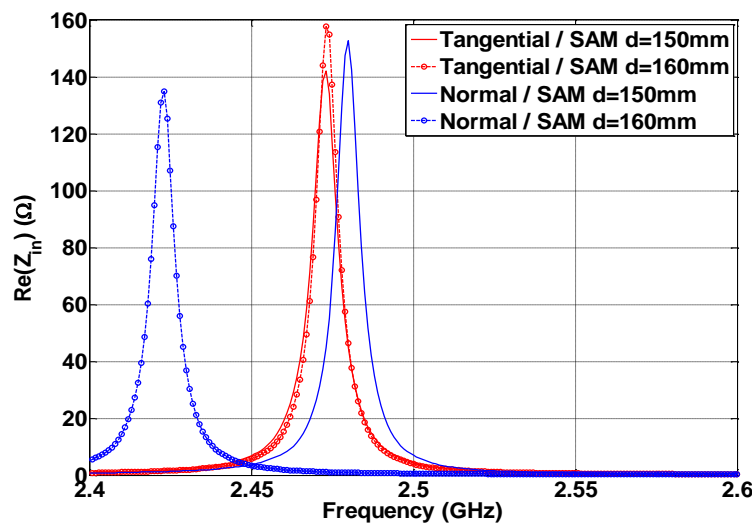


It can be noticed that the directivity pattern is disturbed by the human head. Compared to the antenna free space case, which owns an omnidirectional pattern, antenna inside the head has directional radiation properties. The normal position presents best performances on terms of maximum realized gain and total efficiency.

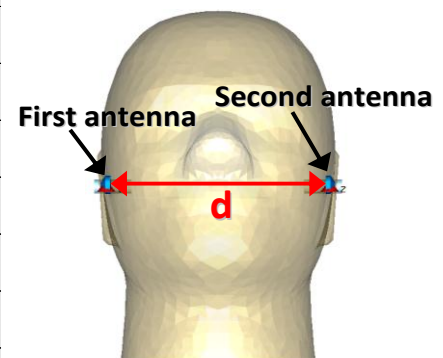
The head scenario study can be improved by the investigation of the influence of the antenna location inside the ear, i.e. the d length defined Figure 6.7.1.

6.7.2 Antenna depth inside the auditory canal

Two d lengths are studied, i.e. 150 mm and 160 mm for both orientations. Figure 6.7.4 shows the real part of the input impedance and the $|S_{11}|$ parameter according to the d length and antenna orientations.



(a)



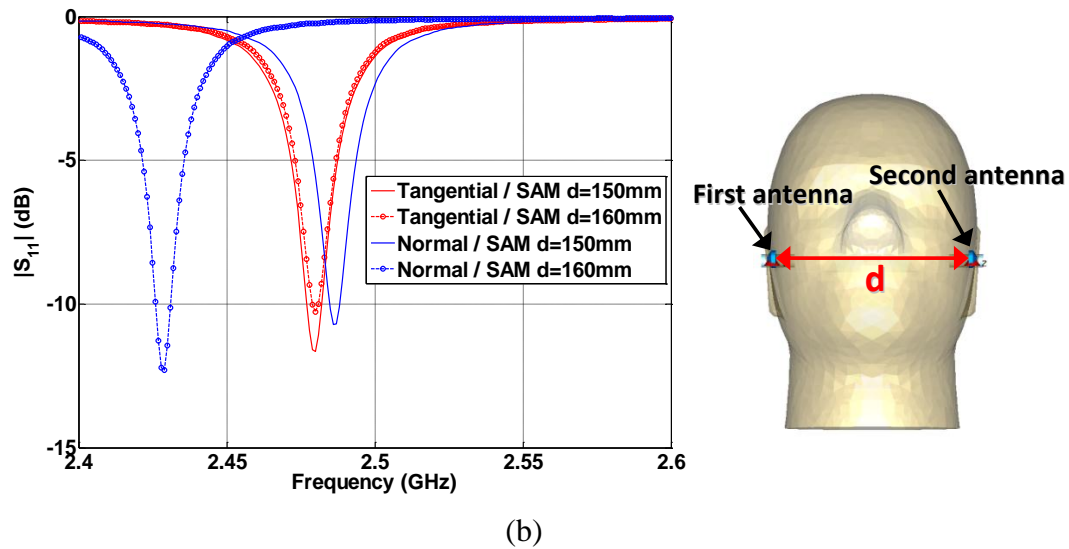


Figure 6.7.4 Input impedance (a) and $|S_{11}|$ parameter (b) for different d lengths and orientations

Depending on the antenna orientation, the d length has a clearly different influences on the input impedance and thus on the $|S_{11}|$ parameter. The input impedance for the tangential orientation of the antenna remains almost unchanged regardless to the d value. On the contrary, for the normal orientation, between 150 mm and 160 mm the resonant frequency and so the impedance matching band is changed. This behavior can be explained by the electrical nature of the antenna and the greater interaction with dielectric material for this field configuration. Nevertheless the detuning effect in different antenna position can be smartly compensated by changing the capacitor value in this active antenna solution.

Concerning the coupling, Figure 6.7.5 shows the $|S_{21}|$ parameter for different d lengths and orientation. As previously, because of the frequency detuning, the frequency axis is normalized with respect to the matching resonant frequency f_0 .

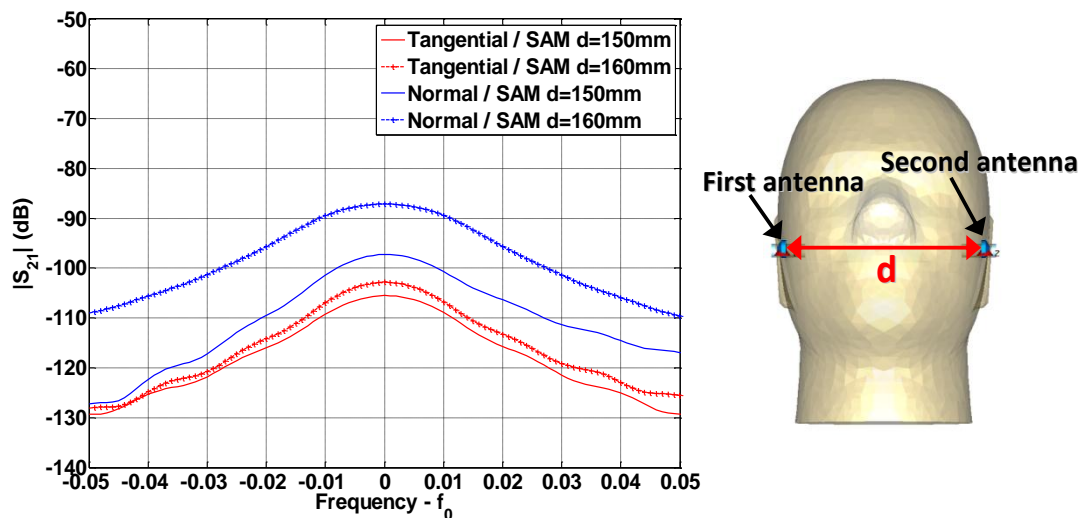
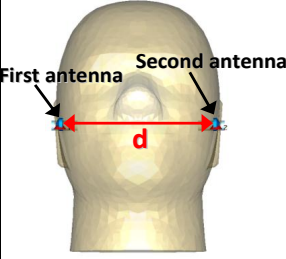
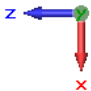
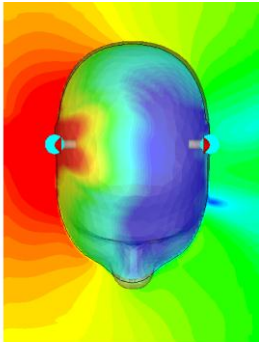
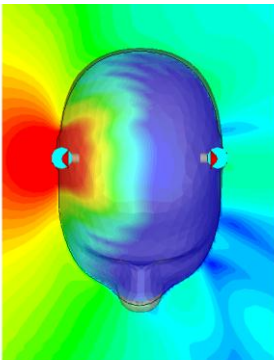
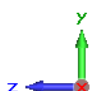
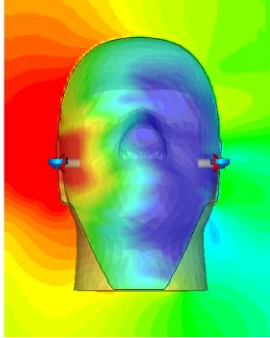
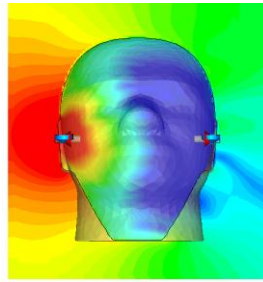


Figure 6.7.5 $|S_{21}|$ parameter for different d lengths and orientations

Unusually, the nearest the antenna are, the lower the $|S_{21}|$ amplitude is. Since the antenna is inside the auditory canal when d is equal to 150 mm, fields are more confined in lossy medium than when the d length equals 160 mm (see Table 6.7.2) and antenna efficiency is lower. Indeed, the 160 mm length corresponds to the boundary of the outer ear canal. Moreover at this distance the propagation takes advantage of creeping waves, being the antennas closer to the body surface. Therefore losses are smaller at $d=160$ mm than at $d=150$ mm.

Table 6.7.2 E fields inside the head for normal orientation

		d=160mm	d=150mm	dBV/m 20.0 16.1 13.0 9.84 6.72 3.59 0.469 -2.66 -5.78 -8.91 -12.0 -15.2 -18.3 -21.4 -24.5 -27.7 -30.0
 Normal position				
				
	$ S_{21} $	-89 dB	-95 dB	

6.7.3 Ear to ear channel

An analytical formula of the field amplitude attenuation around the head derived from diffraction theory [3] has been used:

$$A_{dB} = -3 + \alpha_{dB/cm} \frac{p}{2} + 10 \cdot \log(p) \quad (1)$$

with p the head perimeter in centimeter and α the decaying factor equals to 1.2 dB/cm in the head case at 2.4 GHz.

Table 6.7.3 shows that the amplitude attenuation model around the head is a good approximation of the ear-to-ear radio channel since the simulated $|S_{21}|$ values are in good agreement with the calculated value using (1).

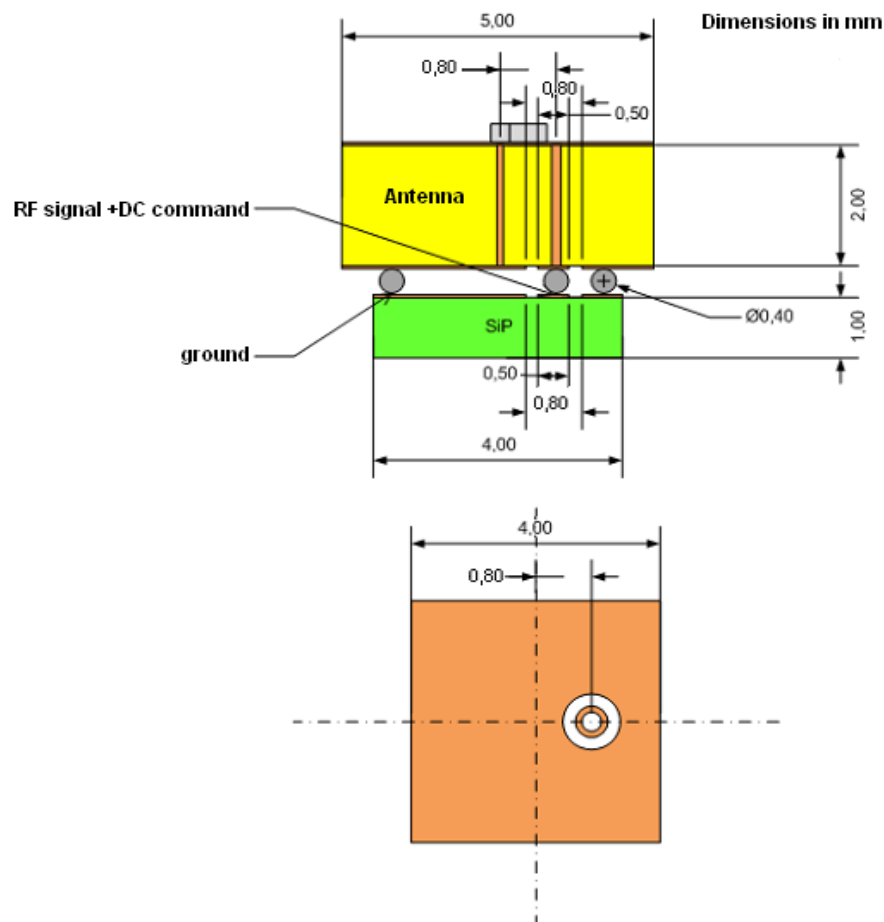
Table 6.7.3 Amplitude attenuation model compared with the $|S_{21}|$ parameter

		$ S_{21} $ (dB)		-AdB-2*Gmax (dB)	
d (mm)		150	160	150	160
Head case	Tangential	-104	-100	-105.5	-102.8
	Normal	-95	-89	-97.2	-87.1

6.8 Antenna/SiP interface

The CEA active antenna feeding is composed of both RF signal and DC command. Thus, the SiP output pad, i.e. the antenna interface with the SiP has to present both RF and DC commands. To fit with the antenna input, pad has to be off-centered and present a 0.8 mm offset only in one direction (x or y) as presented on the Figure 6.7.6.

Concerning the DC voltage, it remains lower than 2 Volts. The latter is corresponding to the 0.74pF capacitance value, and allows covering the first channel of the ISM band.

**Figure 6.7.6 Side and top view of the antenna - SiP layout**

7 CSEM passive loop antenna for cochlear implant

7.1 Introduction

The initial topology comprises a basic circular loop antenna. The loop is made of a golden wire and the whole structure is emerged in a silicone cylinder. The main performance parameters were simulated for a loop antenna in a generic configuration and the results are presented in Table 7.1.1. If a circular loop antenna is integrated in the existing cochlear implant the radiation properties will be obstructed by the inductive coupling loop and the fixation magnet (see Figure 7.1.1 left part). The placement of these components decreases the intensity of the magnetic field passing through the loop. Consequently the radiation resistance is decreased. The radiation and loss resistances of an antenna determine the overall radiation efficiency. The loss resistance of a single-turn small loop is generally much larger than its radiation resistance. Thus the radiation efficiency is normally very low. To increase the radiation efficiency, a folded loop antenna is proposed.

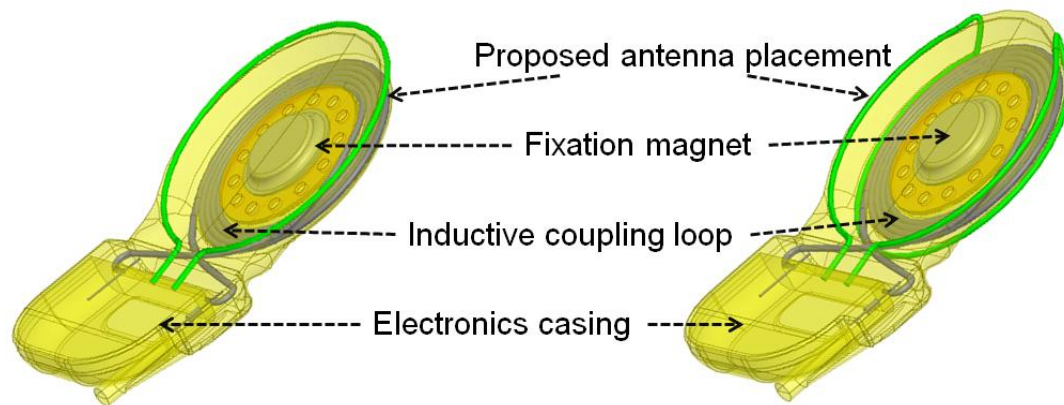


Figure 7.1.1 Topology of the integrated loop antenna: circular loop antenna (left), folded loop antenna (right)

The folded loop antenna is presented in Figure 7.1.1 (right). It occupies the outer rim of the silicone casing. This topology provides a higher radiation resistance as it does not have a magnetic field which is concentrated in the middle of the implant disc.

Table 7.1.1 Performance parameters of a loop antenna

Parameters	Comments	Values	Units
Dimensions	For the initial prototype	28x28x3.8	mm
Frequency range	Simulated for -10 dB S11 level	2.37–2.58	GHz
Instantaneous BW	At 10dB return loss level	200	MHz
Input impedance	At 2.45 GHz, normalized to 50Ω	1.27-0.31j	
VSWR	For the freq. range 2.4–2.5 GHz	≤ 1.75	
Gain	Realized total gain	-0.1	dBi
Radiation pattern	Similar to dipole antenna	80	degrees

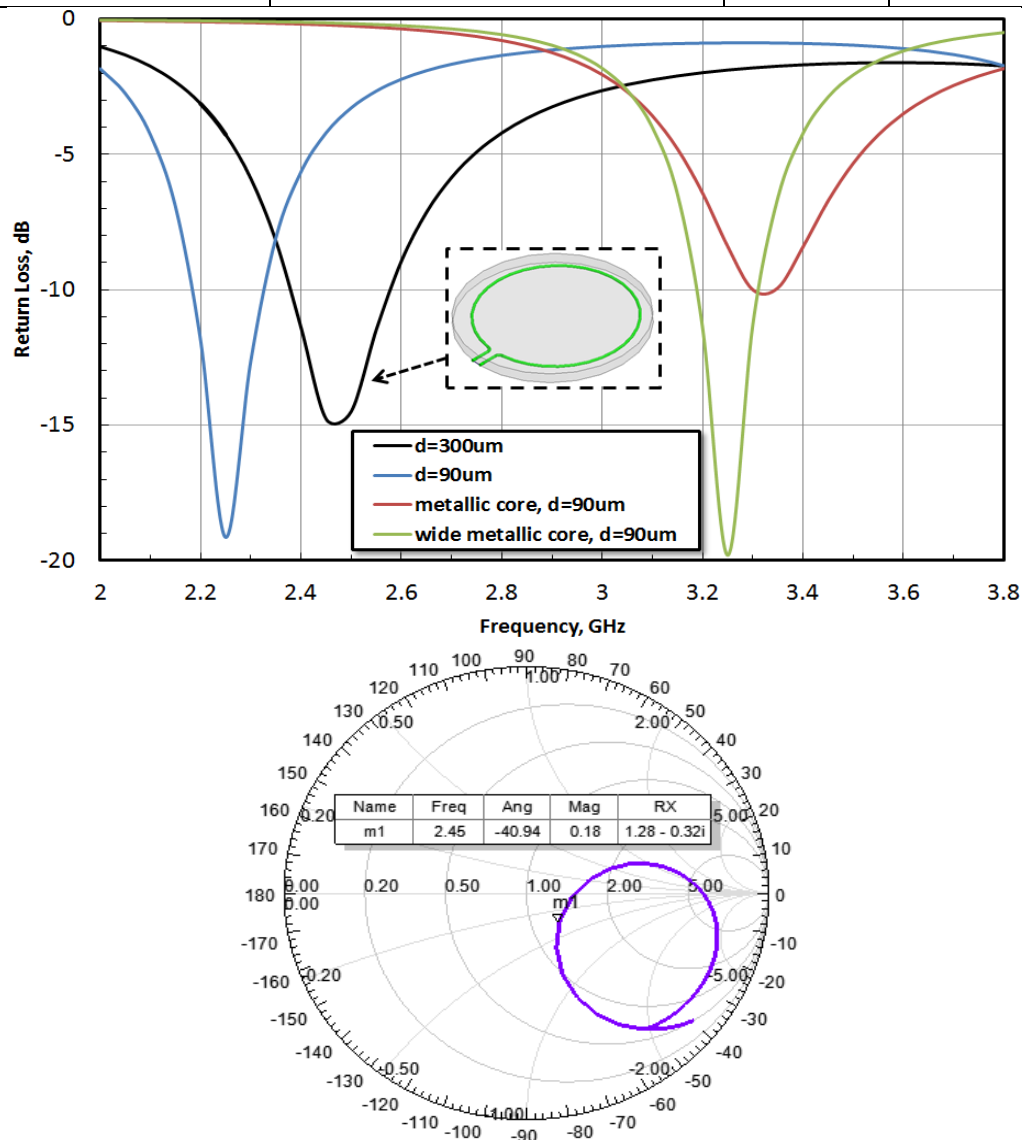


Figure 7.1.2 Simulated performance characteristics for the integrated loop antenna: resonance frequency detuning in different configurations (above), matching for a generic loop antenna (below)

A loop antenna immersed into a slab of silicone has been simulated with golden wires having radii of 300 and 90 μm (black and blue curves in Figure 7.1.2). The initial antenna structure with the wire diameter of 300 μm is perfectly matched to 50 Ω . When a metal object is inserted inside of the loop the resonance frequency is considerably detuned to a higher frequency. The red curve in Figure 7.1.2 presents S_{11} for the loop antenna where the volume of the fixation magnet is filled with metal. The green curve presents the same loop antenna with the magnet and the inductive coupling loop simulated as solid metal objects.

7.2 Matching circuit principle

Matching an antenna means retune its resonant frequency to properly radiate in the adequate bandwidth. To match the antenna, a dedicated circuit and its corresponding PCB are required. The aim of this chapter is to describe how the antenna can be matched. The chapter is organized as follows. First an overview of different types and topologies of circuits applicable in our case. Then follows a description of the test bench and the methodology that has been applied. And finally the measurement results.

To match the antenna, a circuit is required to properly retune the antenna in an adequate resonant frequency and to compensate for the fluctuations of the various uncertainties (magnet in the center, head and brain permittivity, coil next to the antenna). It is very difficult to take into account these fluctuations and uncertainties during modeling and simulation of the antenna. The matching circuit developed is a static design.

Figure 7.2.1 describes this matching circuit. The ports J2A.1 and J2A.4 represent the connections for the coil that will receive energy for charging the battery implant while J2A.2 and J2A.3 are the antenna ports. Using this circuit allows for flexible matching of the antenna because it gives some degrees of freedom (generally only two components are sufficient, but adding additional components offers us greater flexibility as described below). To get a larger bandwidth and to realize a large impedance ratio, more than two matching components are needed in the matching network.

It is simple to design a L, PI or T matching network. It's also possible to use in the same time a balanced to unbalanced circuit topology. This balanced to unbalanced (balun) structure consists of a Pi circuit in one of the 2 branches and a T-shaped structure on the other branch.

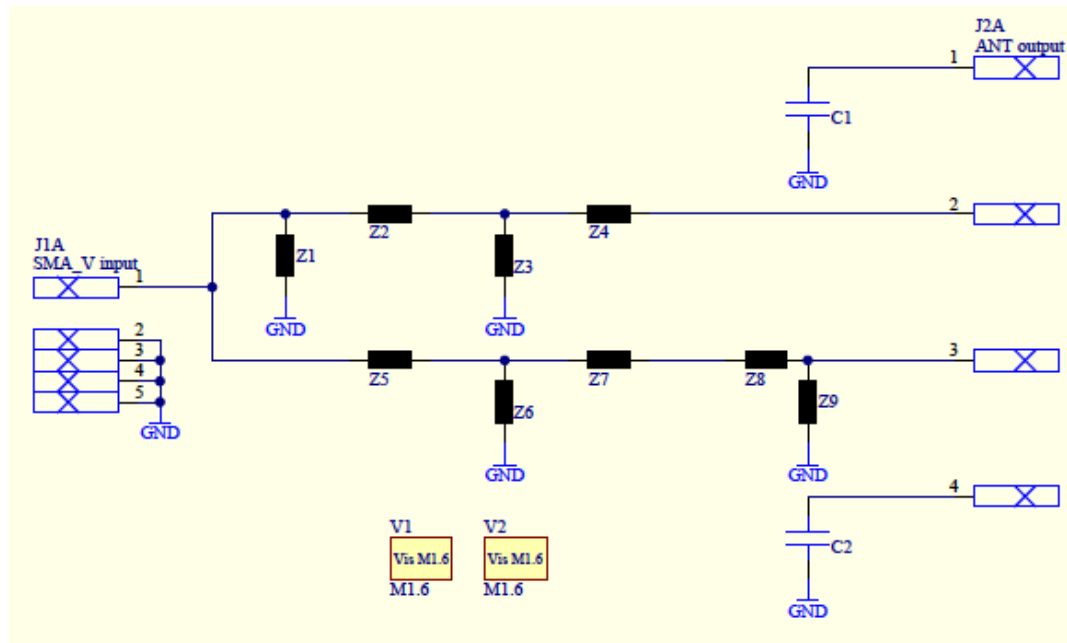


Figure 7.2.1 Schematic of the matching PCB

7.3 Implementation of the matching circuit

Figure 7.3.1 shows the manufactured PCB corresponding to the previous schematic. Purpose of this small PCB is just to measure the impedance of the antenna with and without the matching network and to finally give the right matching topology to implement. The top and bottom sides are shown. Overall size is around 20mm x 25mm. Finally a SMA connector is soldered on the top of this PCB.

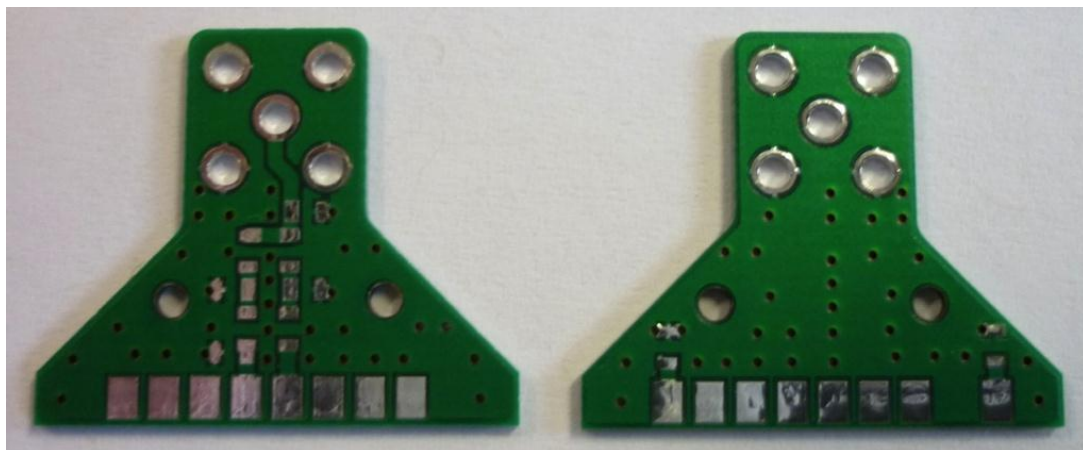


Figure 7.3.1 The matching PCB circuit

Figure 7.3.2 presents the matching PCB circuit connected to the loop antenna. The connection is made through the header used by Medel. The pitch between two consecutive pins is 2 mm. The PCB is inserted between the two rows of pins. The

substrate used for this prototype is FR4 with a thickness of 0.8 mm. Finally this matching circuit will be reproduced on the final PCB of the prototype. In the following chapters, the term classical loop antenna is used and is opposed to the folded loop antenna.

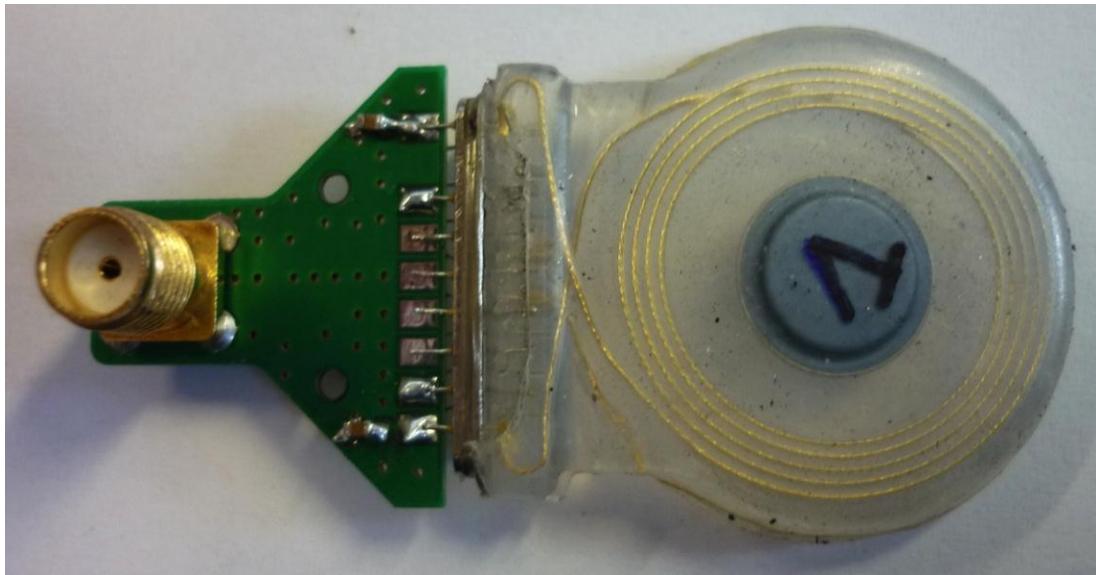
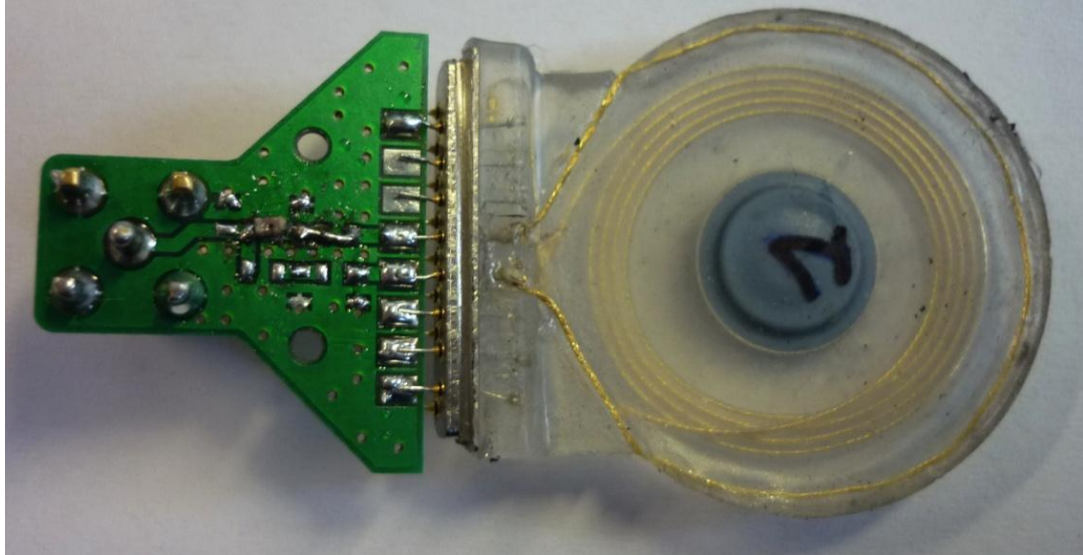


Figure 7.3.2 The matching PCB circuit connected to the antenna (classical loop), top and bottom

7.4 Test bench and measurement setup

7.4.1 Test bench

The following assumptions have been made (see schematic on Figure 7.2.1):

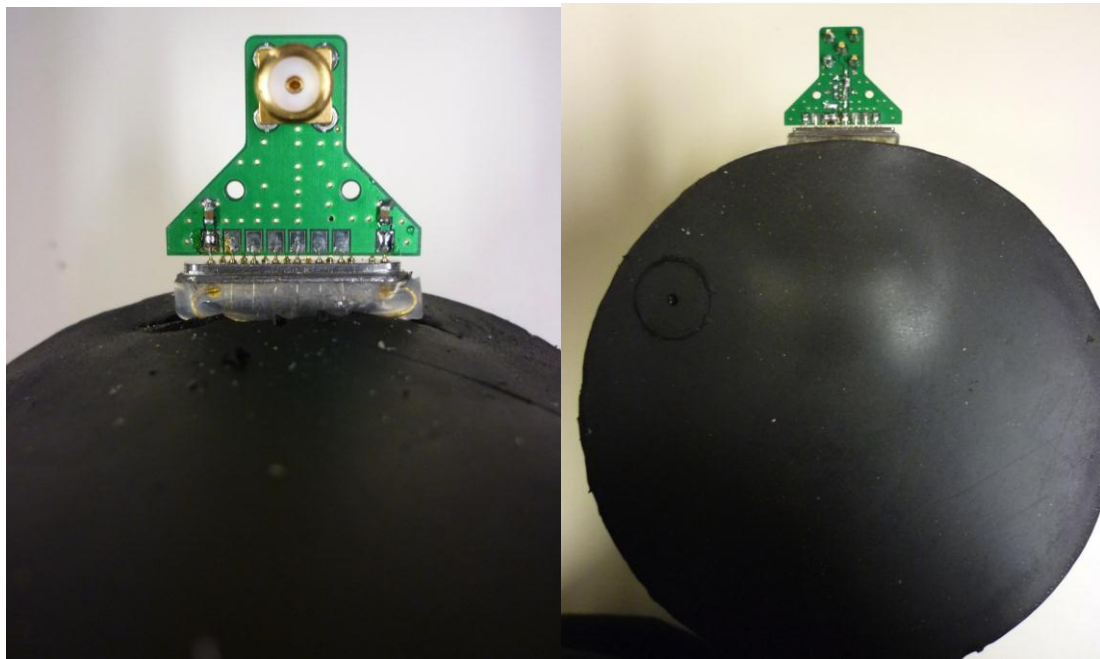
C1 and C2 are chosen equal to 6.8 nF in such a way that the external coil is RF grounded in the 2.4 GHz band.

The following configuration is used to measure and characterize the input impedance:

- Z_2 , Z_4 and Z_9 are shorted
- Z_1 , Z_3 , Z_5 , Z_6 , Z_7 and Z_8 are left opened

The head environment is modeled by using a special narrow band solid gel recreating environment of head (brain, bones, etc.). It is coming from Speag (reference number is MSL2450V2) and this gel is compliant to the following standards: CELENEC EN 50361 / IEEE Std 1528-2003 / IEC 62209/CD / FCC OET Supplement C.

Figure 7.4.1 show the antenna and its matching PCB inserted inside the special head gel.



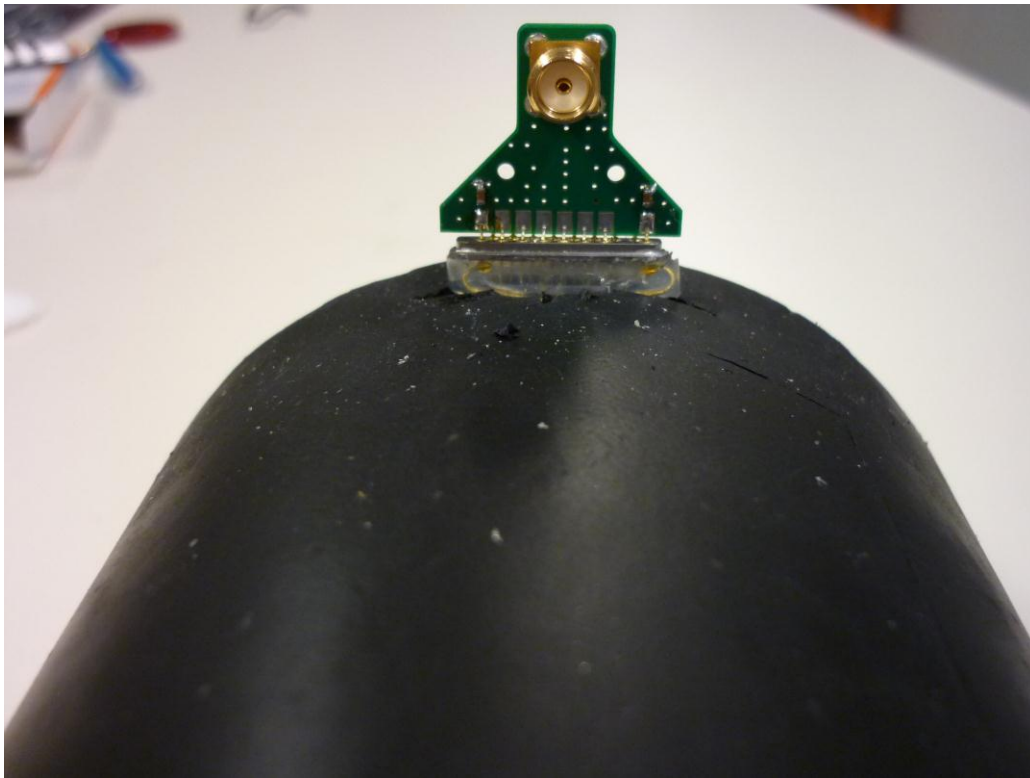


Figure 7.4.1 Antenna and its matching PCB inserted inside the gel

Two samples of the classical circular loop antenna are characterized. The main difference between samples 1 and 2 is the diameter of the wire: Sample 1 is using a 300 μ m diameter wire while sample 2 is using a 90 μ m wire. Two additional samples of the folded loop antenna were also characterized. Difference between samples 3 and 4 is the diameter of the wire: Sample 3 is using a 300 μ m diameter wire while sample 4 is using a 90 μ m wire.

Figure 7.4.2 shows the classical circular loop antenna (left) and the folded loop antenna (right).

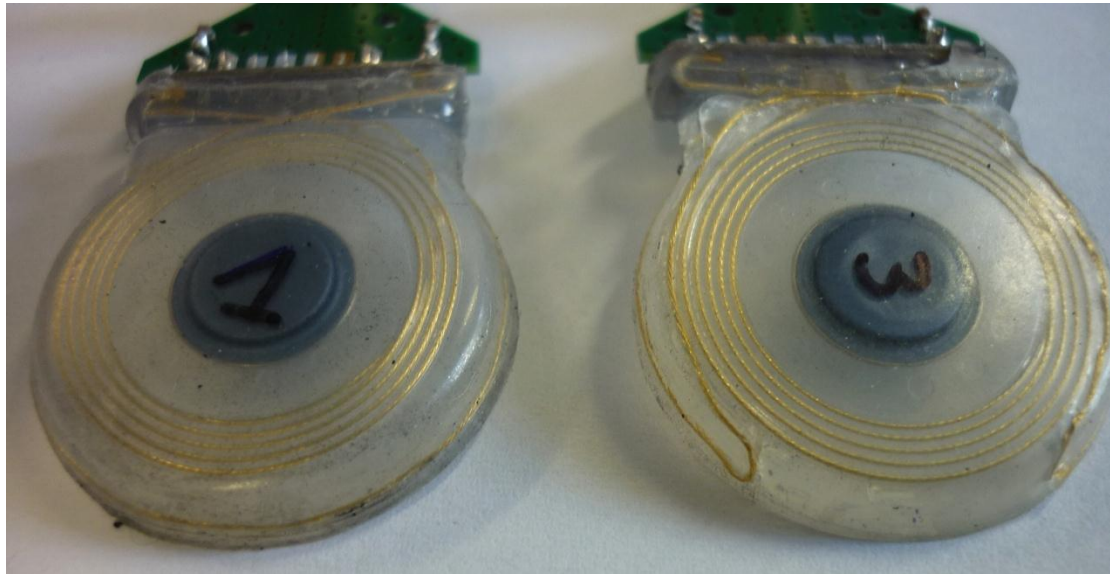


Figure 7.4.2 Classical and folded loop antenna

It is important to note that ferrites are used to prevent or reduce the influence of the RF current leaking into the outer surface of the coaxial feeder line. The ferrites have the same behavior than a $\lambda/4$ -choke (conductor based).

Another effect of these leaking current occurs in the measurement of electrically small antenna radiation pattern. These cable currents will participate to the radiation and radiate along with the antenna. This unwanted and undesirable radiation will then indicate a larger aperture and thus higher performances (gain, efficiency) than the real one. The smaller the antenna is and bigger is the impact leading to unrealistic optimistic results. Suitable anti-parasitic component (ferrite or conductor -based) must be implemented to ensure accurate measurements and results.

The size and dimension of the ground plane, in case they are smaller than a fraction of the wavelength, also influence the results. Small ground planes tend to have higher currents running on the ground plane and could lead to unstable results when trying to measure the input reflection coefficient at the antenna feed point. The location of the ferrite along the cable has also an impact of the measurement.



Figure 7.4.3 Use of ferrite to reduce leakage current

7.4.2 Measurement results

Measurement results of the impedance are shown in Table 7.4.1 and Table 7.4.2. The value of the impedance is given in the middle of the band, i.e. 2.45 GHz:

Table 7.4.1 Input impedance of samples 1 and 2 (classical loop antenna)

Sample	Input impedance
1	$22\Omega - j5.3\Omega$
2	$18\Omega - j15\Omega$

Table 7.4.2 Input impedance of samples 3 and 4 (folded loop antenna)

Sample	Input impedance
3	$39.5\Omega - j43.7\Omega$
4	$23.9\Omega - j28\Omega$

As the input impedance is known, the element of the matching circuit can be now computed. A PI circuit has been chosen for the following reasons.

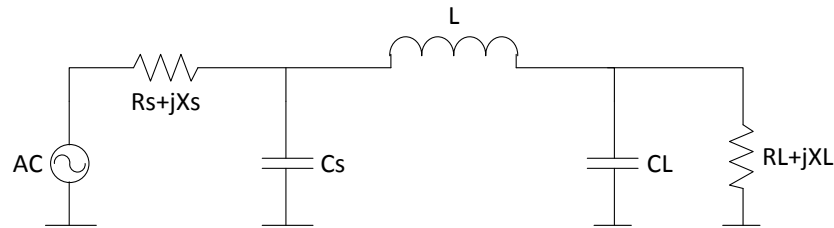


Figure 7.4.3 Matching circuit using a PI topology

The main advantages of using a PI (or T) circuit are:

1. Three-element Pi and T networks permit the matching of almost any load conditions
2. Added element has the advantage of more flexibility in the design process (fine tuning)
3. Provides quality factor design, allow is an extra degree of freedom to control the value of Q in addition to performing impedance transformation/matching
4. When 3 elements are used in a matching network, we are no longer limited to a single value of network Q as using 2 elements circuit. For a given set of source/load resistances now we can select any Q higher than the one when using 2 elements L –type network.
5. The 3 element Pi or Tee type networks can match a source that is either higher or lower than the load resistance, simply by alternating ratio of the two shunt components.
6. The Pi network can be described as two “back to back” L networks that are both configured to match the load and the source to a virtual resistance located at the junction between the two networks.

In matching a small loop antenna, it is important to remember that the series matching inductor must have a tiny series resistance.

For each sample, the following bill of material is computed and derived with a selected quality factor Q equals to 3:

Table 7.4.3 Matching circuit components (classical loop antenna)

Sample	C_s	L	C_L
1	3.9pF	1.6nH	4.66pF
2	3.9pF	1.7nH	3.0pF

Table 7.4.4 Matching circuit components (folded loop antenna)

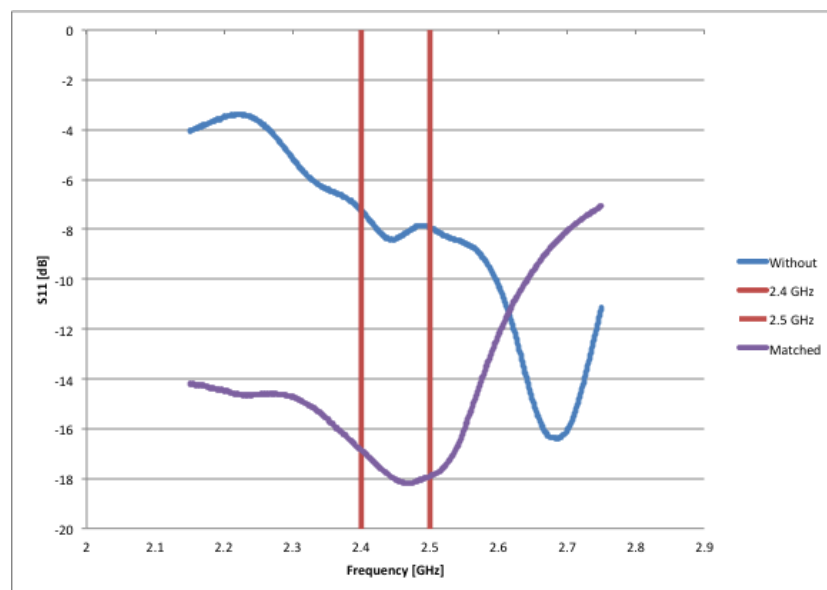
Sample	C_s	L	C_L
3	3.9pF	2.3nH	2.2pF
4	3.9pF	2.02nH	2.3pF

It was found that after several trials only the inductance L is required to obtain an excellent broadband matching, as shown in the following pictures. The value of L was set to 1.8nH for both sample one and two. This is partly due to the fact that the pads and footprints of the capacitors, due to their design and geometry, already present a capacity of about a few pF. For sample three an inductor of 2.2 nH is required while for sample four requires an inductor of 1.8 nH.

The following Figure 7.4.4, Figure 7.4.5, Figure 7.4.6 and Figure 7.4.7 present the measurement results of the input antenna impedance with (purple) and without (blue) the matching network.

- The input reflection coefficient S_{11} for sample 1:

In Figure 7.4.4, blue curve shows the input reflection coefficient without the matching circuit while the purple curve presents the effect of adding the matching circuit with and its components. The two vertical red lines indicate the limit of the useful bandwidth (ISM 2.4 GHz). There is a big significant improvement in terms of bandwidth (more than 200MHz).

**Figure 7.4.4 S_{11} for sample 1**

- The input reflection coefficient S_{11} for sample 2:

In Figure 7.4.5, blue curve shows the input reflection coefficient without the matching circuit while the purple curve presents the effect of adding the matching circuit with and its components. The two vertical red lines indicate the limit of the useful bandwidth (band ISM 2.4 GHz). There is a big significant improvement in terms of bandwidth (more than 200MHz).

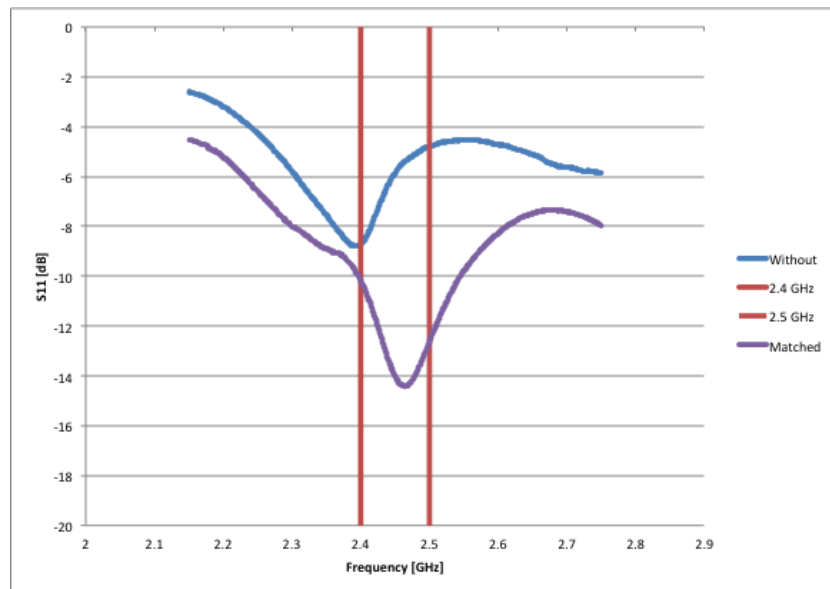


Figure 7.4.5 S_{11} for sample 2

- The input reflection coefficient S_{11} for sample 3:

In Figure 7.4.6, blue curve shows the input reflection coefficient without the matching circuit while the purple curve presents the effect of adding the matching circuit with and its components. The two vertical red lines indicate the limit of the useful bandwidth (band ISM 2.4 GHz). There is a big significant improvement in terms of bandwidth (more than 150MHz).

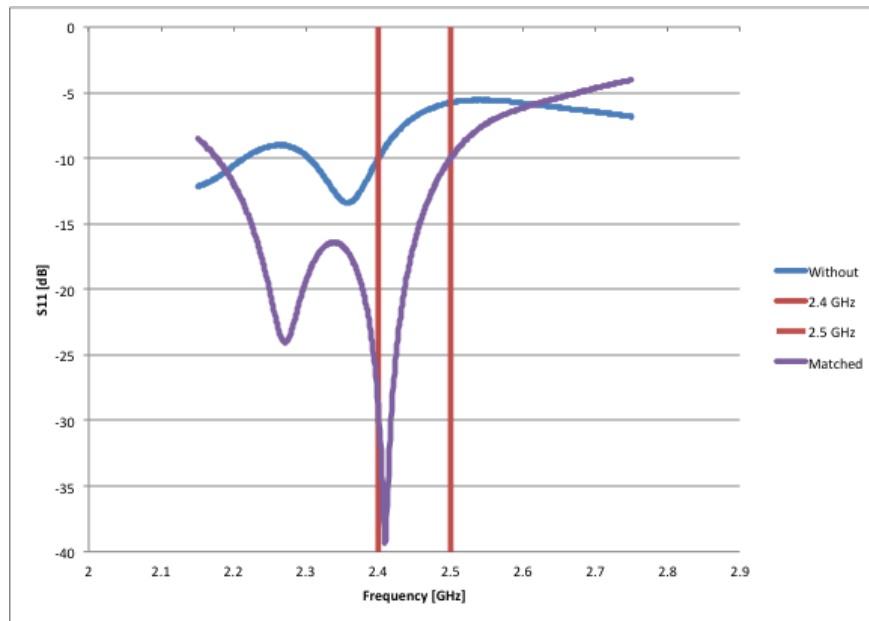


Figure 7.4.6 S_{11} for sample 3

- The input reflection coefficient S_{11} for sample 4:

In Figure 7.4.7, blue curve shows the input reflection coefficient without the matching circuit while the purple curve presents the effect of adding the matching circuit with and its components. The two vertical red lines indicate the limit of the useful bandwidth (band ISM 2.4 GHz). There is a big significant improvement in terms of bandwidth (more than 200MHz).

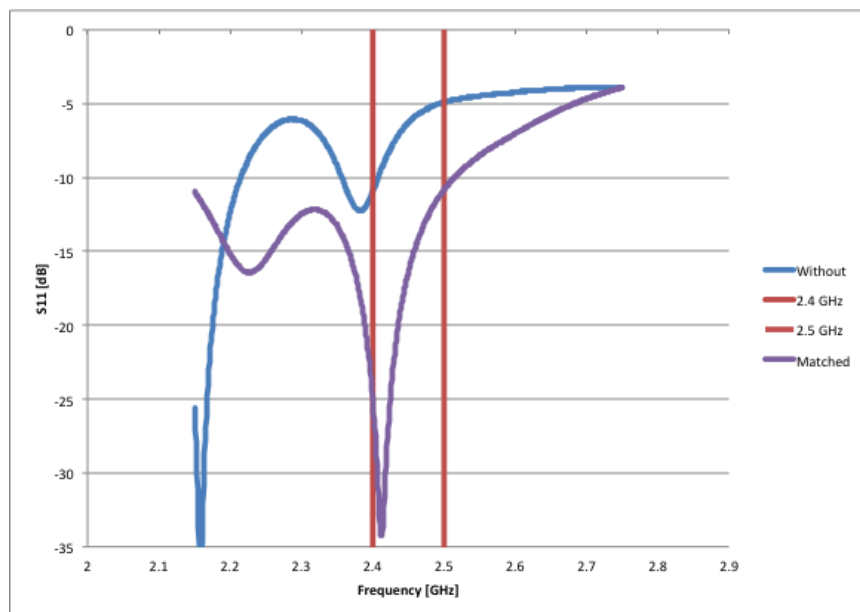


Figure 7.4.7 S_{11} for sample 4

7.5 Conclusion

We have designed a system that allows for a flexible use to re-match, re-tune an antenna that resonates at a frequency rather close to the targeted one. We clearly see with these four examples that we have enough room to refocus the antenna and thus to make it resonate at the right frequency. In such a way we increase the link budget of the communication by increasing the delivered power to the antenna by minimizing the reflected power. Next step will be measurement of efficiency and radiation pattern of these antennas.

8 CEA Passive antenna for Micro SD card

8.1 Antenna structure

The passive antenna design has to be integrated in an 11 mm x 7 mm x 1 mm micro SD extension defined by the specifications as shown Figure 8.1.1.

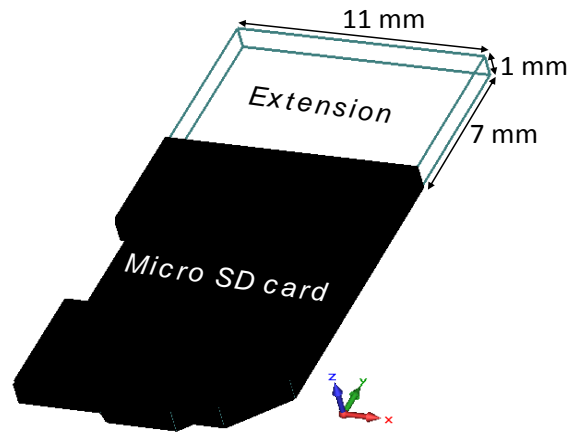


Figure 8.1.1 Micro SD card with its extension

The proposed micro SD antenna design is an hybrid antenna, because it is between a folded T-shaped monopole antenna and an inverted F antenna.

The first designed topology exhibited the antenna on an alumina substrate (see Figure 8.1.2).

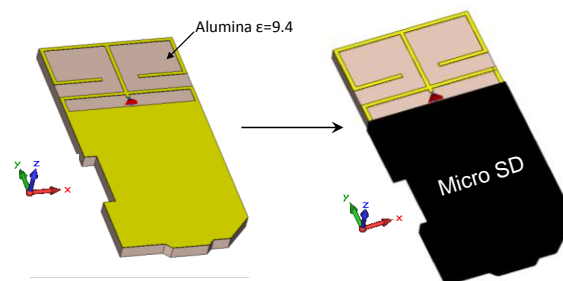


Figure 8.1.2 Micro SD antenna on the alumina substrate

To ease antenna manufacturing, the design was amended to be on a FR4 substrate. Since the dielectric permittivity of the FR4 is lower than the one of the alumina, the radiated element length has been extended to increase the electrical length, by keeping the same total dimension of the Micro SD card plus extension. The new structure on the FR4 substrate is presented Figure 8.1.3.

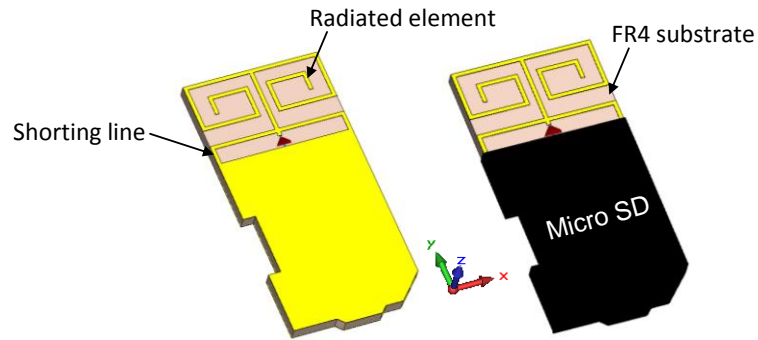


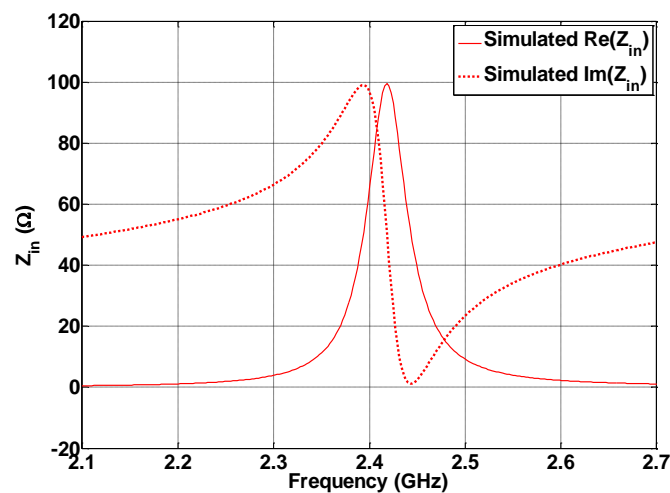
Figure 8.1.3 Micro SD antenna on the FR4 substrate

The shorting line allows achieving a parallel resonance, whereas the input impedance is depending on its shape and length. As expected, the value of the resonant frequency is controlling by the radiated element length.

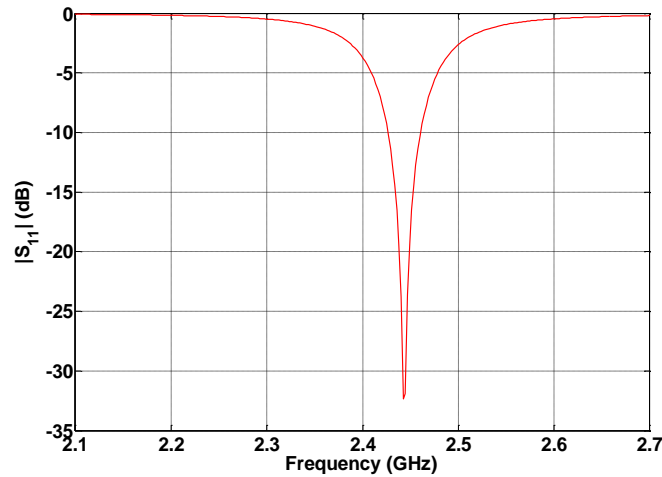
It is directly fed by a 50Ω -discrete port has been simulated with the FIT method using CST Microwave Studio. It must be noticed that a discrete port is modeled by a lumped element, consisting of a current source with a 50Ω -inner impedance.

8.2 Simulation results

Simulated antenna input impedance and return loss are plotted in Figure 8.2.1.



(a)



(b)

Figure 8.2.1 Input impedance (a) and $|S_{11}|$ parameter (b) of the micro SD antenna on the FR4 substrate

These results show that the antenna is matched on the [2.426– 2.461] GHz frequency range, representing 1.43% of bandwidth at -10dB. It should be noted that the frequency range can be changed (without being an active antenna) by changing the radiated element length.

The radiated performances have also been simulated. Figure 8.2.2 and Figure 8.2.3 respectively present the total efficiency and the maximum realized gain together with the $|S_{11}|$ parameter.

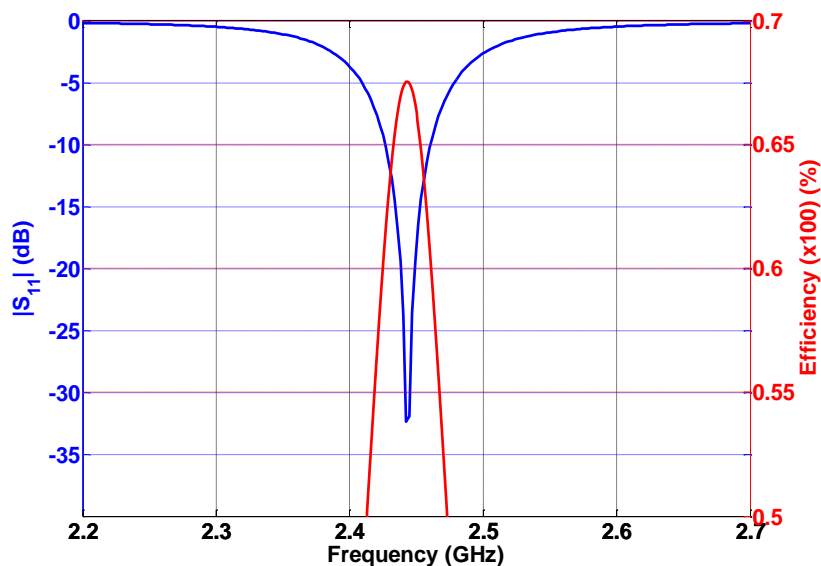


Figure 8.2.2 $|S_{11}|$ parameter vs the total efficiency

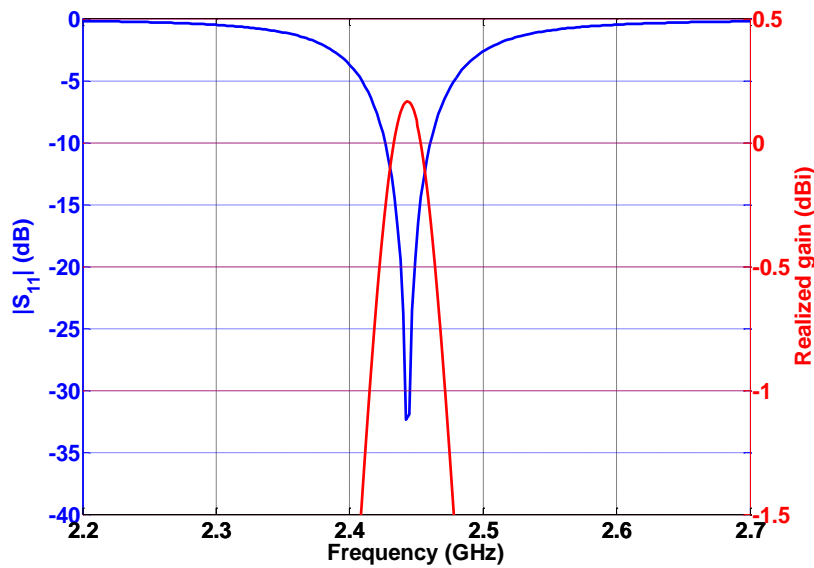
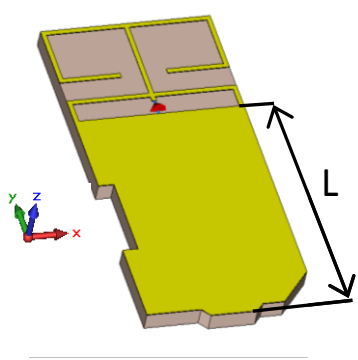


Figure 8.2.3 $|S_{11}|$ parameter vs the maximum realized gain

The total efficiency is reaching 67% at the matched frequency whereas the maximum realized gain equals 0.2 dBi.

In the zone where the micro SD is not entirely metalized (i.e. the antenna ground plane is reduced), additional studies have been done to see the antenna performances impact. Studies results are depicted Table 8.2.1.

Table 8.2.1 Antenna performances according to the ground plane length

L=15mm	f_m	2.44 GHz	
	Bandwidth	1.4%	
	Directivity	1.9 dBi	
	Realized gain	0.2 dBi	
	Total efficiency	67%	
L=3mm	f_m	2.59 GHz	
	Bandwidth	0.8%	
	Directivity	2 dBi	
	Realized gain	-3.9 dBi	
	Total efficiency	26%	

As expected and according to the Chu limit [4], both total efficiency and bandwidth are lower when the ground plane length is reduced. Moreover, a frequency detuning is observed, representing an increase of 6% from a 3mm to a 15mm ground plane length.

8.3 Methodology for antenna measurement

To measure the antenna, the 50Ω -discrete port has to be replaced with a real excitation, i.e. a coplanar waveguide printed on the FR4 substrate. A RF coaxial cable is exciting the coplanar waveguide as depicted Figure 8.3.1.

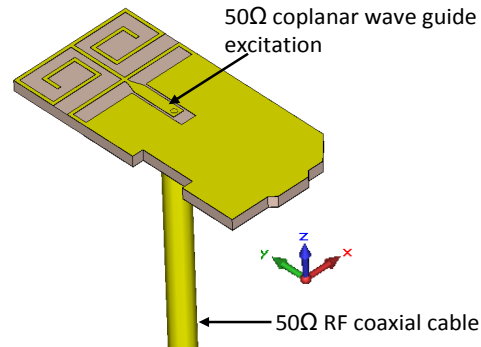


Figure 8.3.1 Micro SD antenna excited by a coplanar waveguide

Also for the passive antenna we will adopt the same approach than the CEA active antenna. For sake of brevity, all steps will not be detailed here.

Depending on the cable length L both input impedance and $|S_{11}|$ parameter are changing (see Figure 8.3.2).

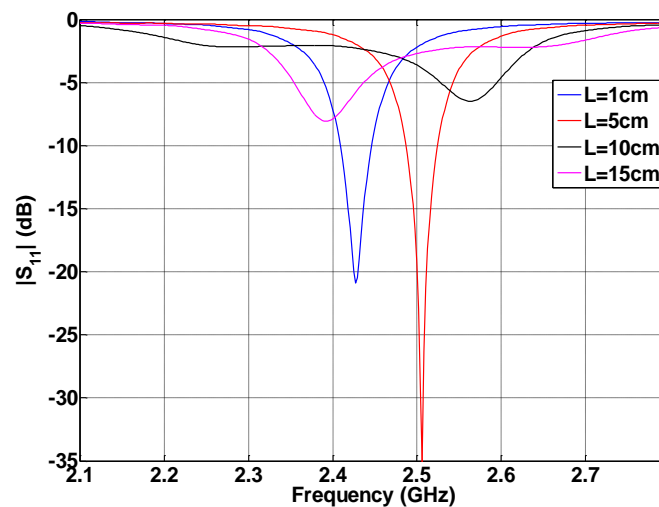


Figure 8.3.2 $|S_{11}|$ parameter according to the L length of the RF coaxial cable

Thus, like the previous CEA antenna, it is necessary and possible to control the antenna surrounding by integrating a quarter wave length stub. This allows having unchanged results regardless the cable length under the stub as shown Figure 8.3.3.

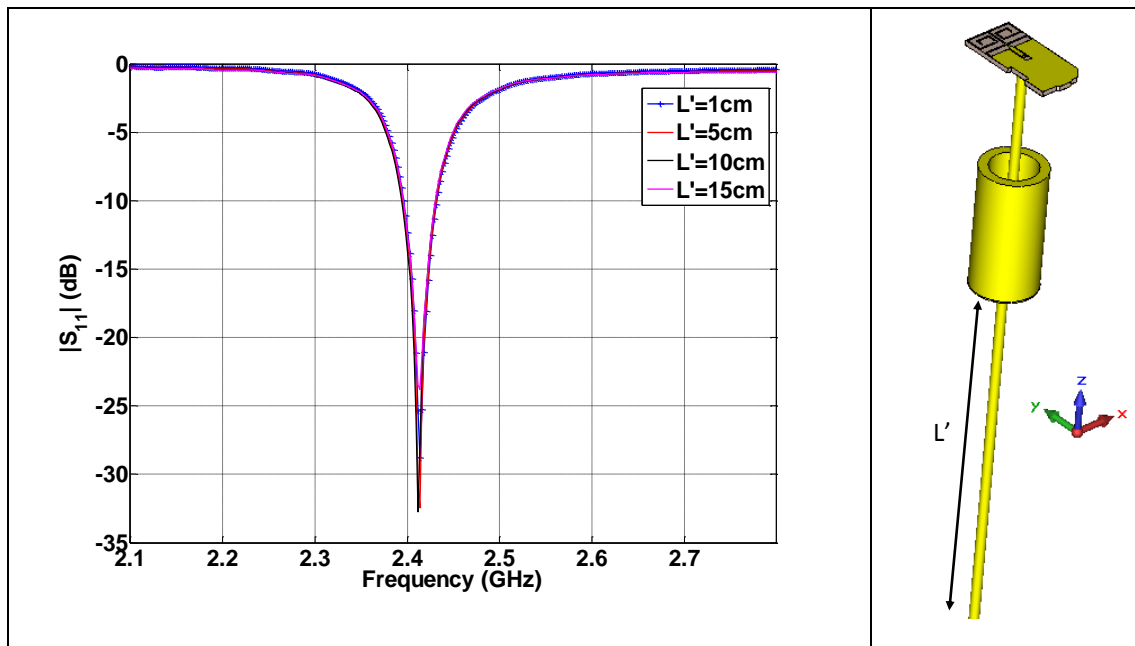


Figure 8.3.3 $|S_{11}|$ parameter according to the L' length of the RF coaxial cable under the stub

8.4 Antenna prototype

An antenna prototype was manufactured on a 1mm-thick FR4 substrate. All the micro-SD is metalized and a quarter wave length stub has been integrated on the RF feed cable (see Figure 8.4.1). The coplanar waveguide is presenting an impedance equals to 50Ω and is exciting by the 50Ω RF feed cable.

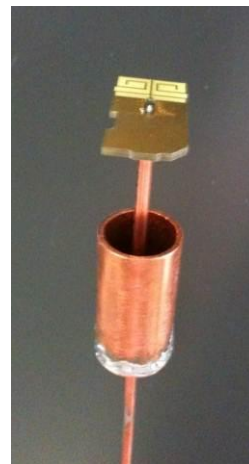
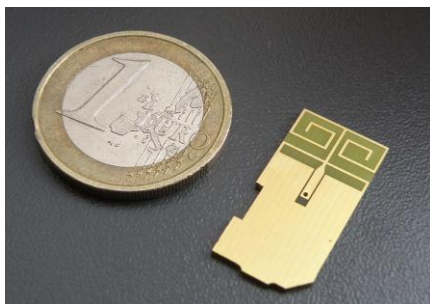
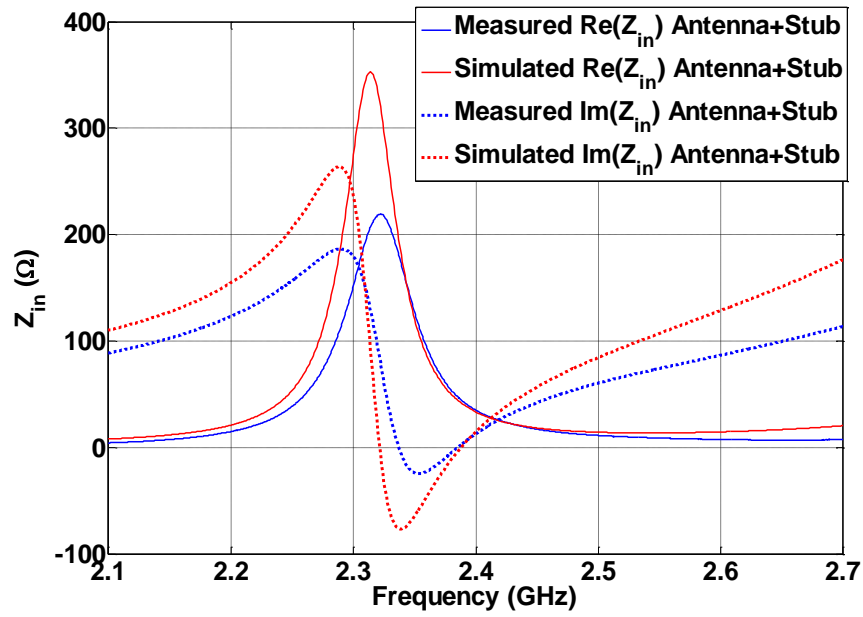


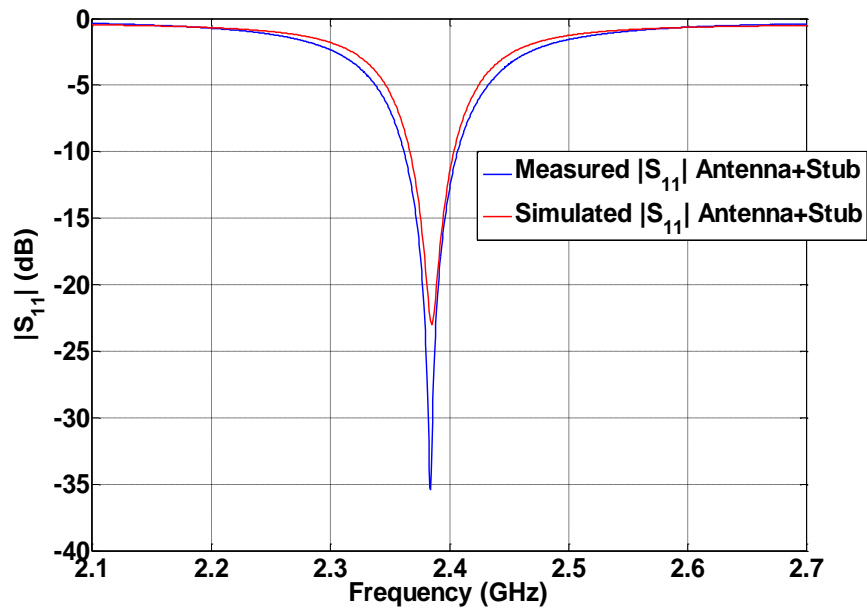
Figure 8.4.1 Manufactured prototype

8.5 Impedance results

Figure 8.5.1 presents the comparison between the measured and simulated impedance results for the {antenna + stub} structure. Using the same method as the previous CEA antenna, the transfer function has been determined. Finally, thanks to the transfer function from the {antenna + stub} structure results, Figure 8.5.2 shows the comparison between the simulated and the “measured” single antenna results.

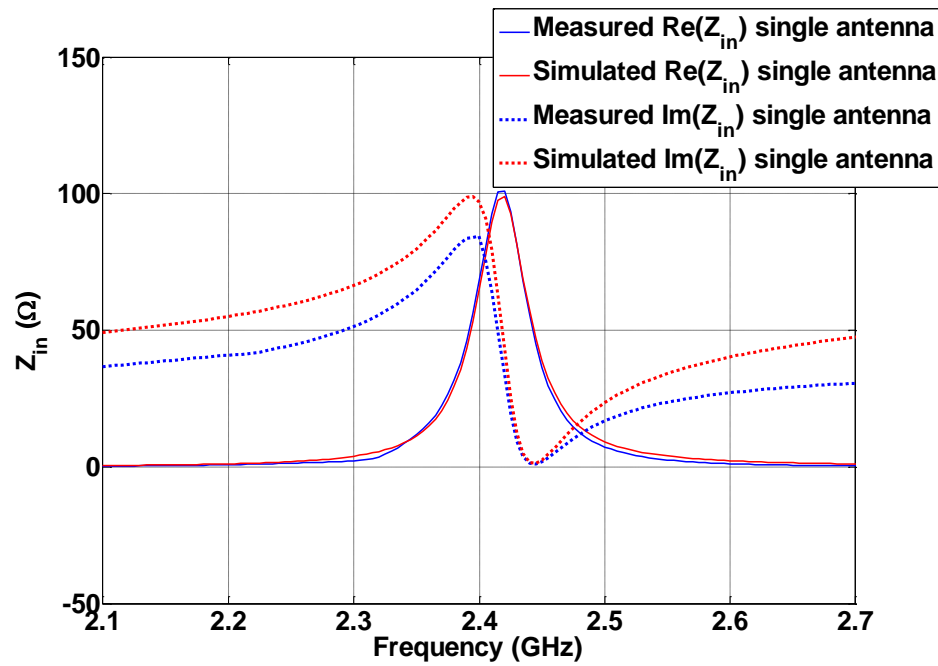


(a)

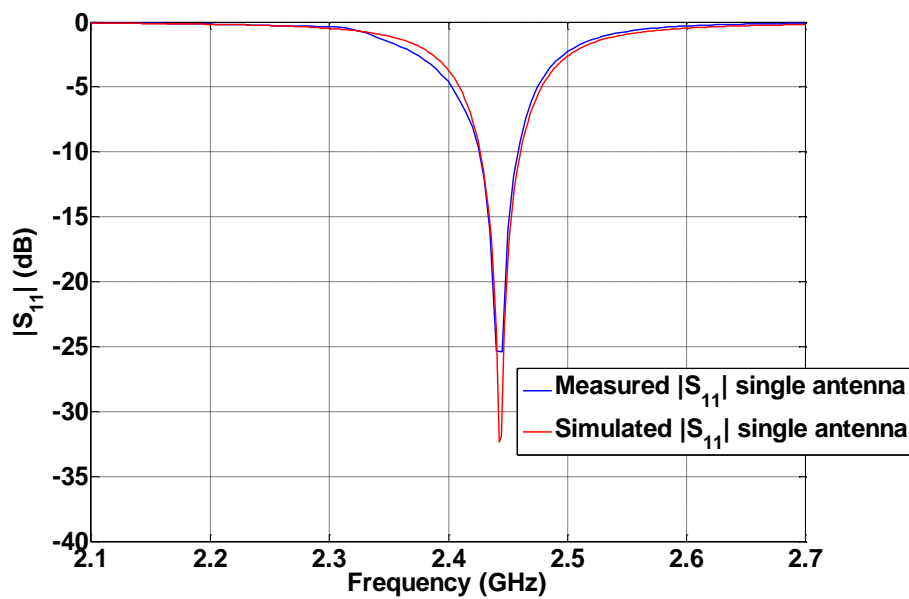


(b)

Figure 8.5.1 Comparison between simulated and measured input impedance (a) and $|S_{11}|$ parameter (b) for the {antenna + stub} structure



(a)



(b)

Figure 8.5.2 Comparison between simulated and measured input impedance (a) and $|S_{11}|$ parameter (b) for the single antenna case

All these previous results exhibit an excellent agreement between measurement and simulation. The measured single antenna is covering the [2.426– 2.458] GHz frequency band at -10 dB, corresponding to 1.3% of bandwidth. If a -6 dB is considered for matching boundary, 2.55% of bandwidth is covered by the measured single antenna.

8.6 Radiation results

Radiation and directivity patterns present omnidirectional properties. The 3D directivity pattern at the matching frequency is presented Figure 8.6.1. The maximum realized gain for the single antenna in the air is -0.2 dBi.

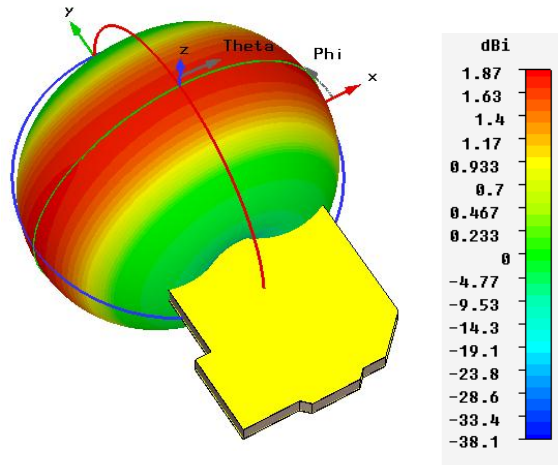
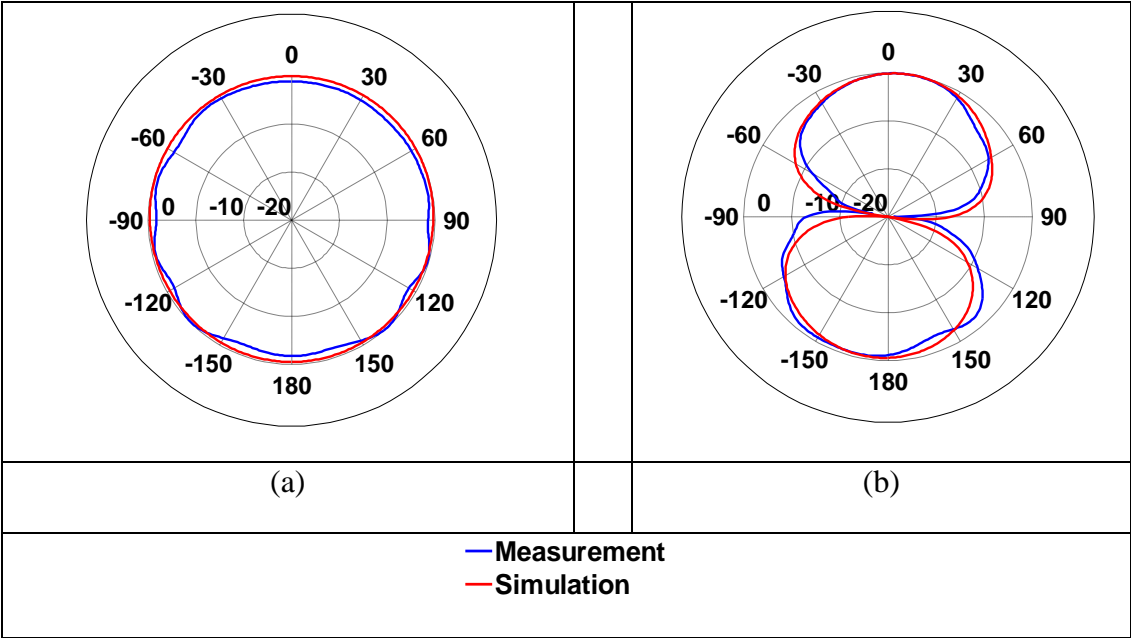


Figure 8.6.1 Directivity pattern at the matching frequency (simulation)

Radiation properties have been measured in an anechoic chamber in three planes: xOy, yOz and xOz planes. Figure 8.6.2 is presenting the comparison between measured and simulated total normalized radiation patter including the quarter wavelength stub.



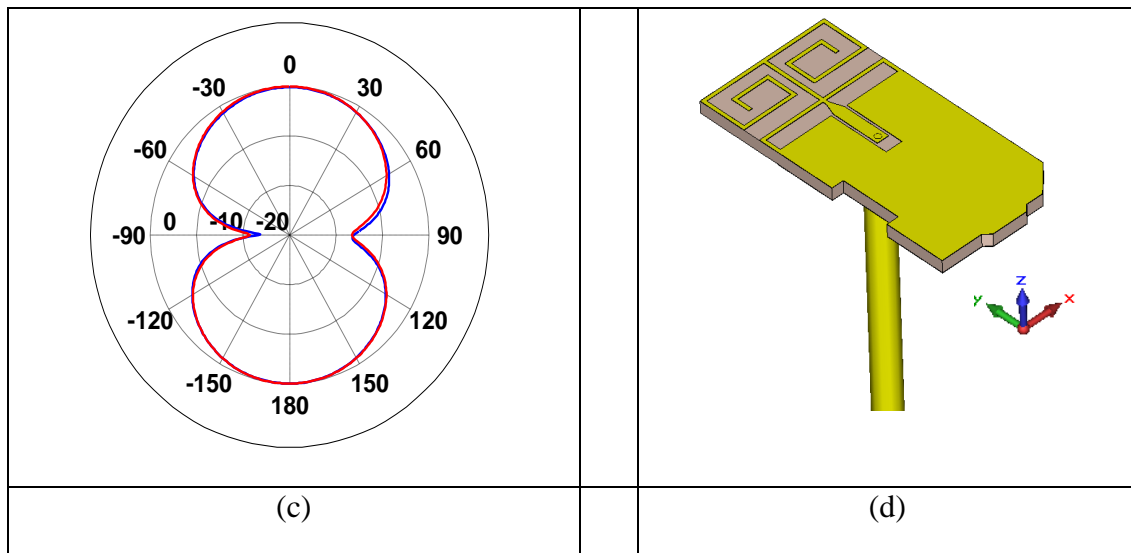


Figure 8.6.2 Radiation pattern in the xOz (a), yOz (b) and xOy (c) planes and respective coordinates of the structure (d)

The {antenna + stub} structure presents omnidirectional properties in both measurement and simulation with a main linear polarization along y axis. In each plane, the measured maximum realized gain is equal to -0.4 dBi while the simulated one equals -1 dBi.

8.7 Antenna characteristics in a Smartphone

8.7.1 Investigated scenarios

The integration of this micro SD antenna in a Smartphone has been investigated. This latter has been simulated as a PCB card enclosed by a plastic case. Because the integration in the smartphone scenario is not completely defined at this stage of the project, many cases have been studied and compared:

- The micro SD antenna has absolutely no connection with the PCB card of the Smartphone and the micro SD card has an off-centered position according to the Smartphone side as presented Figure 8.7.1.
- The micro SD antenna has a connection with the PCB card of the Smartphone and the micro SD card has a central position according to the Smartphone side as presented Figure 8.7.1.
- The micro SD antenna has a connection with the PCB card of the Smartphone and the micro SD card has an off-centered position according to the Smartphone side as presented Figure 8.7.1.

All these scenarios will be compared with the single antenna case previously presented.

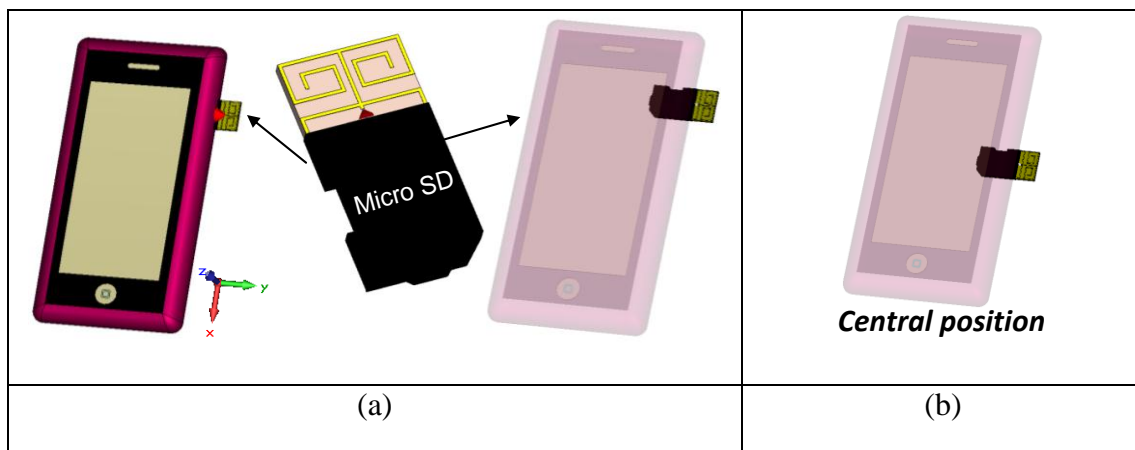
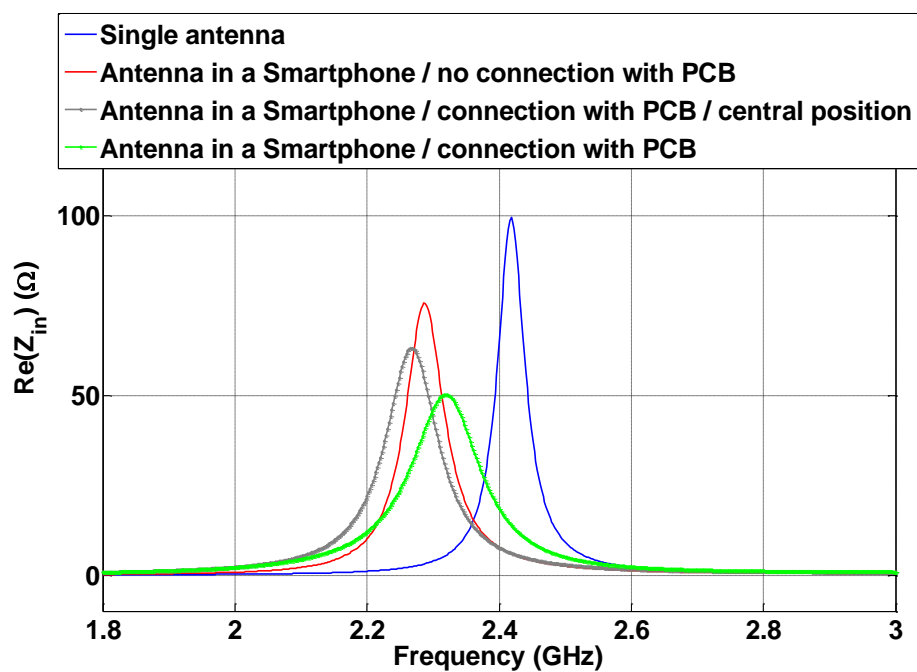


Figure 8.7.1 Integration of the micro SD antenna with off-centered (a) and a central (b) positions

8.7.2 Simulation results of smartphone influence

Real and imaginary parts of the input antenna impedance in the smartphone are presented Figure 8.7.2.



(a)

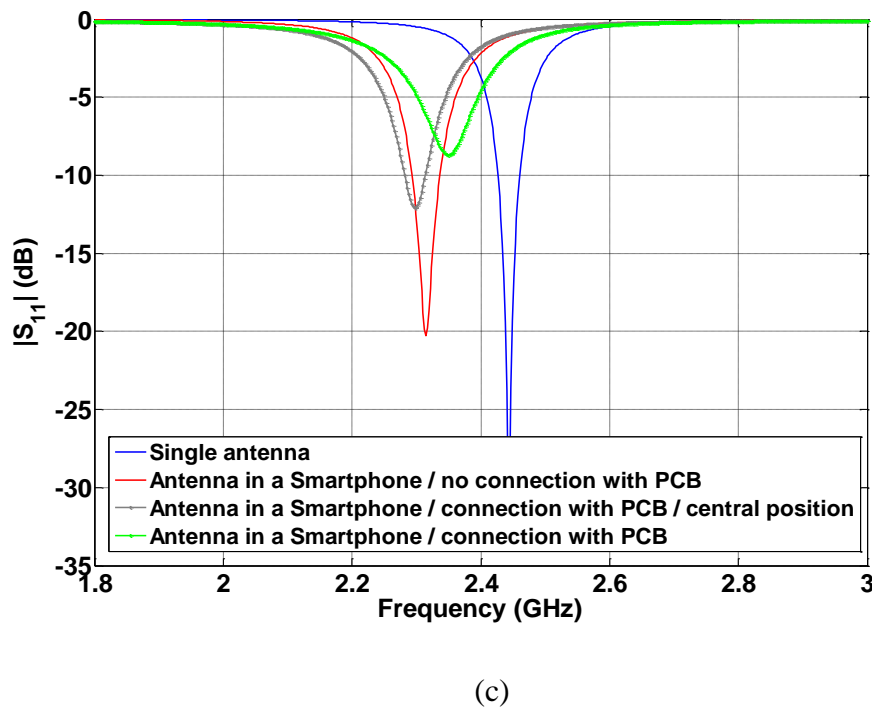
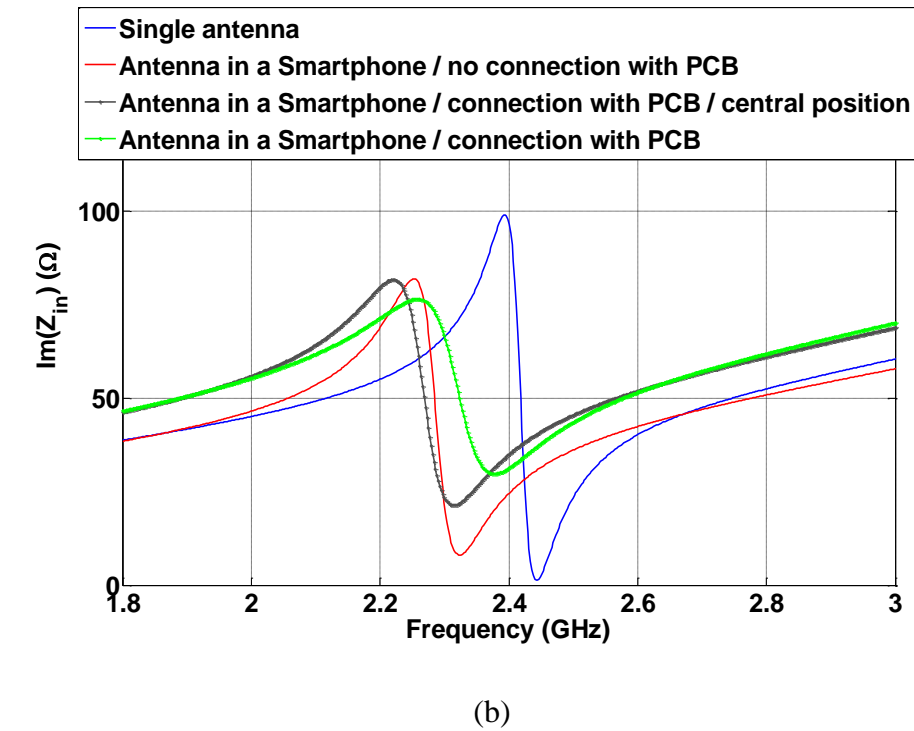


Figure 8.7.2 Real (a) and imaginary (b) parts of the input impedance and $|S_{11}|$ parameter (c) for the different scenarios

The presence of the Smartphone involves a frequency detuning, and a decrease of the resonance frequency. Moreover, when the micro SD card is connected to the PCB card of the Smartphone, i.e. when the antenna ground plane is extended, radiated Q factor is decreasing and antenna is no longer matched at -10dB. Indeed, the $|S_{11}|$

parameter presented Figure 8.7.2 shows that the worst case is the one when the micro SD antenna has a connection with the PCB card of the Smartphone and is off-centered according to the Smartphone side.

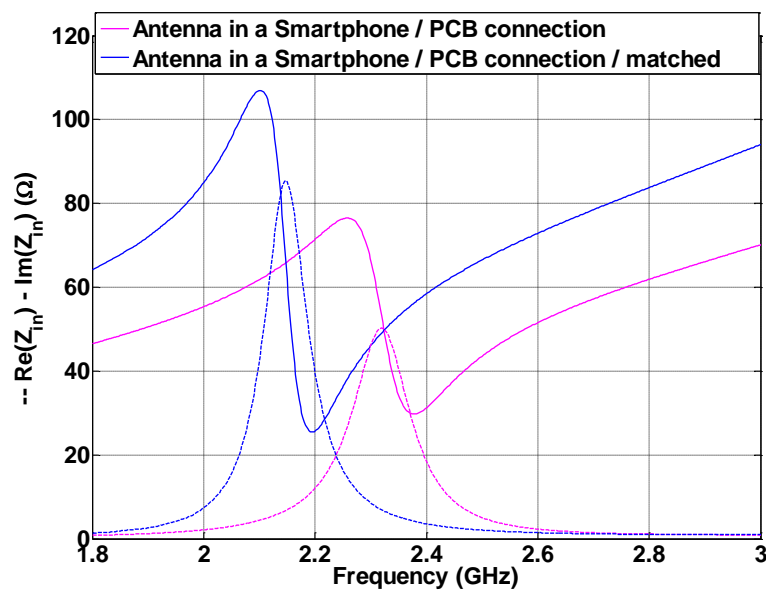
8.7.3 Optimization of the antenna in the Smartphone

Considering the worst case, this section will try to supply satisfactory answers about the antenna re-optimization to match it on the ISM band as for the single antenna scenario.

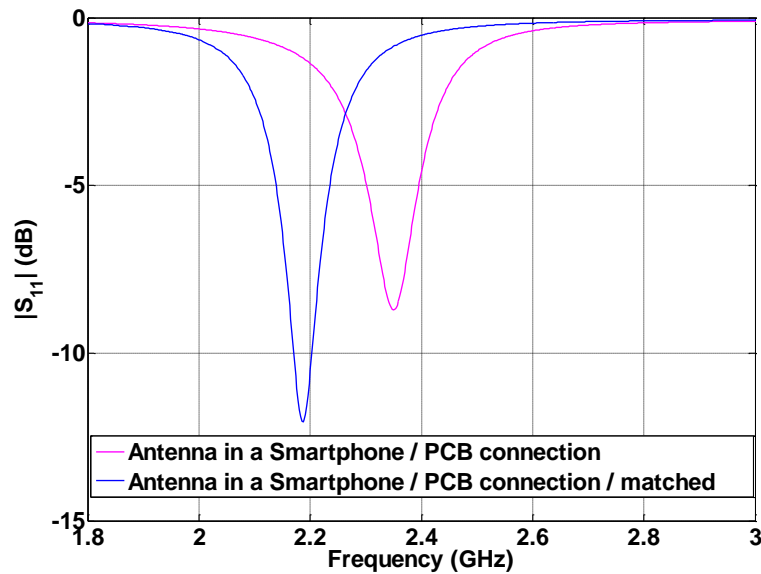
- Antenna matching

To match the antenna, the amplitude of both real and imaginary parts has to be higher in order to increase the radiated Q factor. The antenna's shorting line allows adjusting the antenna input impedance.

The Figure 8.7.3 is presenting the comparison between input impedances before and after the adjustment of the antenna. Real and imaginary parts amplitudes are higher for the optimized antenna case, which allows achieving 1.7% of bandwidth at -10 dB as it can be seen on Figure 8.7.3.



(a)



(b)

Figure 8.7.3 Input impedance (a) and $|S_{11}|$ parameter (b) before and after antenna optimization

However, the matching band is not embedded in the ISM band and the radiated element has to be adjusted in order to provide a higher resonance.

- Antenna matching in the ISM band

To match the antenna in the ISM band, the resonance frequency has to be increased. To achieve that, the length of the radiated element has been reduced as shown on the Figure 8.7.4.

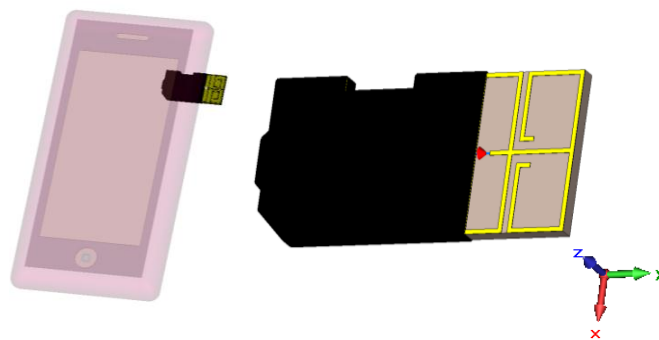
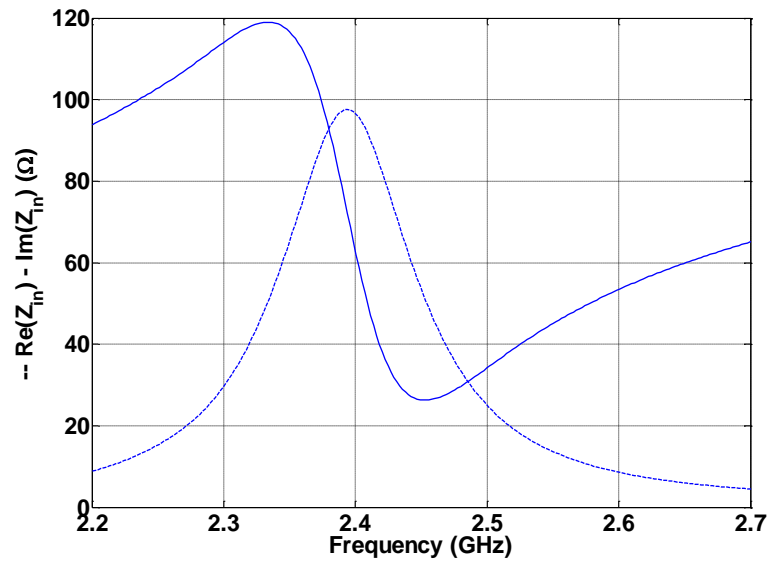
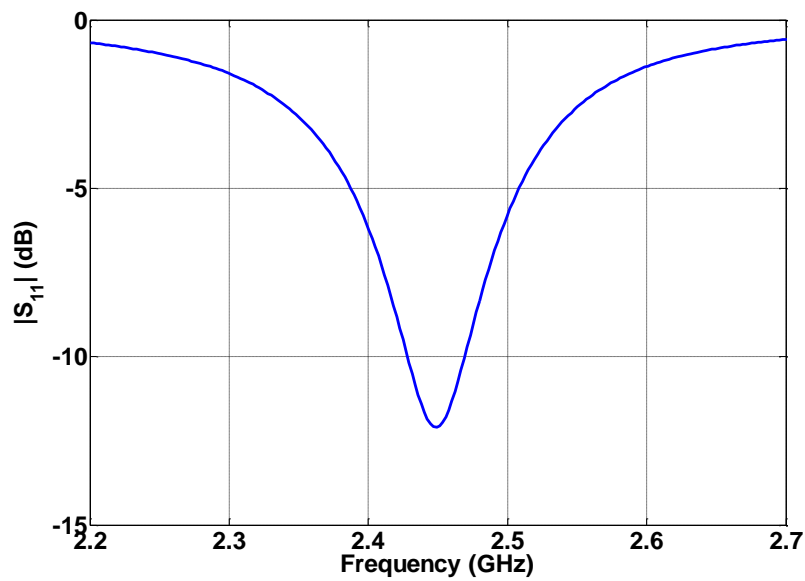


Figure 8.7.4 Antenna optimization to match it in the ISM band

The Figure 8.7.5 presents both input impedance and $|S_{11}|$ parameter for the antenna optimized in the Smartphone.



(a)



(b)

Figure 8.7.5 Input impedance (a) and $|S_{11}|$ parameter (b) of the optimized antenna in the Smartphone

The $|S_{11}|$ parameter shows that the antenna is matched on the [2.428– 2.469] GHz frequency range, i.e. has 1.7% of bandwidth at -10dB. It should be noted that if the matching band is now considered at -6 dB, all the ISM band is covered.

As expected, the 3D directivity pattern of the antenna integrated in the Smartphone is disturbed as shown Figure 8.7.6. It has now directional radiation properties compared with the single antenna case, which presents an omnidirectional radiation pattern.

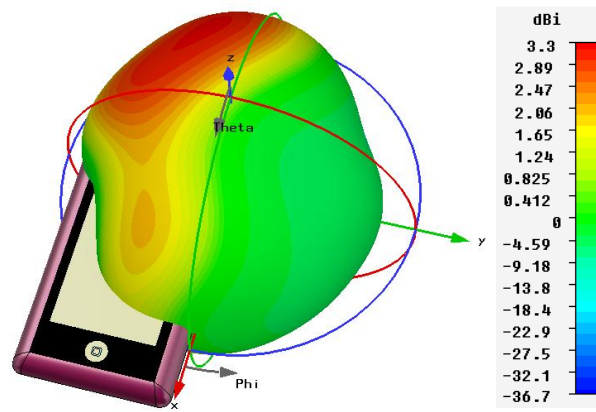


Figure 8.7.6 Directivity pattern for the Smartphone scenario

Table 8.7.1 is summarizing the antenna performances at the matching frequency for three relevant cases: the single antenna case, the Smartphone case without any connection with the PCB card and the Smartphone case with a PCB card connection (the case previously addressed).

Table 8.7.1 Antenna performances for different scenarios

	Directivity max	Radiated efficiency	Maximum of the realized gain
Single antenna	1.87 dBi	67%	0.15 dBi
Smartphone / No PCB connection	3.3 dBi	77%	1.9 dBi
Smartphone / PCB connection	3.8 dBi	78%	2 dBi

This table exhibits that antenna performances in terms of total efficiency and maximum realized gain are better for Smartphone scenarios.

9 Conclusions

This D3.2 document is the first important “milestone” report in anticipation of the final version D3.3.

At this stage, important results have been achieved, with the first antenna prototype realizations and the corresponding measurements. This puts the WP3 stakeholders in good shape for fine-tuning the antenna designs taking into account system and housing requirements in anticipation of the final system integration.

On the other hand, the antenna-to-radio interface still needs some work as issues have been faced for realizing the measurements. A memo will be issued at M22, and the results consolidated into the final D3.3 deliverable.

List of Tables

Table 3.1 Main specifications of the WiserBAN transceiver	10
Table 3.2 Specifications of the RF front-end	12
Table 4.1 Main performance parameters of the RF SAW filter	13
Table 5.1.1 Tunable L-antenna specifications	18
Table 5.1.2 Design parameters of the tuning circuit	20
Table 5.1.3 Design parameters of the sensing circuit	22
Table 5.2.1 Summary of the L-antenna and spiral antenna results	31
Table 5.3.1 Electrical parameters of the simple head model at 2.45 GHz	31
Table 6.7.1 3D directivity patterns and antenna performances for both orientation scenarios	48
Table 6.7.2 E fields inside the head for normal orientation	51
Table 6.7.3 Amplitude attenuation model compared with the $ S_{21} $ parameter	52
Table 7.1.1 Performance parameters of a loop antenna	54
Table 7.4.1 Input impedance of samples 1 and 2 (classical loop antenna)	61
Table 7.4.2 Input impedance of samples 3 and 4 (folded loop antenna)	61
Table 7.4.3 Matching circuit components (classical loop antenna)	62
Table 7.4.4 Matching circuit components (folded loop antenna)	63
Table 8.2.1 Antenna performances according to the ground plane length	70
Table 8.7.1 Antenna performances for different scenarios	82

List of Figures

Figure 2.1 WiserBAN platform architecture	8
Figure 2.2 Main parts of the WiserBAN antenna-to-radio interface	9
Figure 3.1 Block diagram of the WiserBAN transceiver	10
Figure 3.2 Schematic presentation of the RF front-end	11
Figure 4.1 Package of the RF SAW filter	14
Figure 5.1.1 Layout of L-antenna on IPD	16
Figure 5.1.2 Input impedance of L-antenna	16
Figure 5.1.3 Radiation patterns of L-antenna	17
Figure 5.1.4 Matching circuits for L-antenna	17
Figure 5.1.5 Frequency tuning of L-antenna	18
Figure 5.1.6 Simplified schematic diagram of the tuner circuit	19
Figure 5.1.7 Simplified schematic diagram of the impedance sensing block	22
Figure 5.2.1 Simulation models of the L-antenna prototypes	23
Figure 5.2.2 Simulation results of the L-antenna v1	24
Figure 5.2.3 Simulation results of the L-antenna v2	24
Figure 5.2.4 Radiation efficiency of spiral antenna versus substrate thickness	25
Figure 5.2.5 Simulation models of the spiral antenna prototypes	25
Figure 5.2.6 Simulation results of the spiral antenna v1	26
Figure 5.2.7 Simulation results of the spiral antenna v2	26
Figure 5.2.8 Photographs of the first L-antenna prototypes	27
Figure 5.2.9 Photographs of the first spiral antenna prototypes	27
Figure 5.2.10 Photographs of the UFL-SMA RF cables	28
Figure 5.2.11 Reflection coefficients of L-antenna v1	28
Figure 5.2.12 Reflection coefficients of L-antenna v2	29
Figure 5.2.13 Reflection coefficients of spiral antenna v1	29
Figure 5.2.14 Reflection coefficients of spiral-antenna v2	30

Figure 5.2.15 Radiation patterns of L-antenna v1	30
Figure 5.2.16 Radiation patterns of spiral antenna v2	31
Figure 5.3.1 L-antenna horizontally aligned near a simple head model	32
Figure 5.3.2 L-antenna vertically aligned near a simple head model	32
Figure 5.3.3 Frequency detuning of horizontally and vertically aligned L-antenna near a simple head model	32
Figure 5.3.4 Spiral antenna horizontally aligned near a simple head model	33
Figure 5.3.5 Spiral antenna vertically aligned near a simple head model	33
Figure 5.3.6 Frequency detuning of horizontally and vertically aligned spiral-antenna near a simple head model	33
Figure 5.3.7 Radiation efficiencies of L-antenna and spiral antenna at 2.4 GHz when placed at different distances from the simple head model	34
Figure 6.1.1 Perspective, top and side views of the antenna structure	35
Figure 6.2.1 Input impedances for different capacitor values	36
Figure 6.2.2 $ S_{11} $ parameters and total efficiencies for different capacitor values	36
Figure 6.3.1 Surface current according to the cable	37
Figure 6.3.2 Input impedance and $ S_{11} $ parameter according to the cable length L	38
Figure 6.3.3 Integration of a quarter wave length stub on the RF feed cable	38
Figure 6.3.4 Surface current on the cable with the stub	39
Figure 6.3.5 Input impedance and $ S_{11} $ parameter according to the cable length L' under the stub	40
Figure 6.3.6 Radiated {antenna + stub} structure	40
Figure 6.4.1 Prototype of the {antenna + stub} structure	41
Figure 6.5.1 Comparison between simulated and measured input impedance and $ S_{11} $ parameter for the {antenna + stub} structure	42
Figure 6.5.2 Determination of the transfer function	42
Figure 6.5.3 Comparison between simulated and measured input impedance and $ S_{11} $ parameter for the single antenna structure	43
Figure 6.6.1 3D directivity pattern at 2.47 GHz and antenna radiation patterns	44
Figure 6.6.2 Antenna measurement in the anechoic chamber	45

Figure 6.6.3 Radiation pattern in the xOz , yOz and xOy planes and respective coordinates of the structure	45
Figure 6.7.1 Investigation on the head influence	46
Figure 6.7.2 Input impedance and $ S_{11} $ parameter for head and free space cases	47
Figure 6.7.3 $ S_{21} $ parameter for head and free space cases	48
Figure 6.7.4 Input impedance and $ S_{11} $ parameter for different d lengths and orientations	50
Figure 6.7.5 $ S_{21} $ parameter for different d lengths and orientations	50
Figure 6.7.6 Side and top view of the antenna - SiP layout	52
Figure 7.1.1 Topology of the integrated loop antenna: circular loop antenna, folded loop antenna	53
Figure 7.1.2 Simulated performance characteristics for the integrated loop antenna	54
Figure 7.2.1 Schematic of the matching PCB	56
Figure 7.3.1 The matching PCB circuit	56
Figure 7.3.2 The matching PCB circuit connected to the antenna (classical loop), top and bottom	57
Figure 7.4.1 Antenna and its matching PCB inserted inside the gel	59
Figure 7.4.2 Classical and folded loop antenna	60
Figure 7.4.3 Use of ferrite to reduce leakage current	61
Figure 7.4.3 Matching circuit using a PI topology	62
Figure 7.4.4 S_{11} for sample 1	63
Figure 7.4.5: S_{11} for sample 2	64
Figure 7.4.6 S_{11} for sample 3	65
Figure 7.4.7 S_{11} for sample 4	65
Figure 8.1.1 Micro SD card with its extension	67
Figure 8.1.2 Micro SD antenna on the alumina substrate	67
Figure 8.1.3 Micro SD antenna on the FR4 substrate	68
Figure 8.2.1 Input impedance and $ S_{11} $ parameter of the micro SD antenna on the FR4 substrate	69

Figure 8.2.2 $ S_{11} $ parameter vs the total efficiency	69
Figure 8.2.3 $ S_{11} $ parameter vs the maximum realized gain	70
Figure 8.3.1 Micro SD antenna excited by a coplanar waveguide	71
Figure 8.3.2 $ S_{11} $ parameter according to the L length of the RF coaxial cable	71
Figure 8.3.3 $ S_{11} $ parameter according to the L' length of the RF coaxial cable under the stub	72
Figure 8.4.1 Manufactured prototype	72
Figure 8.5.1 Comparison between simulated and measured input impedance and $ S_{11} $ parameter for the {antenna + stub} structure	73
Figure 8.5.2 Comparison between simulated and measured input impedance and $ S_{11} $ parameter for the single antenna case	74
Figure 8.6.1 Directivity pattern at the matching frequency (simulation)	75
Figure 8.6.2 Radiation pattern in the xOz, yOz and xOy planes and respective coordinates of the structure	76
Figure 8.7.1 Integration of the micro SD antenna with off-centered and a central positions	77
Figure 8.7.2 Real and imaginary parts of the input impedance and $ S_{11} $ parameter for the different scenarios	78
Figure 8.7.3 Input impedance and $ S_{11} $ parameter before and after antenna optimization	80
Figure 8.7.4 Antenna optimization to match it in the ISM band	80
Figure 8.7.5 Input impedance and $ S_{11} $ parameter of the optimized antenna in the Smartphone	81
Figure 8.7.6 Directivity pattern for the Smartphone scenario	82

List of reference documents

- [1] Delaveaud, C. Leveque, P. Jecko, B., "Small-sized low-profile antenna to replace monopole antennas", Electronics Letters, 16 Apr 1998, Volume: 34, Issue: 8, pp: 716-717.
- [2] S. Sufyar, C. Delaveaud " A miniaturization technique of a compact omnidirectional antenna ", Radioengineering, December 2009, Volume 18, Number 4.
- [3] Alves, T.; Poussot, B.; Laheurte, J.-M.; , "Analytical Propagation Modeling of BAN Channels Based on the Creeping-Wave Theory," Antennas and Propagation, IEEE Transactions on , vol.59, no.4, pp.1269-1274, April 2011
- [4] L. J. Chu, "Physical Limitations of Omni-Directional Antennas," J. Appl. Phys., 19, December 1948, pp. 1163-1175.